Modelling coronary blood flow using a non Newtonian fluid model : fractional flow reserve estimation

Keltoum Chahour

UNIVERSITÉ CÔTE D'AZUR

ÉCOLE DOCTORALE
SCIENCES FONDAMENTALES ET APPLIQUÉES

جامعة محمد الخامس بالرباط
Université Mohammed V de Rabat

Modélisation de l'écoulement sanguin coronaire à l'aide d'un modèle de fluide non Newtonien: estimation de la fraction de réserve fluide

Keltoum CHAHOUR

Laboratoire J.A. Dieudonné

Présentée en vue de l'obtention du grade de docteur en mathématiques de l'université Côte d'Azur et de l'université Mohammed V de Rabat.
Dirigée par: Abderrahmane Habbal / Rajae Aboulaich.
Soutenue le: 02 Décembre 2019.

Devant le jury, composé de:

Rajae Aboulaich, Professeur EMI.
Soumaya Boujena, Professeur Université Hassan II.
Abderrahmane Habbal, MDC HC HDR, UCA.
Olivier Pantz, Professeur LJAD, UCA.
Vitaly Volpert, Directeur de recherche CNRS.
Nejib Zemzemi, CR Carmen Team, INRIA Bordeaux.
Mohamed Ziani, MDC HDR Université Mohammed V.

Modélisation de l'écoulement sanguin coronaire à l'aide d'un modèle de fluide non Newtonien: estimation de la fraction de réserve fluide

Jury:

Président du jury
Olivier Pantz, Professeur, Laboratoire de Mathématiques, Université Côte d'Azur, Nice.
Rapporteurs
Soumaya Boujena, Professeur, Université Hassan II-Faculté des Sciences Ain Chock, Casablanca, Maroc.
Vitaly Volpert, Directeur de recherche au CNRS, Institut
Camille Jordan, UMR 5208 CNRS, University Lyon 1 (absent).
Examinateurs
Mohamed Ziani, MDC HDR, Université Mohammed V, Rabat, Maroc.
Nejib Zemzemi, CR1, équipe CARMEN Inria Bordeaux.

Remerciements

Je tiens à remercier toutes les personnes qui ont contribué à l'aboutissement de cette thèse et qui m'ont aidé à mener à bien mes travaux de recherche. Tout d'abord, je voudrais exprimer ma profonde gratitude envers mes deux directeurs de thèse. Je remercie chaleureusement Professeur Rajae ABOULAICH pour sa gentillesse, sa disponibilité, son aide et soutien sur les plans personnels et professionnels. C'est grâce à elle que j'ai pu découvrir le domaine des biomathématiques. Je souhaite aussi exprimer ma reconnaissance envers Professeur Abderrahmane HABBAL pour sa confiance, sa gentillesse, et sa disponibilité. Je remercie également Docteur Chérif Abdelkhirane de m'avoir proposé un sujet aussi riche et intéressant et d'actualité. C'est grâce à son expertise clinique que j'ai pu cerner les différents aspects liées à la circulation cardiovasculaire. Ses conseils et orientations m'ont aidé à améliorer la qualité de mon travail.

Je remercie ensuite Professeur Soumaya BOUJENA et Professeur Vitaly VOLPERT d'avoir accepté d'être rapporteurs de cette thèse. Je les remercie pour l'attention et le temps qu'ils ont accordés à mon manuscript. Mes remerciements s'adressent également à Professeur Olivier PANTZ, Professeur Nejib ZEMZEMI et Professeur Mohamed ZIANI de m'avoir fait l'honneur d'accepter de participer au jury de cette thèse.

Je remercie également l'équipe CARMEN de l'INRIA de Bordeaux de m'avoir donné l'opportunité d'effectuer différents stages au cour de cette cotutelle. Particulièrement Mr. Nejib ZEMZEMI pour les collaborations fructueuses sur différentes questions.

Je remercie aussi le laboratoire Jean Alexandre Dieudonné pour m'avoir accueilli dans ses locaux et donné l'accès à ses ressources de calcul. Mes sincères remerciements vont aussi aux deux ingénieurs informatiques du laboratoire: Mr. Jean-Marc LACROIX et Mr. Roland RUELLE pour leur accueil et leur accompagnement tout au long de la phase du calcul parallèle.

Finalement je remercie l'équipe ACUMES et l'INRIA Sophia Antipolis pour m'avoir accueilli dans ses locaux et donné l'accès à ses ressources. Je remercie particulièrement Mr. Mickael BINOIS pour la collaboration fructueuse.

بسم الله الرحمن الرحيم

إِنَّمَا أَمْرُهُ إِذَا أَرَادَ شَيْئاً أَنْ يَقُولَ لَهُ

كُنْ فَيَكُونُ

سوره یس

Dédicaces

Je dédie ce modeste travail et ma profonde gratitude à ma très chère maman et mon très chère père.

Résumé

Dans cette thèse, nous explorons la possibilité d'une évaluation virtuelle des sténoses à travers la simulation de l'index de la réserve coronaire - appelée FFR en anglais - qui est un outil indispensable mais contraignant lors du diagnostic. Tout d'abord, nous utilisons un modèle d'écoulement 2D non Newtonien, puis un modèle d'interaction fluide structure faiblement couplé pour établir une étude préliminaire des principales caractéristiques de l'écoulement dans une portion sclérosée. Nous introduisons ensuite une méthodologie pour estimer la FFR virtuelle par analogie avec le dispositif médical. Le capteur FFR a été, dans un premier lieu, considéré non physique (intégré au domaine d'écoulement). Nous avons mené différents tests numériques pour relever les facteurs affectant la FFR virtuelle et présenté son profil par rapport aux différents paramètres considérés pour la lésion. Deuxièmement, nous présentons deux géométries réalistes : un arbre coronaire gauche - en 2D - obtenu à partir de la segmentation d'une image angiographique et une bifurcation en 3D. Nous définissons des modèles d'écoulement généralisés à l'intérieur des deux géométries et considérons que la paroi artérielle est rigide. La présence de plusieurs sorties dans ces nouvelles géométries nous a conduit à utiliser un nouveau type de conditions aux limites. A l'entrée, nous proposons une fonction bi-sinusoïdal s'approchant du profil de vitesse sanguine enregistré pour un arbre coronaire gauche. En ce qui concerne les sorties du domaine, nous considérons un modèle Windkessel à 2 éléments. Nous avons mené une étude comparative entre le modèle de Navier Stokes et le modèle non Newtonien considéré et entre les conditions limites de sorties libres et le modèle Windkessel présenté en 2D et défini le flux à l'intérieur de l'arbre de bifurcation 3D. Nous calculons également la FFR virtual de deux lésions artificielles ajoutées à l'arbre coronaire et démontrons que l'angiographie seule ne suffit pas pour évaluer la sévérité de la sténose. Troisièmement, nous étudions - par modélisation 2D et 3D - une des raisons possibles de la dérive de pression pendant la mesure de la réserve coronaire FFR, représentée par la position et la configuration arbitraires du capteur de pression. Le capteur est considéré durant cette étude extrinsèque au domaine de l'écoulement. Nous considérons les mêmes modèles de flux non Newtoniens que précédemment. En 2D, le capteur FFR est assimilé à un disque avec une position variable incorporée dans l'arbre coronaire gauche. Alors que le domaine 3D correspond à une portion artérielle sclérosée à laquelle

on introduit un tube 3D déformé (guide + capteur) avec une longueur et un coefficient de fléchissement donnés. L'effet de fléchissement du tube est obtenu grâce à un problème élastique basé sur la loi de Hooke. À l'aide d'un processus gaussien, nous modélisons le FFR en fonction des variables du capteur - et deux autres variables de la lésion - nous effectuons un ensemble d'expériences correspondant à l'espace d'hypercube considéré. Les données 2D indiquent une bonne précision pour la prédiction de FFR tandis que les données 4D confirment le fait que les micro-cathéters avec des diamètres importants surestiment la gravité des lésions. Les résultats obtenus démontrent que la dérive qui se produit en raison de la configuration variable du dispositif FFR peut induire en erreur lors de la classification de la sténose. Tous les algorithmes de résolution et les outils de simulation ont été implémentés sous le logiciel FreeFem++. Le besoin de plus d'espace mémoire pour les simulations 3D nous a conduit à adopter une stratégie de résolution parallèle utilisant FreeFem+++ MPI et le solveur MUMPS.

Mots clés: Écoulement non Newtonien; Fraction de réserve coronair; Athérosclérose; Processus gaussiens; Dérive.

Abstract

In this thesis, we explore the possibility of virtual coronary stenosis assessment, through the simulation of Fractional Flow Reserve (FFR) measurement, that is an indispensable but binding tool during diagnosis. First, we use a 2D non Newtonian flow model, and later a weakly coupled FSI model to make a preliminary study of the main features of flow over a stenotic coronary arterial portion. We then introduce a methodology to estimate the virtual FFR in analogy with the clinical device. The FFR device was considered non-physical (integrated to the flow domain) at a first place. We led different experiments to enumerate the factors affecting the virtual FFR and computed its profiles with respect to different lesion's parameters. Second, we consider two realistic geometries: a 2D left coronary tree obtained from the segmentation of an angiography image and a 3D bifurcation tree. We define generalized flow models inside the two geometries and consider the arterial wall to be rigid. The presence of several outlets in these new geometries led us to define a new type of boundary conditions. For the inlet, we propose a bi-sinusoïdal function approaching the velocity profile recorded inside a left coronary tree. For the outlets, we implement a 2 element Windkessel model. We led a comparative study between Navier Stokes and the flow model considered and between free outlets boundary conditions and Windkessel model in 2D and define the flow inside the 3D bifurcation tree. We also compute the virtual FFR of two artificial lesions added to the coronary tree and demonstrate that angiography alone is not enough to evaluate the severity of stenosis. Third, we investigate - through 2D and 3D modelling - one possible reason of pressure drift during FFR measurement, that is the arbitrary position and configuration of the FFR device, considered during this study extrinsic to the flow domain. We consider the same non Newtonian flow models as previously. In 2D, the FFR device is assimilated to a disk with a variable position incorporated inside the left coronary tree. While the 3D domain corresponds to a diseased arterial portion to which we introduce a deformed 3D tube (wire+sensor) with a given length and coefficient of bending. The bending effect of the tube is obtained thanks to an elastic problem based on Hooke's law. Using a Gaussian process, we model the FFR depending on these variables - and two additional stenosis variables later - we perform a set of samples corresponding to the design space considered. The 2D data indicates a good accuracy for FFR prediction while the 4D data emphasis the fact that mi-

crocatheters with important diameters overestimate lesion's severity. The results obtained demonstrate that drift occurring because of the variable device configuration may lead to stenosis misclassification. All resolution algorithms and simulation tools were implemented under FreeFem++ software. The need of more space memory for 3D simulations led us to adopt a parallel resolution strategy using FreeFem++ MPI and MUMPS solver.

Key words: Non Newtonian flow; Fractional Flow Reserve; Atherosclerosis; Gaussian processes; Drift.

Contents

List of Figures

List of Tables

Chapter 1

Introduction

Cardiovascular diseases (CVDs) are the major cause of death globally, killing more than 17.9 million worldwide, according to WHO (World Health Organization). Therefore, 31% of total global mortality is due to cardiovascular diseases. An estimated 7.4 million are due to coronary heart disease and 6.7 million to a stroke (2015). Atherosclerosis is one of the most common pathologies that lead to stroke. It is a chronic inflammatory disease that affects the entire arterial network and especially the coronary arteries. It is an accumulation of fat cells and lipids over the arterial surface due to a dysfunction of the endothelial layer (finer superior layer of blood vessel). The grassy deposit is commonly known as plaque or lesion in clinical context. The objective of clinical intervention in this case is to establish a revascularization, in order to allow the blood to circulate in a normal way among the diseased vessel. The first problem we were interested in during this thesis was the multidisciplinary optimization of drug-eluting stents. The objective was to find the optimal design (topology and characteristics) of the stent which ensures a permanent enlargement of the damaged portion while reducing the risks induced by the immune reactions of the arterial wall (restenosis, thrombosis ...). In order to have a good understanding of the pathology and the clinical processes associated with it, a contact with practitioners in the field of interventional cardiology was required. Here we tried to have contact with AMCAR, the Moroccan association of cardiology in Casablanca. They put us in contact with Dr. Chérif Abdelkhirane, a specialist in stenting and interventional cardiology, head chief of the clinical center Cardiology Maarif in Casablanca at the time, and now head of the department of Interventional Cardiology, Clinique des spécialités Achifaa, Casablanca, Morocco. From the very first discussions, we could realize that what matters the most from a cardiologist's point of view is to ensure a better revascularization. While the stent design, according to them, is not determinant of the post-intervention results. Especially that the stents available in the market are enough sophisticated. That is why he suggested a new problematic for the thesis. Indeed, revascularization is based on the principle of remedying ischemia, that is the decrease or the interruption of

oxygen supply to the organs. This anomaly - ischemia- is attenuated by the presence of more than one lesion (multivariate patients), which can lead to several complications. The key to a good medical intervention is establishing a good diagnosis. During the diagnosis phase, the cardiologist uses several techniques for decision making, among which angiography is the most intuitive. Angiography is an X-ray technique to visualize the inside (the lumen) of blood vessels in order to identify vessel narrowing: stenosis. Despite its widespread use, angiography is often imperfect in determining the physiological significance of coronary stenosis. The clinical decision is based on the degree of stenosis, that corresponds to the plaque's height over the diameter of reference of the diseased arterial portion. If the problem remains simple for minimal lesions ($\leq 40\%$) or very severe ($\geq 70\%$), a very important category of intermediate lesions must benefit from a hemodynamic evaluation in order to determine the outcomes of revascularization. Fractional Flow Reserve (FFR) can be a better alternative in this case.

In the first chapter, we give the necessary elements to define the context of our work. Firstly, some clinical precisions about the pathology of atherosclerosis and the methods of diagnosis and treatment. Secondly, we establish a state of the art of the works that were interested in the simulation of blood flow.

In the second chapter of this thesis, we provide a first estimation of a virtual non-invasive Fractional Flow Reserve (VFFR). We present a preliminary study of the main features of flow over a stenosed coronary arterial portion, in order to enumerate the different factors affecting the VFFR, and to emphasis considering other parameters than the degree of stenosis to judge the severity of a coronary lesion. In particular, the lesion radius, as demonstrated by the clinical study given in [17]. We adopt a non Newtonian flow model inside a 2D simplified domain assumed to be rigid in a first place, corresponding to the artery geometry in maximum vasodilation. In a second place, we consider a simplified weakly coupled FSI model in order to take into account the infinitesimal displacements of the upper wall. No large displacements are taken into account. A 2D finite element solver was implemented using Freefem++. We computed the VFFR profiles with respect to different lesion parameters and compared the results given by the rigid wall model to those obtained for the elastic wall one.

In the third chapter, we adopt realistic domains, issued from reconstructed coronary trees. Two geometries were adopted: the first one corresponds to a 2D left coronary tree, issued from an angiography, to which we included two artificial lesions of different degrees. The second one is a 3D bifurcation to which we add an artificial lesion. We used the same generalized fluid model as in the first chapter with a Carreau law in 2D and 3D, but addressed a special concern to boundary conditions. We use a coupled multidomain method based on a 2 element Windkessel model as outlet boundary condition. At the inlet, instead of using a wave form function, we opted for a double-sinusoïdal profile similar to flow data curves

from a left coronary tree. We introduce our methodology to quantify the virtual FFR, and lead several numerical experiments. We compare FFR results in 2D for Navier Stokes versus generalized flow model, and for Windkessel versus free outlets boundary conditions. In the fourth chapter, we try to study the impact of the pressure wire design and configuration on the computed FFR value, in order to quantify the uncertainties induced in the measure. Inside a 3D domain modelling a diseased coronary portion, we insert a microcatheter-design sensor to capture the proximal and distal pressures. We use a generalized 3D fluid model and we run different simulations to enumerate the effect of the sensor's configuration on the estimated FFR. Gaussian processes are then used to provide a statistical model to predict the FFR value.

Scientific production

Publications

- K.Chahour, R.Aboulaich, A.Habbal, C.Abdelkhirane and N.Zemzemi "Numerical simulation of the fractional flow reserve (FFR)", Math. Model. Nat. Phenom. 13 (2018).
- K.Chahour, R.Aboulaich, A.Habbal, C.Abdelkhirane and N.Zemzemi "Virtual FFR quantified with a generalized flow model using Windkessel boundary conditions: Application to a patient-specific coronary tree", Computational and Mathematical Methods in Medicine (submitted in August 2019).
- K.Chahour, A.Habbal, M.Binois, R.Aboulaich and C.Abdelkhirane "Drift quantification during fractional flow reserve measurement using Gaussian processes" (final stage of writing).
- C. Bonnet, K. Chahour, F. Clément, M. Postel, R.Yvinec "Multiscale population dynamics in reproductive biology: singular perturbation reduction in deterministic and stochastic models ", ESAIM PROCS (accepted in July 2019).

Communications in international conferences

- October 2018 – BIOMATH 2018: Hassan II University, Mohammedia Morocco. "Realistic blood flow simulation in a 2D reconstructed coronary tree"
- June 2018 – PICOF'18: American University of Beirut, Beirut, Lebanon. "Simulation of blood flow in a stenosed artery and fractional flow reserve computation"
- October 2017 – ICAM'17: Faculty of science and technology Taza, Morocco. "Numerical simulation of the fractional flow reserve (FFR)"

Chapter 2

Preliminary

Abstract

Blood flow simulation inside diseased coronary arteries is a crucial task before computing the virtual Fractional Flow Reserve (FFR). In this preliminary chapter, we highlight some clinical aspects of coronary blood circulation, atherosclerosis and the invasive FFR measurement. On the other hand, we establish a state of the art of the works in applied mathematics that investigated in this view in order to enumerate the elements to be considered to better modelize our problem.

2.1 Clinical context

2.1.1 Atherosclerosis

Atherosclerosis is a chronic inflammatory disease that affects the entire arterial network and especially the coronary arteries. It is an accumulation of fat cells and lipids over the arterial surface due to a dysfunction of the endothelial layer (finer superior layer of blood vessel). The grassy deposit is commonly known as plaque or lesion in clinical context. The objective of clinical intervention in this case is to establish a revascularization, in order to allow the blood to circulate in a normal way among the diseased vessel. Different angioplasty techniques can be envisaged, among which implantation of stents is the most widespread. The cardio-stent is a small metallic tube that has generally a periodic design composed by a repeated pattern. It acts like a scaffold to support the inside of the diseased portion of artery. The intervention, called stent implantation, consists on introducing a stent into the damaged arterial portion. The stent is placed over a balloon catheter, that is placed over a guide wire, in order to be brought into the site of the plaque. Once there, the balloon is inflated and the stent expands to the size of the artery and holds it open. The balloon is then deflated and removed while the stent stays in place.

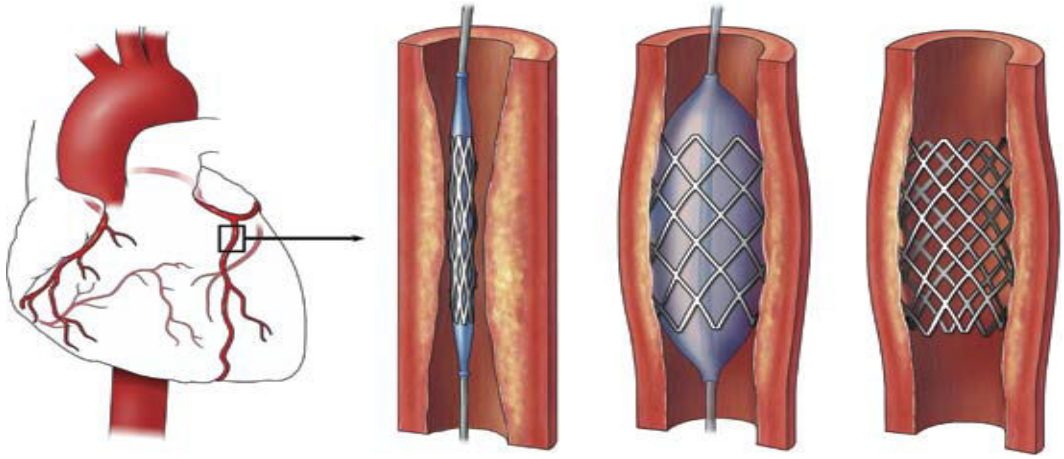

Figure 2.1: Angioplasty : stent implantation, [37]

The physical characteristics as well as the geometric design of the stents in industries involved so that this last could have an optimal performance once placed on the site of atherosclerosis. Combining different criterias: flexibility, manageability, opacity, inoxidability, bio-compatibility... Two potential post-stenting risks are intra-stent restenosis and thrombosis, see [52]. Restenosis is due to an excessive tissue proliferation in the luminal surface of the stent, leading to a reduction in lumen diameter after coronary intervention. Thrombosis is an acute consequence to restenosis in the case where a part of cells is liberated from the lumen surface to form an occlusion and lead to stroke. In order to reduce these

risks, a new generation of drug-eluting stents has appeared. A drug eluting stent is nothing else but a stent covered by a fine layer of polymer containing an antiproliferative substance.

2.1.2 Fractional Flow Reserve

Fractional Flow Reserve (FFR) is a lesion specific, physiological index determining the hemodynamic severity of intracoronary lesions. FFR can accurately identify lesions responsible for ischemia which in many cases would have been undetected or not correctly assessed by angiography alone. FFR is defined as the maximum achievable blood flow in stenotic coronary artery (Pd) divided by maximum blood flow in the same artery without stenosis (Pa). FFR has a unique normal value of 1.0 in healthy coronary artery. An $FFR = 0.80$ is commonly accepted as the threshold below which a lesion is considered ischemia causing. The invasive FFR measurement is established during maximum hyperemia, administrated by adenosine stimulus. It is only at maximal hyperemia that resistance is minimal and that flow develops a linear relationship to pressure, a vital prerequisite for the FFR equation to hold true. Not achieving maximal hyperaemia will overestimate the FFR value and therefore underestimate the true severity of a coronary stenosis. More technical details about the FFR clinical test and the FFR device will be given in the next section 2.1.4. As demonstrated by multiple clinical studies, particularly FAME study [11], FFR is the current gold standard to improve clinical decision making in the case of coronary stenosis. Using a patient data collected from more than 20 medical centers in the united states and Europe, patients were randomly assigned to undergo with stent implantation guided by angiography alone or guided by FFR measurement in addition to angiography, see [11]. The conclusion of FAME study is that the FFR improved the clinical outcomes and contributed in reducing the mortality rate.

2.1.3 Blood circulation in the heart

Blood is a complex mixture of blood cells suspended in blood plasma. Plasma, which constitutes 55% of blood fluid, is mostly water (92% by volume), contains proteins, lipoproteins, and ions by which nutrients and wastes are transported to the different organs. Red blood cells comprising approximately 40% of blood by volume are small semisolid particles. They are responsible of increasing the viscosity of blood that is four times more viscous than water. Blood does not exhibit a constant viscosity at all flow rates and thus has a non-Newtonian behavior especially in the microcirculatory system, such as the coronary arteries. However, in large arteries like the aorta, blood behaves in a Newtonian fashion, and the viscosity can be considered constant. In this work, we give a special concern to the coronary arteries.

Coronary arteries, see figure 2.2 constitute the vascular system that supplies oxygen to the heart muscle, called myocardium. The aorta branches off into two main coronary blood vessels. These coronary arteries glued to the heart muscle branch off themselves into smaller arteries and capillaries that transport oxygen-rich blood. The right coronary artery supplies blood mainly to the right side of the heart. The right side of the heart is smaller because it pumps blood only to the lungs. The left coronary artery, which branches into the left anterior descending artery and the circumflex artery, supplies blood to the left side of the heart. The left side of the heart is larger and more muscular because it pumps blood to the rest of the body.

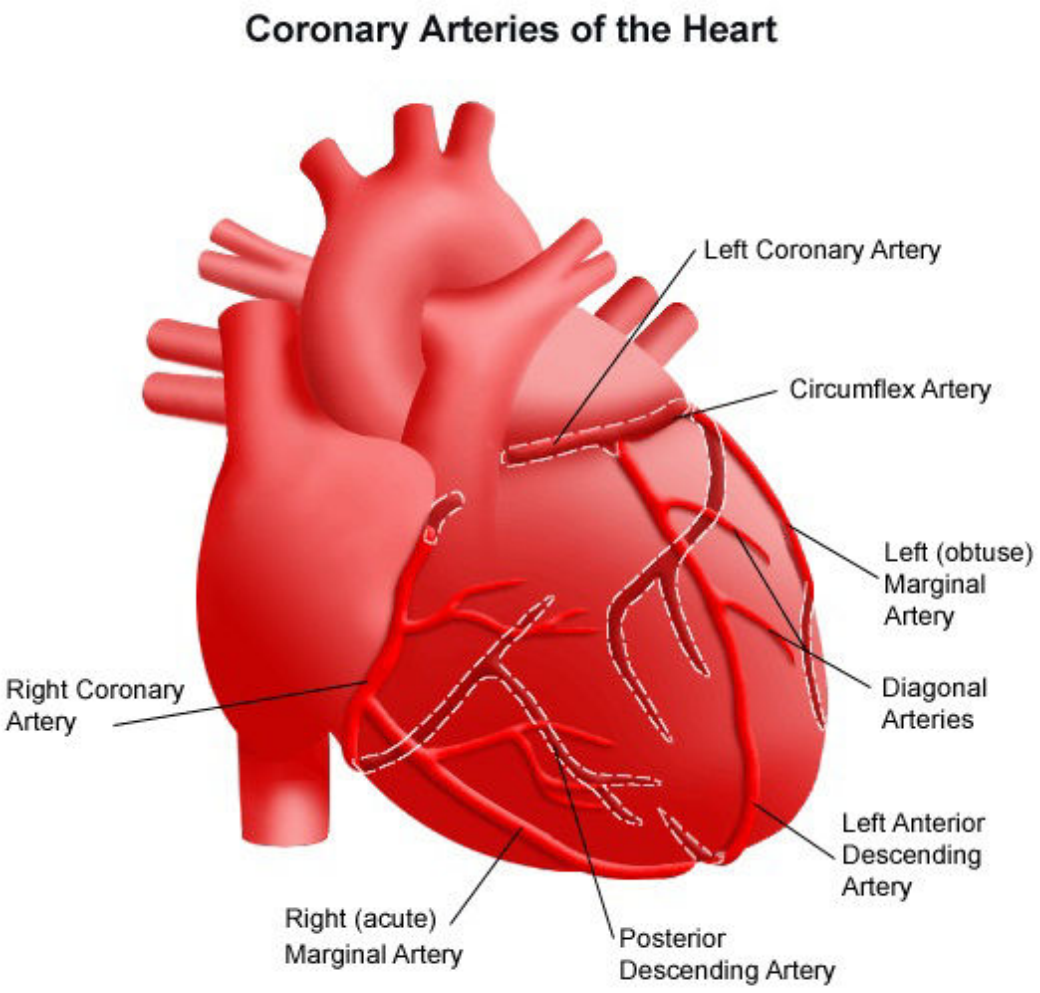

Figure 2.2: The right and left coronary arteries of the heart.

Blood flow and pressure are unsteady. The cyclic nature of the heart pump creates pulsatile conditions in all arteries. The heart ejects and fills with blood in alternating cycles called systole and diastole with a frequency of 75 beats per minute. Blood is pumped out of the heart during systole while the heart rests during diastole, and no blood is ejected. A

heart cycle lasts about 0.8 seconds, systole occupies the third while diastole occupies the two thirds.

During systole, intramuscular blood vessels are compressed and twisted by the contracting heart muscle and blood flow to the left ventricle is at its lowest. The force is greatest in the sub-endocardial layers where it approximates to intramyocardial pressure, figure 2.3. In systole intramyocardial blood is propelled forwards towards the coronary sinus and retrogradely into the epicardial vessels, which act as capacitors. Flow resumes during diastole when the muscle relaxes. The coronary perfusion pressure is the difference between the aortic diastolic pressure and left ventricular end-diastolic pressure (LVEDP). Phasic changes in blood flow to the right ventricle are less pronounced because of the lesser force of contraction.

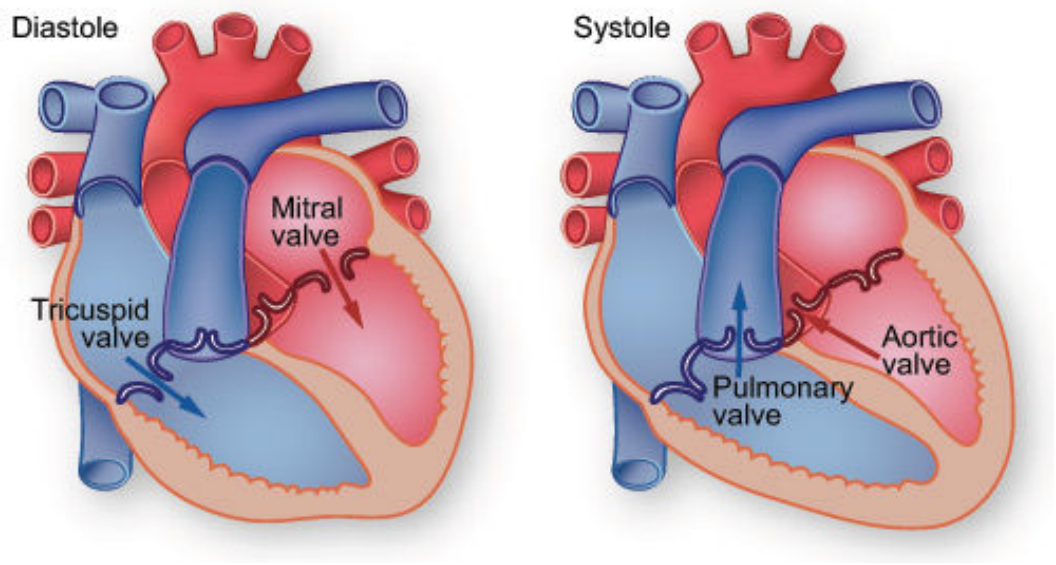

Figure 2.3: Systole and diastole refer respectively to the contraction and relaxation of the two right or left ventricles of the heart.

Central venous pressure may be a more appropriate choice for downstream pressure to calculate the right-sided coronary perfusion pressure. Pressure and flow have characteristic pulsatile shapes that vary in different parts of the arterial system, as illustrated in Figure 2.3. The flow out of the heart is intermittent, going to zero when the aortic valve is closed. The aorta, the large artery taking blood out of the heart, serves as a compliance chamber that provides a reservoir of high pressure during diastole as well as systole. Thus the blood pressure in most arteries is pulsatile, yet does not go to zero during diastole. In contrast, the flow is zero or even reversed during diastole in some arteries such as the external carotid, brachial, and femoral arteries. These arteries have a high downstream resistance during rest and the flow is essentially on/off with each cycle. In other arteries such as the internal carotid or the renal arteries, the flow can be high during diastole if the downstream resistance is low.

The flow in these arteries is more uniform.

2.1.4 FFR devices: FFR guidewire vs microcatheter

Despite strong outcome records, FFR is still underutilized. Areas for improvement of FFR equipement technology fall into three categories:

1. signal stability that is the main reason of pressure drift;
2. wire handling characteristics and rapid placement.
3. use of multiple wires for complex or multi-vessel assessment.

For FFR measurement, two main technologies are commercially available [35] and [54]. On the one hand, pressure wire technology that involves a special 0.014 inches wire. There are two main types of pressure wires, the most commonly used is the piezo-electrical. In this kind of pressure wires, the sensor is located at the proximal end of the radiopaque flexible wire tip (about 3 cm long). The value measured by the Piezoelectric sensor is a dynamic pressure. The approach is the following: a thin membrane over a large base is used, ensuring that an applied pressure specifically loads the elements in one direction. Deformation of the crystal generates an electrical charge, which is transmitted along thin wires inside the guidewire. The main disadvantage of this type of sensors is the potential for signal interference at connector points. To overcome the limitations given above, and especially, to improve signal stability, a new generation of optical sensors has appeared. In this case, thin optical fibers are incorporated around a metal core (e.g nitinol, cobalt chromium). The difference in pressure measurement resides in the way of measuring the membrane deflection, which is optical rather than electrical. As blood pressure increases, the membrane deflects inward, which induces a phase delay between two light beams created within the sensor assembly. It should be noticed that optical FFR wires demonstrated a much better signal stability than the piezoelectrical ones, and thus less drift during FFR assessment [**?**]. On the other hand, microcatheter technology that employs a low-profile catheter with a pressure sensor incorporating fibre-optic technology into the distal end, giving a profile comparable to 0.022 inches diameter at the lesion site. This new equipement is convenient and may overcome some of the limitations associated with conventional pressure wire systems. It may also be less prone to pressure drift since it utilizes an optical pressure sensor. However, the larger elliptic profile, see figure 2.4, is observed to produce an additive contribution to lesion severity -compared to other models of FFR devices- and as a result lower the measured FFR value [34].

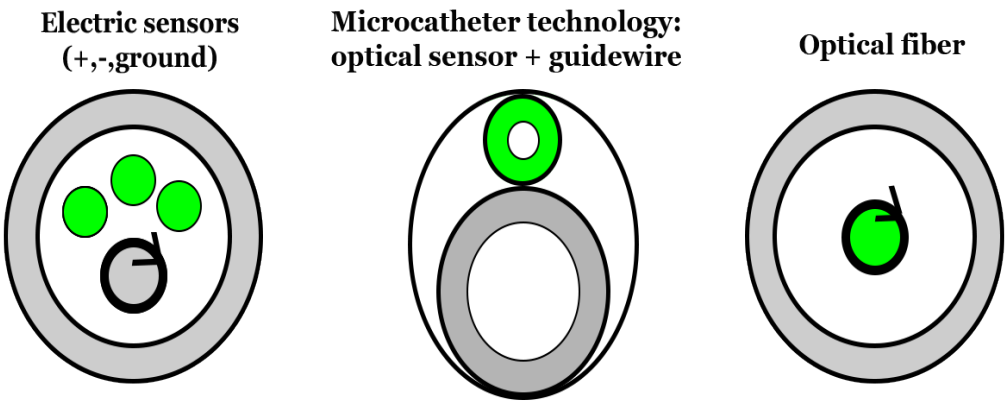

Figure 2.4: Sections of piezo-electrical sensor, microcatheter and optical sensor from left to right respectively. Left, standard wire core surrounded by thin transmission and ground wires. Center, ultra thin microcatheter using optical fiber: sensor housing + guidewire. Right, nitinol cobalt chromium wire around central optical fiber.

2.2 Mathematical context

2.2.1 Blood flow modelling

Simulating blood flow in the arterial network - and in the coronary arteries in particular - is a highly complex task. Combining different mathematical disciplines: computational fluid dynamics, elasticity and domain reconstruction. The main difficulties can be resumed in the following:

- The bio-fluid complexity of blood, and the choice of the appropriate value or formula for the viscosity term. Moreover, whether we are in large or small arteries, the choice of a Non-Newtonian flow model or Navier Stokes is crucial as to the accuracy of the solutions obtained.

- Arterial vessel walls show a so called "bioviscoelastic" behavior C302. This property has two important effects. First, the arterial wall deformation is a function of the transmural pressure and the time. Hence the “history” of the wall has an effect on the current state, according to the considered scheme.

- The geometrical complexity of the arterial network. It consists of numerous vessel branches with different length, diameter and stiffness (compliance). There are also several bifurcations in the system. Furthermore, there is a noise introduced by the large displacements of the respiratory system, constantly in contact with the heart.

During the last decades fluid mechanics has become a powerful tool in the analysis of arterial blood flow. A flow and pressure wave starts from the heart to cross all major arteries in which it is damped, dispersed and reflected due to changes in vessel sizes, as well as the properties of the tissues and branches. The propagation of the blood wave in the different arteries creates small displacements of the arterial wall due to its elastic property. That said, a realistic reproduction of blood flow in the coronary arteries involves:

- **Taking into account the fluid and the arterial wall particularity :** On one hand, the choice of a Newtonian fluid model using the Navier Stokes equations for example, under certain conditions, or Non Newtonian. The work in [51] presents some recent developments in blood flow modelling and gives a special concern to the non Newtonian properties of blood. In the case of sclerotic arteries, the problem becomes more complex. More details about the inflammatory process that initiates atherosclerosis are given in [50]. On the other hand, the choice of a fluid-structure coupling model that takes into account the interaction between the arterial wall and the blood. These 2D and 3D coupling models were presented in several papers [1] [2][3] [5] [8]. Among them [1] [2] introduced the presence of stenosis.

- **The choice of suitable boundary conditions for the inlets and the outlets of the system:** Various studies have tackled the problem of boundary conditions in the case of the blood flow [3] [4] [6] . These last, if they do not agree with the problem posed and its geometrical configuration can cause stability problems due to the creation of reverse flow, which does not correspond to the physical reality of the flow. Indeed, the difficulty resides in the fact of isolating a part of a network which is in fact closed, and in which the flow is periodic. The boundary condition at the inlet is often a sinusoïdal, parabolic or a spline function extracted from a medical data. At the outlet, the most common boundary condition are constant pressure or traction with a velocity profile. In the case of complex geometries, or 3D domains reconstructed from medical imaging, in which there are several evacuations, the condition at the outlet boundary must be chosen in order to avoid having inaccurate values of pressure and velocity. The best boundary conditions in the outlet for cardiovascular flow applications are not those which do not produce reflections, since reflections naturally come from the change in the vessels caliber, bifurcations, variation in the properties of the wall ... etc, which produces a resistant effect at the exit of the large vessels. For this reason, the boundary conditions based on the impedance and resistance models are the most adapted to incorporate this reflected wave effect into the model.

- **The choice of adapted resolution strategies:** Numerical methods to solve this kind of coupled problems are very diverse, but the finite element method remains the most

used to solve this kind of problems. To describe the mobile domain in 2D or 3D, often an Arbitrary Lagrangian-Eulerian (ALE) coupling scheme is used, as was done in the works [5][7] [8] . In [8] as in other works based on this type of formulation, proceded by decoupling the problem into two parts: solid and fluid, introducing additional boundary conditions at the interface. These types of resolution strategies allowed to obtain rather stable patterns [8] while reducing the computational cost.

- **The choice of realistic values for the parameters:** The stability of this kind of schema also depends on the selected temporary parameters (End time, time step ... etc) which must be consistent with the periodicity of the flow and the duration of the cardiac cycle. And also of the fluid and elastic parameters considered. In [7] , as in [12] , we were interested to the estimation of the different parameters involved in the case of blood flow, adopting reverse problem type methods and optimization.

- **Using realistic domains for simulations:** There are different approaches to reconstruct 3D vessels from 2D images. The most widspread are those that are based on images corresponding to different slices of the 3D object: mainly CT scans or MRI. Another 3D reconstruction technique is based on different projections of the 3D vessel, issued from 2D angiography, like presented in [48] and [13]. This second methodology consists on segmenting the set of initial images corresponding to each projection plane, then obtaining the centerlines and defining a centerline skeleton in 3D through a connectivity metric. At each center point of the skeleton, a circle is defined, its radius is approximated from the initial projections images, see [49].

2.2.2 Virtual Fractional Flow Reserve

Despite the established evidence that Fractional Flow Reserve (FFR) has clinical benefits, it remains an underutilized tool in interventional practice. Potential barriers may be summarized in the additional procedure time required, need for adenosine administration, as well as additional cost that are not covered by insurances. Statistically, it is used in less than 10% of the cases. A tool that could accurately and rapidly calculate FFR without the need of expensive requirements - mainly the pressure wire- would make this physiologic index become available to a wider population. In this regard, computational fluid dynamics (CFD) has been applied to realistic geometries issued from coronary computed tomography to estimate a new virtual FFR [9] [10]. This new attractive and non-invasive alternative is a potential key to overcome the limitations cited above. However, there are many challenges that need to be overcome before vFFR can be translated into clinical routine. The virtual FFR is based on coronary angiographies to reconstruct the domain in 3D using diverse segmentation meth-

ods. As well as the models of computational fluid dynamics to describe the flow, such as the Navier Stokes equations [10]. Notwithstanding, the primary scientific limitations to this kind of work lies in the phase of 3D reconstruction of the coronary arterial tree, in which there are many information loss due to the noise initially present in the images (because of the twisting of the arteries, and the movement induced by the respiratory system when acquiring images). Especially if the validation method consisted on matching the values resulting from simulation with those of the clinical FFR test, which gives rise to a statistical study, as in [10]. Firstly, the segmentation method used is decisive as to the accuracy of the 3D geometric model obtained [13]. Secondly, as cited above, the choice of appropriate boundary conditions is paramount. And as long as we base on angiographies corresponding to a particular patient to reconstruct the 3D geometrical model, it is also necessary to choose patient-specific boundary conditions.

In the next chapter, we will use a non Newtonian fluid model - the same as in [1] - coupled to a fluid structure interaction model (see [4]) to simulate blood flow inside a sclerotic arterial portion. Then we introduce a computational methodology to compute the virtual fractional flow reserve in analogy with the clinical device based on the pressure features obtained previously. A set of samples are established to investigate the effect of the lesion's parameters on the FFR value computed.

Chapter 3

Virtual Fractional Flow Reserve (VFFR) computation

Abstract

The Fractional Flow Reserve (FFR) provides an efficient quantitative assessment of the severity of a coronary lesion. Our aim is to address the problem of computing virtual non-invasive fractional flow reserve VFFR. In this chapter, we present a preliminary study of the main features of flow over a stenosed coronary arterial portion, in order to enumerate the different factors affecting the VFFR. We adopt a non Newtonian flow model and we assume that the 2D domain is rigid in a first place. In a second place, we consider a simplified weakly coupled FSI model in order to take into account the infinitesimal displacements of the upper wall. A 2D finite element solver was implemented using Freefem++. We computed the VFFR profiles with respect to different lesion parameters and compared the results given by the rigid wall model to those obtained for the elastic wall one.

3.1 Introduction

The technique of the fractional flow reserve FFR has derived from the initial coronary physical approaches decades ago. Since then, many studies have demonstrated its effectiveness in improving the patients prognosis, by applying the appropriate approach. Its contribution in the reduction of mortality was statistically proved by the FAME (Fractional Flow Reserve Versus Angiography for Multivessel Evaluation) study [11]. It is established that the FFR can be easily measured during coronary angiography by calculating the ratio of distal coronary pressure P_d to aortic pressure P_a. These pressures are measured simultaneously with a special guide-wire. FFR in a normal coronary artery equals to 1.0. FFR value of 0.80 or less identifies ischemia-causing coronary lesions with an accuracy of more than 90% [11]. Obviously, from an interventional point of view, the FFR is binding since it is invasive. It should also be noted that this technique induces an additional cost and time as explained in the preliminary chapter. In this perspective, a new virtual version of the FFR, entitled VFFR, has emerged as an attractive and non-invasive alternative to standard FFR, see [9, 10]. However, there are key scientific, logistic and commercial challenges that need to be overcome before VFFR can be translated into routine clinical practice.

As precised in the first chapter 2, blood circulation is generated by the heart "pump" that produces consecutive contraction/relaxation movements. These movements are performed during what we call a cardiac cycle. It consists of two phases: the systole, that is the phase of contraction. It occupies about one third of the cardiac cycle. The diastole, during which the heart muscle relaxes and refills with blood. It lasts the two remaining thirds of the cardiac cycle. Assuming a healthy heart and a typical rate of 70 to 75 beats per minute, each cardiac cycle takes about 0.8 second. A flow and pressure wave starts from the heart to cross all major arteries in which it is damped, dispersed and reflected due to changes in vessel sizes, as well as the properties of the tissues and branches. The two coronary arteries cover the surface of the heart and represent the first derivations of the general circulation, see figure 2.2.

3.2 Fractional flow reserve

In order to provide a good estimation of the VFFR, a good understanding of the FFR technique as well as the various medical verifications preceding the test is required. In this section, we give details about the invasive FFR. The patient is initially placed in the supine position. To start the measure of the fractional flow reserve (FFR) the operator crosses the coronary lesion with an FFR-specific guide wire. This guide wire is designed to record the

coronary arterial pressure distal to the lesion (figure 3.1 left). Once the transducer is distal to the lesion (approximately 20 mm), a hyperemic stimulus is administered by injection through the guide catheter, and here the FFR value is subject to a wide variation. The operator waits for few minutes so that the FFR value becomes constant, this value corresponds to the maximal vasodilation.

The mean arterial pressures from the pressure wire transducer P_{aortic} and from the guide catheter P_{distal} are then used to calculate FFR ratio: $FFR = P_{distal}/P_{aortic}$ (figure 3.1 right).

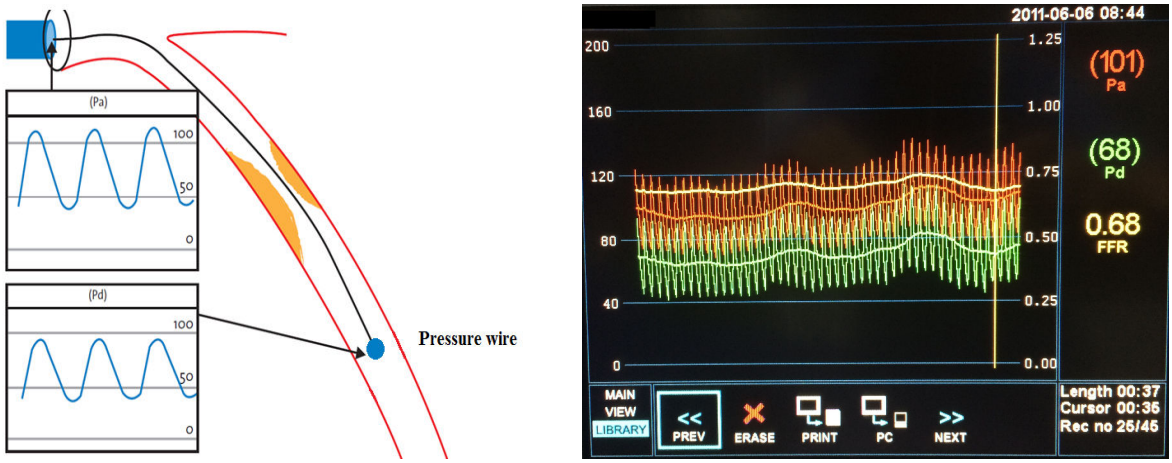

Figure 3.1: Left, representatif schema of the invasive FFR technique [16]. Right, a typical example of FFR measurement. Automated calculation of FFR corresponds to the ratio of mean distal coronary pressure (green) to mean aortic pressure (red) during maximal hyperemia, see [15].

The pressure values given by the FFR instrument are calculated as temporal mean pressures over small time intervals, depending on the frequency of acquisition of the pressure sensor $p_s(t)$. Assuming that T_c is the duration of a cardiac cycle, these pressures are given as follows:

$$P = \frac{1}{T_c}\int_0^{T_c} p_s(t)dt \tag{3.1}$$

An FFR value lower than 0.75 indicates a hemodynamically significant lesion. An FFR value higher than 0.8 indicates a lesion that is not hemodynamically significant. Values between 0.75 and 0.80 are indeterminate and should be considered in the context of patient's clinical history to determine if revascularization is necessary.

In this chapter, we aim at presenting a preliminary 2D based study to understand the flow distribution in a stenosed coronary artery and to enumerate the factors that affect the value of the VFFR. We give a special concern to the influence of the lesion's parameters.

Since we are interested in studying the flow in the coronary arteries, we decided to use

a non Newtonian flow model like in [1] and [2]. In fact, the coronary arteries have a small caliber (0.5 cm) compared to the aorta for example, where the use of non Newtonian flow model is not really crucial. In a first place, we assumed that the arterial wall is rigid. This is justified by the fact that the FFR value taken into account by the clinician during the test is established into a domain corresponding to the maximal vasodilation.

In a second place, we considered a simplified weakly coupled fluid-structure interaction model to include the arterial wall elastic behavior, as presented in [8]. The coronary arteries are subject to two different displacements:

- Large displacements: Since they are partially attached to the myocardium, they are directly influenced by the myocardium contraction/relaxation, and by the movements induced by the respiratory system.
- Small displacements: Due to the propagation of the blood wave generated by the heart pulse.

In this work, we chose to restrain our study to the small displacements. Moreover, only the upper face of the arterial portion is involved since the lower one is fixed (glued to the myocardium), see [7]. We also assume that the displacements of the shell are infinitesimal. As for the boundary conditions, even if their choice is crucial for this kind of studies, we decided to make few simplifications in order to be able to address the problem. At the inlet, we impose a sinusoïdal wave function, to illustrate the pulsatile property of the flow, as in many works [4], [8] and [7]. At the outlet, we assume that the vessel following the portion of interest is long enough before getting to the small tissues, or having a change in the vessel caliber, so there is no resistance effect. This justifies the choice of natural outlet boundary condition.

We implement from scratch, within the FreeFem++ environment, a finite element solver for both the generalized flow model and the coupled arterial wall/ blood flow model. To describe the 2D mobile domain, we used an Arbitrary Lagrangian-Eulerian (ALE) coupling scheme. Like in [7], we proceed by decoupling the problem into two parts: solid and fluid, while introducing coupling boundary conditions at the interface. We then introduce and implement an algorithm for computing the VFFR following the industrial manufacturer protocol for the analogic FFR estimation. Using the solvers, we lead a study of the VFFR with respect to the stenosis dimensioning parameters (degree of stenosis and lesion radius).
In this study, our goal is to provide a first estimation of the coronary fractional flow reserve VFFR in a simplified 2D geometry. We conduct different simulations in order to identify the impact of the lesion's parameters on the value of VFFR. In section 3.3, we present the non Newtonian flow model used to carry all the simulations, as well as the boundary conditions. In section 3.4, we give some numerical results considering that the arterial portion is rigid.

The flow and pressure distributions are given in two different geometries: a single stenosis case (presence of only one lesion), and a multi-stenosis case. In these two configurations of the domain, we plot VFFR variations according to some parameters of influence: degree of stenosis, lesion's radius, and the spacing between the two lesions in the multi-stenosis case. In section 3.5, we present the fluid-structure interaction model, and the different VFFR variations corresponding to it.

3.3 Generalized non newtonian flow model

In large arteries, blood flow can be modeled by the Navier Stokes equation. In our case, the blood cannot be assimilated to a Newtonian fluid, since the coronary vessels caliber is very small (0.5 cm). We choose a non-Newtonian flow model, as in [1]. The mathematical model was studied in [1] and authors proved the existence of a solution to this type of problems. In this chapter, we are more interested in giving a bi-dimensional based estimation of the virtual fractional flow reserve VFFR on the one hand. On the other hand, we lead different simulations, in order to explore the impact of the plaque's characteristics on the velocity and pressure fields.

We consider the Carreau law and we suppose that the viscosity varies as a function of the second invariant of the deformation tensor s(u):

$$(s(u))^2 = 2Du : Du = 2\sum_{i,j}(Du)_{ij}(Du)_{ji} \tag{3.2}$$

with:

$$Du = \frac{1}{2}(\nabla u + \nabla^T u) \tag{3.3}$$

Following the Carreau law, μ is given by:

$$\mu = \mu_\infty + (\mu_0 - \mu_\infty)(1 + (\lambda s(u))^2)^{(n-1)/2} \tag{3.4}$$

where $\mu_0 = 0.0456 \ \ Pa.s$ and $\mu_\infty = 0.0032 \ \ Pa.s$, are the values of the viscosity for the lowest and highest shear rates. $\lambda = 10.03 \ \ s$ and $n = 0.344$.

The problem considered involves the blood velocity $u = (u_1, u_2)$ and pressure p defined in $\Omega_f \times (0, T_c)$ as follows (the considered domain Ω_f is shown in figure 3.2):

$$\begin{cases} \rho_f \dfrac{\partial u}{\partial t} + \rho_f (u.\nabla)u - \nabla.(2\mu(s(u))Du) + \nabla p = 0, \ \ sur \ \ \Omega_f \times (0, T_c) \\ \nabla.u = 0, \ \ sur \ \ \Omega_f \times (0, T_c) \end{cases} \tag{3.5}$$

where ρ_f is the blood density, we impose $\rho_f = 1060 \ \ Kg.m^{-3}$ like in [1], [8].

These equations are completed with the following boundary conditions on Ω_f (n is the normal):

$$2\mu(s(u))Du.n - pn = h, \ \ sur \ \ \Gamma_{in} \times (0, T_c) \tag{3.6}$$

$$2\mu(s(u))Du.n - pn = 0, \ \ sur \ \ \Gamma_{out} \times (0, T_c) \tag{3.7}$$

$$u = 0, \ \ sur \ \ \Gamma_{\omega_1} \cup \Gamma_{\omega_2} \times (0, T_c) \tag{3.8}$$

The blood flow is initially at rest and enters the vessel by the left side Γ_{in} where a sinusoïdal pressure-wave with a maximum $P_{max} = 10^4$ Pa is prescribed during $T^* = 5.10^{-3}$ seconds. The wave's profile is set equal to a stress vector of magnitude h, oriented in the negative normal direction given by the equation:

$$h = \begin{cases} (P_{max} \times (1 - cos(2\pi t/T^*)), 0)^t, x \in \Gamma_{in}, \ \ 0 \ \ \leq t \leq T^* \\ (0,0)^t, \qquad\qquad\qquad\qquad\qquad x \in \Gamma_{in}, \ \ T^* \leq t \leq T_c. \end{cases} \tag{3.9}$$

We consider that the fixed geometry at $t = 0$ corresponds to a maximal vasodilation.

The outflow is the right boundary Γ_{out} where a zero pressure is imposed. A no-slip condition is enforced on the lower and upper boundaries Γ_{ω_1} and Γ_{ω_2}, which assume that the fluid is not moving with respect to these boundaries.

The initial condition is the solution of a steady Stokes problem with a Poiseuille flow profile at the inlet, given by the following equation:

$$u_0(y) = u_{0m} \times y/H \times (1 - y/H) \tag{3.10}$$

where $u_{0m} = 0.4 \ \ m/s$

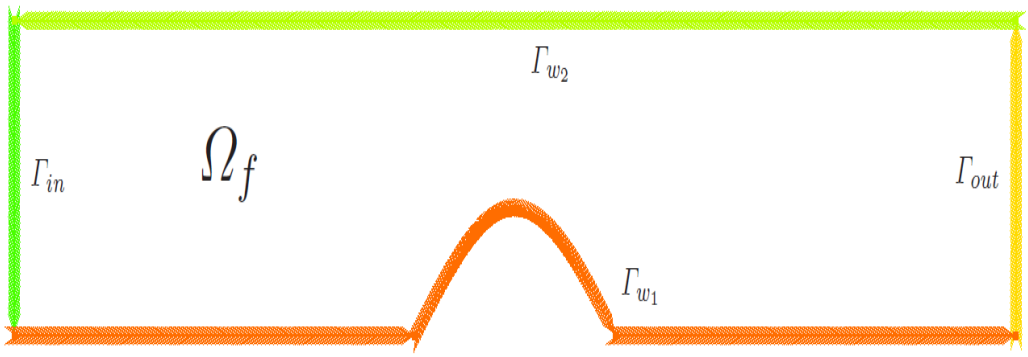

Figure 3.2: Considered geometry for the problem.

Arterial coronary plaques present a large variability in their configuration. We chose a simplified axisymmetric 2D configuration in order to address our problem, following [7]. The shape of the plaque in this case is modeled as a sinusoïdal function:

$$\omega_s(x) = \begin{cases} D \times cos(\pi(x - x_s)/2 * \delta) \;\; if \;\; x_s - \delta < x < x_s + \delta \\ 0 \qquad\qquad\qquad\qquad\qquad\qquad\qquad otherwise. \end{cases} \tag{3.11}$$

We consider a portion of a length $L = 60 \;\; mm$ from the diseased artery. The lumen diameter is considered equal to $H = 5 \;\; mm$ (coronary artery). The plaque is assumed to be 100% eccentric and it is caracterized by three parameters: D the height of the plaque, x_s the position of the center of the plaque and $2 \times \delta$ its length. $R = D/H$ indicates the degree of stenosis, it varies by changing the value of D, see 3.2.

A weak formulation of the problem can be written as follows:

$$\begin{cases} \rho_f \int_{\Omega_f} \dfrac{\partial u}{\partial t} v dx + (Au, v) + \rho_f b(u, u, v) = \int_{\Gamma_{in}} hv d\sigma + \int_{\Gamma_{\omega_1}} gv d\sigma, \;\; \forall v \in V \\ u(0) = u_0, \;\; sur \;\; \Omega_f \end{cases} \tag{3.12}$$

where V is the Hilbert space like introduced in [1], defined by:

$$V = \{v \in (H^1(\Omega_f))^2 | \nabla . v = 0 \;\; in \;\; \Omega_f, v = 0 \;\; on \;\; \Gamma_{\omega_1} \cup \Gamma_{\omega_2}\}$$

with:

$$(Au, v) = \int_{\Omega_f} 2\mu(s(u))Du : Dvdx, \tag{3.13}$$

$$b(u, v, w) = \sum_{i,j=1}^{2} \int_{\Omega_f} u_i \frac{\partial v_j}{\partial x_i} w_j dx \tag{3.14}$$

Simulations are performed using the finite element solver Freefem++, based on a semi-implicit time discretization scheme. Fluid velocity and pressure are calculated at each time step. A comparison with the Newtonian flow is established for both the blood velocity and pressure. The time step is $\delta t = 5.10^{-3}s$ and the duration of a cardiac cycle is $T_c = 0.8\ \ s$. Five consecutive cardiac cycles were simulated to ensure that the flow was truly periodic. To confirm the independence of the numerical solutions on the space discretization, computations were repeated for different mesh sizes.
In order to visualize the impact of the plaque's characteristics on the flow over the diseased portion of the artery, the degree of stenosis R varies from 40% to 70% (focusing only on the intermediate lesions). The plaque's radius also varies from 2.5 mm to 5mm. Since the presence of many lesions is clinically frequent, we have also considered a geometrical model with two plaques to get an estimation of the velocity and pressure field variations in this case.

3.4 Numerical results

3.4.1 The case of single stenosis

The simulation of blood flow in the presence of stenosis in a two-dimensional geometry has been the subject of several works [1], [7] and [14]. These works were based on the Navier Stokes model and the arterial wall was considered to be rigid. In our work, we consider a non Newtonian flow model, as in [1]. In this first simulation the arterial wall is considered to be rigid. In figure 3.3, we give velocity and pressure distribution using Navier Stokes model, in a first place, and using the generalized flow model in the second. The length of the plaque is $10\ \ mm$, and the degree of stenosis is 40%. Velocity arrows show the flow profile across the portion of the vessel. We can see reverse flow on the distal side of the plaque. Severe stenosis leads to high flow velocity, high pressure at the throat of the lesion, and a large re-circulation region distal to it.

For the calculation of the VFFR ratio, the aortic pressure P_a is calculated at each time step by the spatial mean pressure of the nodes at $1\ \ cm$ from the inlet of the vessel: $x_a = 1\ \ cm$. Whereas the distal pressure P_d is obtained at $1\ \ cm$ after the lesion: $x_d = x_s + 1\ \ cm$. Then a temporal mean is performed during the cardiac cycle: Mean P_a and mean P_d are then used to calculate the VFFR ratio. The following setting (figure 3.4) describes the approach:

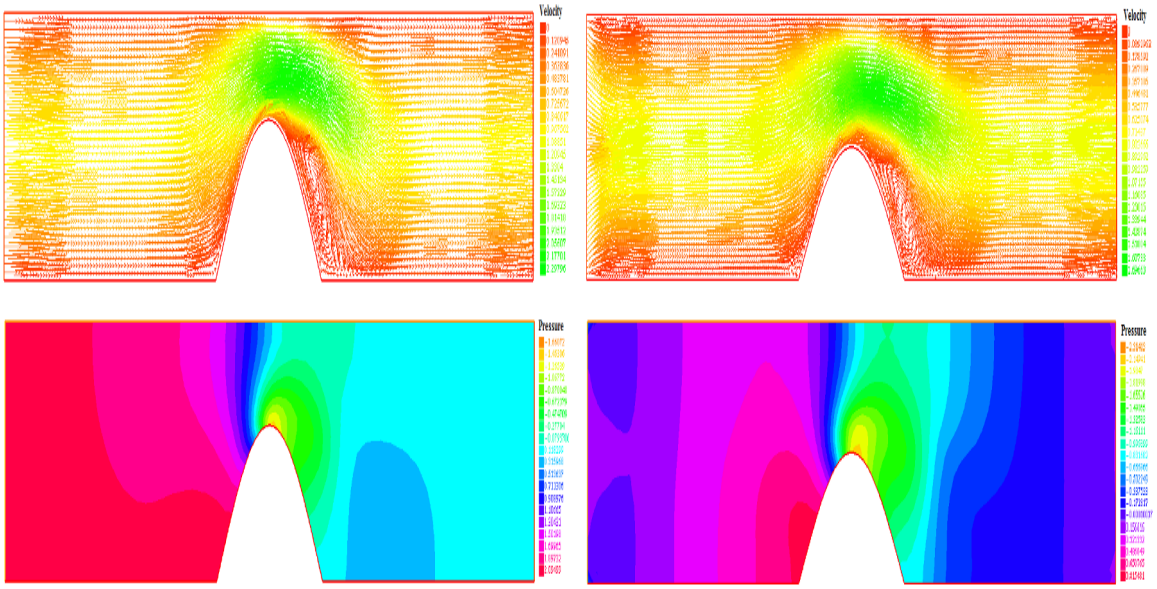

Figure 3.3: Left, velocity and pressure field with Navier Stokes equation at time $t = 0.3s$. Right, velocity and pressure field with the generalized flow model at time $t = 0.3s$

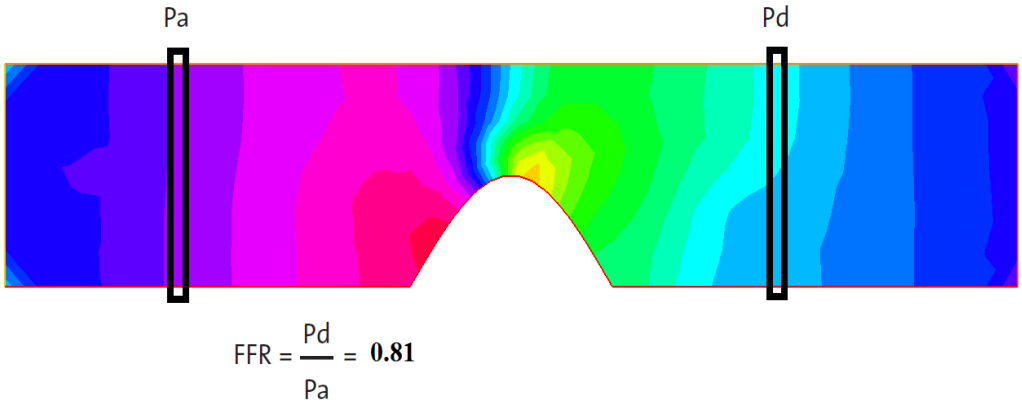

Figure 3.4: FFR calculation. In this case, the degree of stenosis is equal to 40% and the VFFR is equal to 0.81.

In order to take into account the time variations in the value of the VFFR, this value is calculated during 5 consecutive cardiac cycles. We notice that starting from the third cardiac cycle, this value becomes constant. The VFFR takes values in the neighborhood of 0.67 for a lesion with a degree of stenosis equal to 75%.

The following graphic (figure 3.5) gives the variation of the VFFR during the five cardiac

cycles :

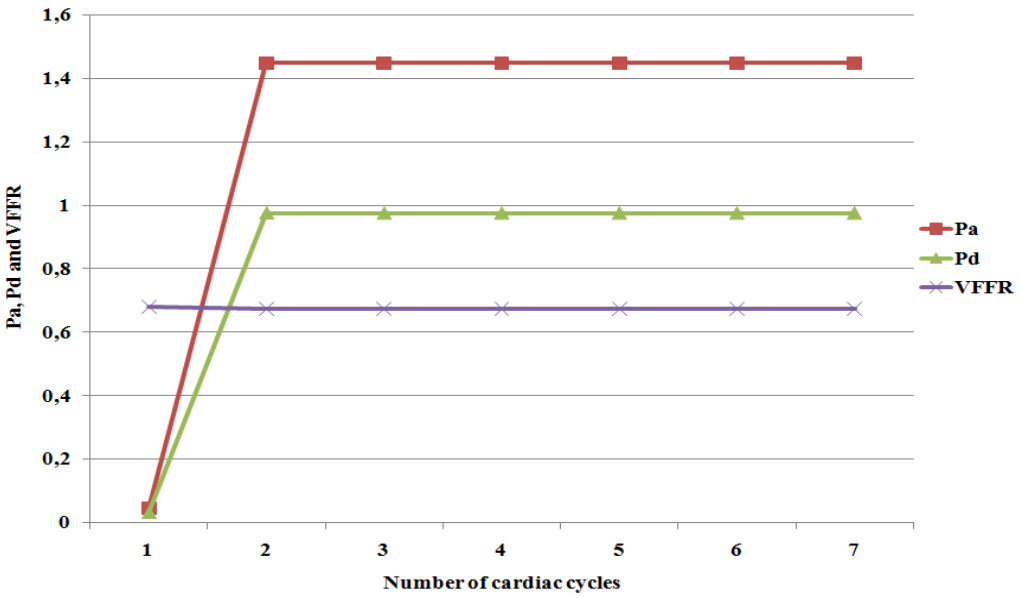

Figure 3.5: VFFR variation during 5 cardiac cycles for a lesion with 75% stenosis.

For all the graphics in the next sections, the VFFR value considered is calculated during the third cycle of the simulation. The two preceding cycles are run in order to reach stable pressure distribution.

The following figures give the aortic pressure P_a, the distal pressure P_d and the VFFR respectively according to the degree of stenosis (figure 3.6 left) and the plaque's radius (figure 3.6 right).

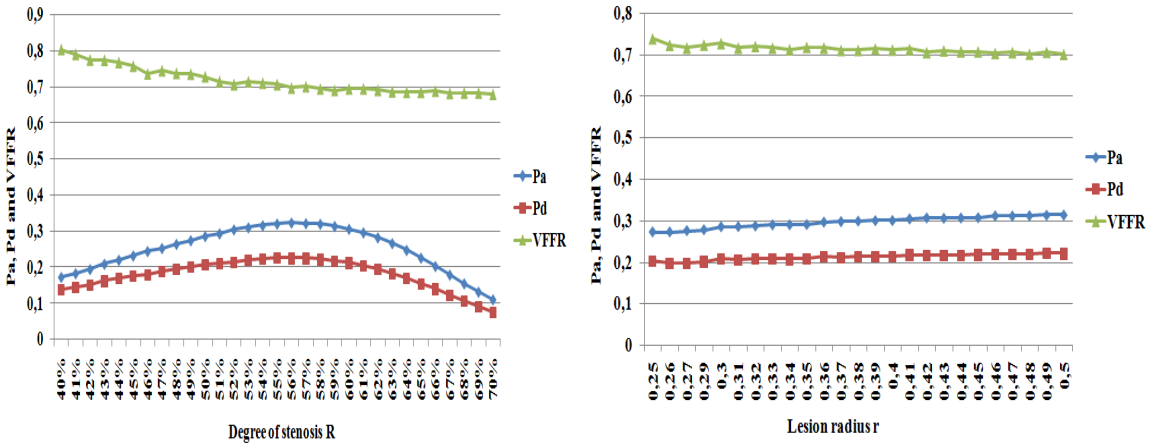

Figure 3.6: Left, P_a, P_d and VFFR variation according to the degree of stenosis R. Right, P_a, P_d and VFFR variation according to the lesion radius δ.

The most common parameter considered to evaluate the significance of a lesion is the degree of stenosis. However, the lesion length (or radius) is also significant for this evaluation, especially when the degree of stenosis is in the intermediate value range [17]. The linear regression models presented in [17] give the correlation between the FFR value (obtained after the invasive test) and different plaque's parameters. Particularly, the lesion radius and the degree of stenosis were considered. The graphics given in paper [17] were obtained from a statistical study of medical data. The results in figure 3.6 cannot be quantitatively compared to those presented in the results in that paper ([17]). However, we can see qualitatively that the graphics have approximately the same trend.

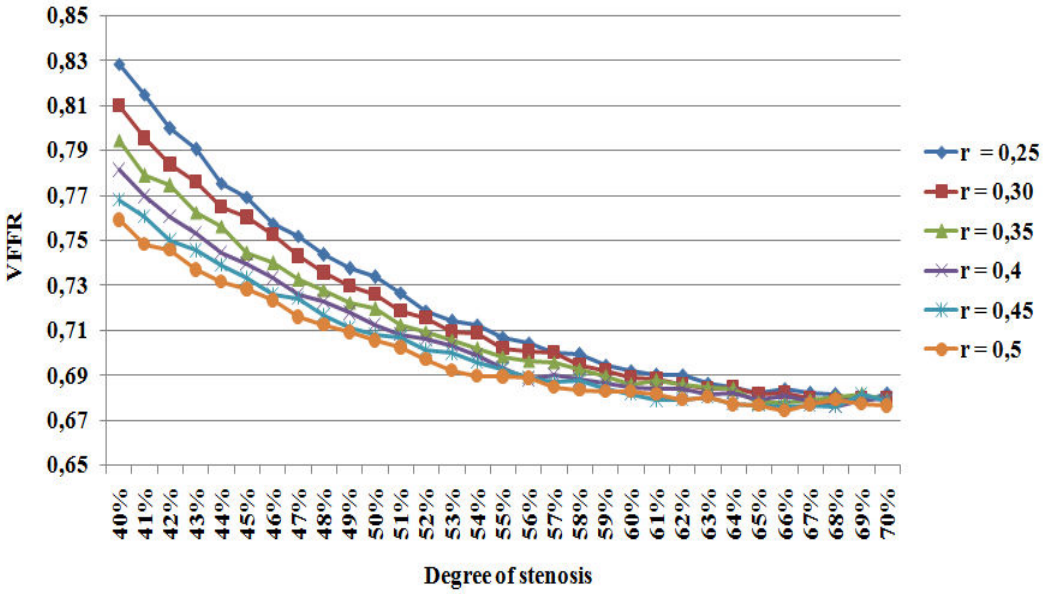

Figure 3.7: VFFR variation for lesions with different radius according to the degree of stenosis.

Figure 3.9 shows the simulated VFFR corresponding to different values of the lesion radius according to the degree of stenosis. We can note from this figure that the curve describing the VFFR according to the degree of stenosis changes with the value of the lesion's radius. Thus, there is an important change in classification, especially for the lesions with a degree of stenosis lower than 45%. For example, for a degree of stenosis of 40%, VFFR value is equal to 0.82 in the case of a lesion's radius of 0.25cm, and to 0.75 on the case of a lesion's radius of 0.5cm. As a consequence, there is a change in the lesion's classification from not hemodynamically significant to hemodynamically significant.

3.4.2 Mutli-stenosis case

In the case of a multi-stenosisl diseased patient, many lesions might be considered in the arterial wall. The following figures describe the blood velocity and pressure in this case:

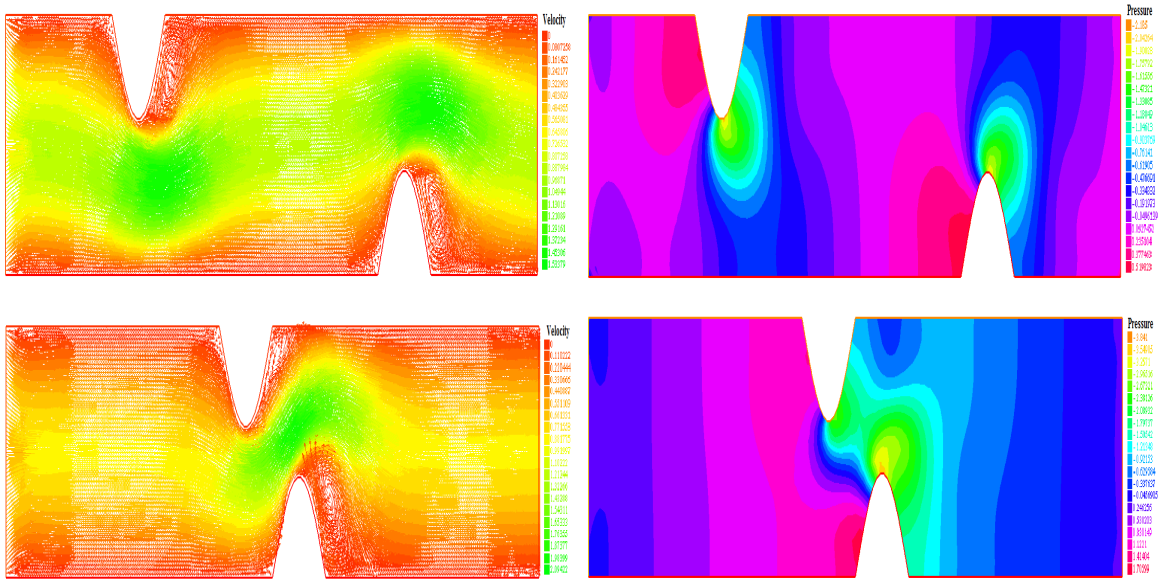

Figure 3.8: Top, velocity and pressure field corresponding to identic lesions of 40% stenosis, with a spacing 'a' of 1.5 cm. Bottom, velocity and pressure field with a spacing 'a' of 0.5 cm

The distance between the two lesions influences the flow, and particularly the micro-circulation downstream the stenosis. Thus, the values of the VFFR obtained in the two cases given in figure 3.10 are different, even if the lesion is somehow similar. The VFFR obtained for a spacing of $0.5cm$ is equal to 0.73, while the VFFR with a spacing of $1.5cm$ is equal to 0.81.

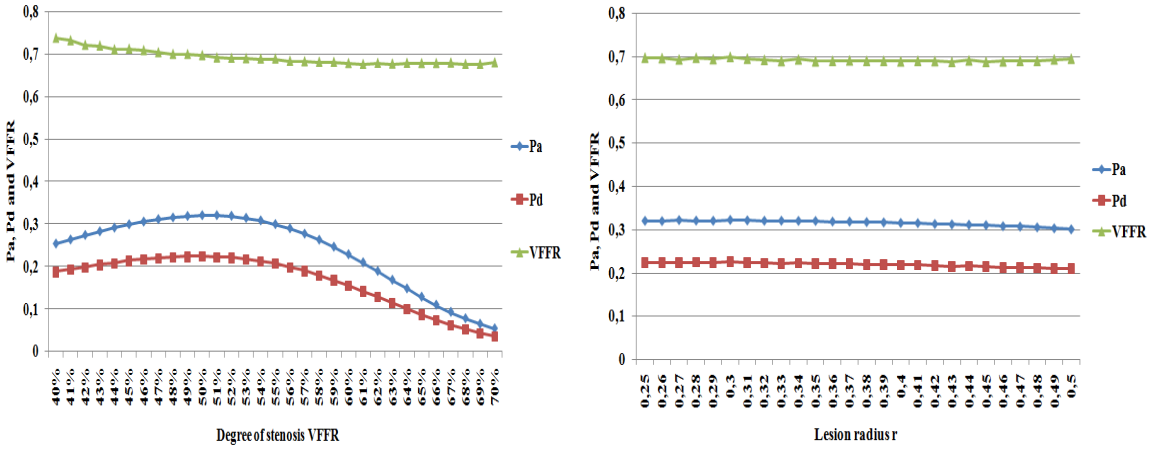

Figure 3.9: Left, P_a, P_d and VFFR variation according to the degree of stenosis R in the case of multiple stenoses. Right, P_a, P_d and VFFR variation according to the lesion radius δ in the case of multiple stenosis.

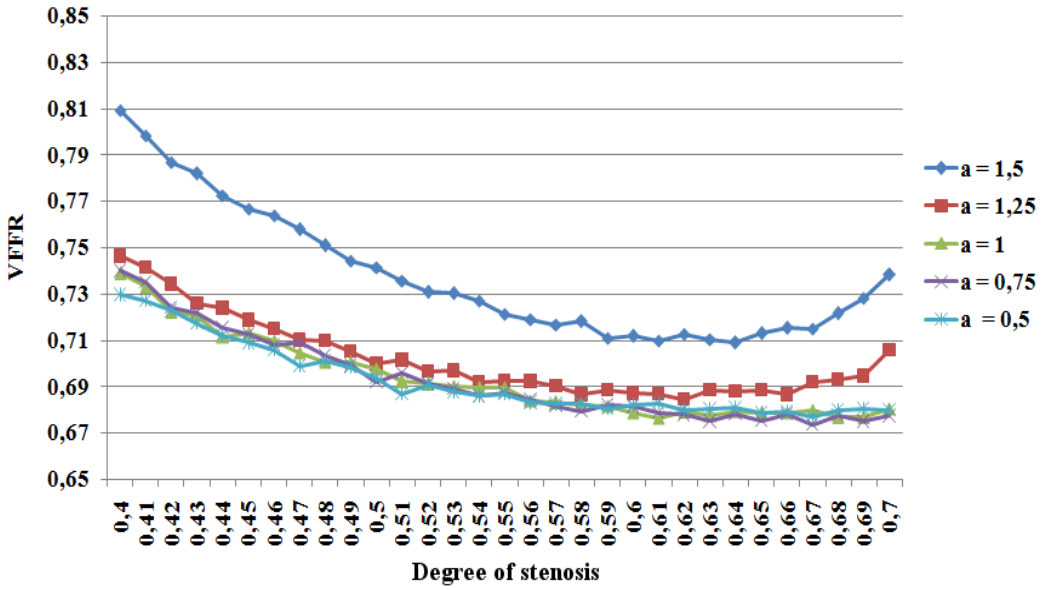

Figure 3.10: VFFR variation in the case of two identic lesions, with different spacings according to the degree of stenosis.

3.5 Coupling scheme: fluid-structure interaction

To achieve more realistic simulations, we consider the fluid-structure interaction between the arterial wall and the blood. We assume that the displacements of the shell are infinitesimal, and that only the upper face of the arterial portion is able to move. In a first place, a generalized linear Koiter model is adopted for the structure, as in [4]. In this case, the arterial wall

is a 1D layer with a thickness ε.

The problem is to find the solid vertical displacement η and the solid vertical velocity $\dot{\eta} = \partial_t \eta$ such that:

$$\begin{cases} \rho_s \varepsilon \partial_t \dot{\eta} - c_1 \partial_x^2 \eta + c_0 \eta = -\sigma(u,p)_{n.n} & over \ \Gamma_{\omega_2} \times (0,T_c), \\ u.n = \dot{\eta}, u.\tau = 0 & over \ \Gamma_{\omega_2} \times (0,T_c), \\ \eta = 0 & over \ \partial\Gamma_{\omega_2} \times (0,T_c). \end{cases}$$

where:

$$\sigma(u,p) = -pI + 2\mu(s(u))Du.$$

u and p are respectively the fluid velocity and pressure, solutions of problem 3.5. $\rho_s = 1.1$ is the solid density. c_1 et c_0 are defined by: $c_1 = \frac{E\varepsilon}{2(1+\nu)}$ and $c_0 = \frac{E\varepsilon}{R^2(1-\nu^2)}$, solid thickness $\varepsilon = 0.1$, Young modulus $E = 0.75.10^6$ and Poisson coefficient $\nu = 0.5$.

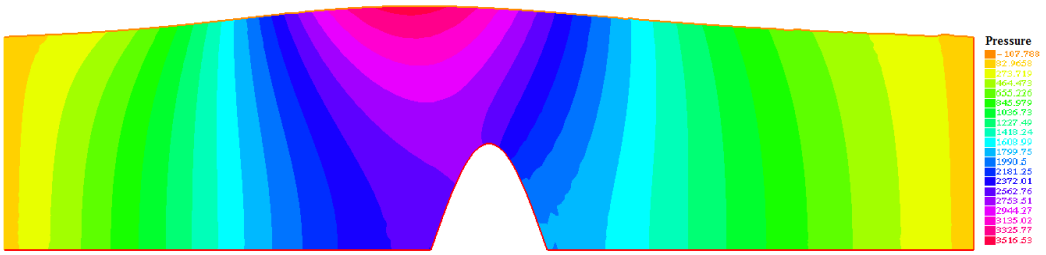

Figure 3.11: Pressure profil with the fluid-structure interaction model.

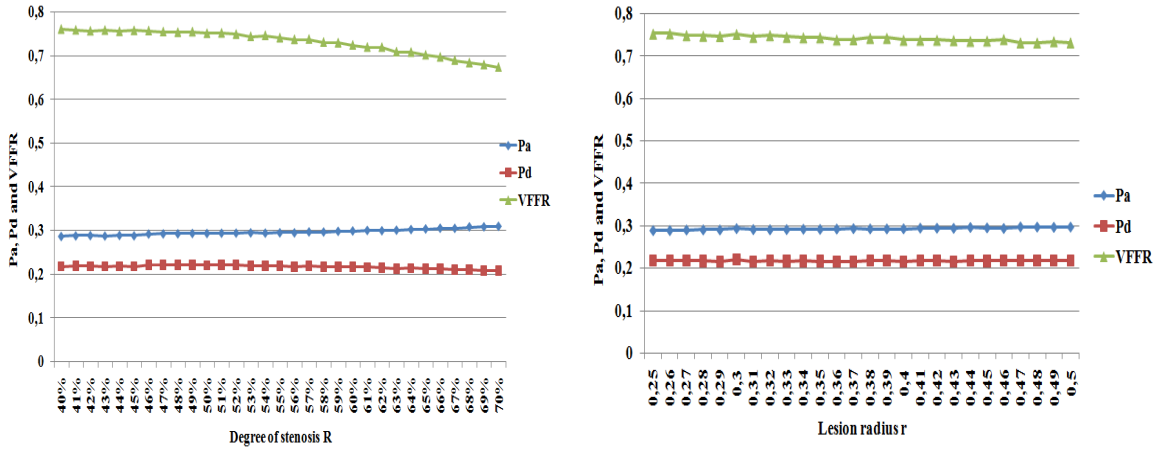

Figure 3.12: Left, P_a, P_d and VFFR variation according to the degree of stenosis R (D defined in equation 3.11 using the fluid-structure interaction model. Right, P_a, P_d and VFFR variation according to the lesion radius δ using the fluid-structure interaction model.

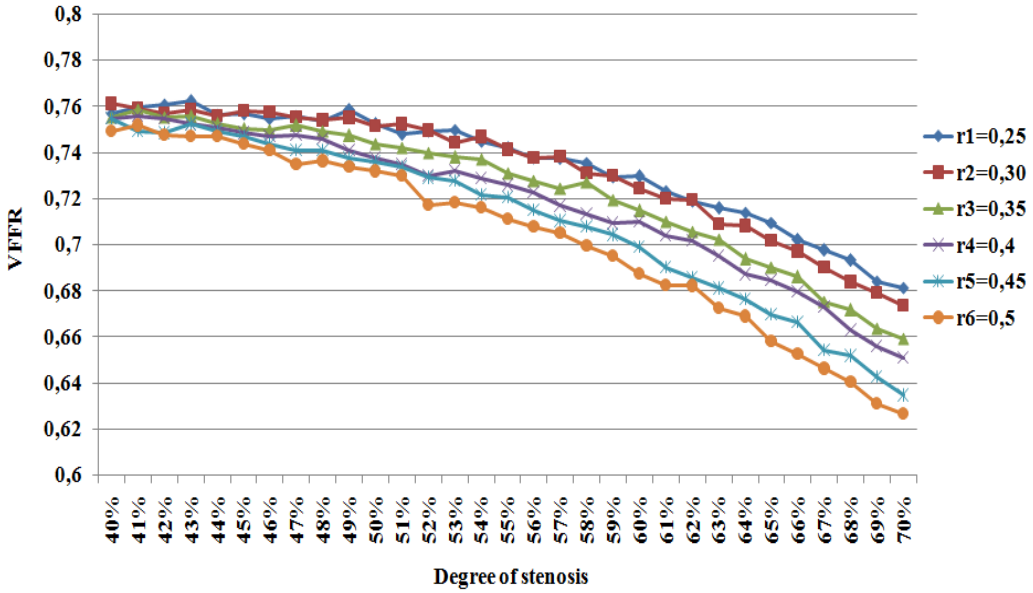

Figure 3.13: VFFR variation using the fluid-structure interaction model according to the degree of stenosis.

The fluid-structure interaction model gives different results compared to the one with rigid boundaries (presented in section 3.4). Therefore, we obtain different values for the VFFR. It should be expected that this model gives better values since it is more adapted to the physiology of the arterial wall. However, to validate the values obtained using this model, we should consider a realistic geometry, reconstructed from clinical images.

3.6 Conclusions

In this chapter, we led different simulations to study the flow through a sclerotic artery. Firstly, we considered a generalized flow model in a fixed 2D domain. We assumed that the initial configuration of the domain corresponds to the maximal vasodilation of the portion of interest. Our purpose was to give a first estimation of the VFFR. We studied the variation of the VFFR with respect to some lesion's parameters: the degree of stenosis and the lesion's radius in the case of a single stenosis. In the case of multi-stenosis (the presence of two parallel lesions), we also studied the VFFR variations according to the distance between the two lesions, since this value also modifies the blood circulation through the diseased portion. Secondly, we introduced a generalized fluid-structure interaction model, in order to take into account the infinitesimal displacements of the upper arterial wall. Large displacements due to the myocardium movements were not considered. Each one of these models: rigid and elastic has a particular importance in the quantification of the VFFR. In medical practice, it

is not the degree of stenosis that modifies the FFR value, even if this parameter is dominant to judge the severity of a lesion. But it is the coronary micro-circulation downstream of the stenosis and its importance that must impact the FFR. This micro-circulation depends not only on the shape of the plaque (flattened, large, sharp...), but on the flow and the wall properties as well. The VFFR model presented in this chapter is able to take into account modifications of the shape of the lesions, through certain parameters on the one hand. On the other hand, is able to take into account/or not the elastic behavior of the upper wall. We highlight that the rigid model, fitted with patient-specific flow parameters, can give useful VFFR estimation in the case of non viable vessels, while the elastic model, in general, is supposed to be more adapted to estimate the VFFR. The values of VFFR obtained by this model are certainly different from those obtained by the rigid one. This could be explained by the fact that the elastic property of the upper wall compensates the over-pressure before the lesion and thus modifies the pressure distribution in the whole domain.

The numerical results for the VFFR presented in this chapter are not yet clinically usable. However, the aim is to enumerate some of the factors influencing the FFR value and to insist on the necessity of going beyond the degree of stenosis in the evaluation of a lesion. In this view, from the comparison between the figures 3.10 and 3.13 we can conclude that the VFFR decreases with the degree of stenosis for both rigid and elastic models. As for the lesion's radius, it influences the VFFR in the rigid model only for lesions with a degree of stenosis lower than 60%. Beyond this value, the VFFR is not subject to a big change using this model. On the contrary, for the elastic model, the lesion's radius influences the VFFR for lesions with degree of stenosis higher than 50%. The geometry of the lesion, dimensioned by the two parameters: R the degree of stenosis and r the lesion's radius, affects the flow through the lesion, and depending on whether the domain is rigid or elastic, the pressure distribution is modified, and the VFFR variation as well.

In the next chapter, we use the same 2D flow model presented in this chapter and an extended version in 3D to simulate blood flow inside realistic geometries issued from medical imaging. The presence of multiple outlets in this case led us to prescribe a new type of boundary conditions based on Windkessel model.

Chapter 4

Blood flow simulation in realistic domains using Windkessel boundary conditions

Abstract

In this chapter, we consider a 2D reconstructed left coronary tree with two artificial lesions of different degrees. We use a generalized fluid model with a Carreau law and a coupled multidomain method to implement Windkessel boundary conditions at the outlets. We introduce our methodology to quantify the FFR, and lead several numerical experiments. We compare FFR results from Navier Stokes versus generalized flow model, and for Windkessel versus traction free outlets boundary conditions or mixed outlets boundary conditions. The computational FFR results show that the degree of stenosis is not enough to quantify a lesion's significance, while there is a good agreement between Navier Stokes and generalized flow model in classifying coronar lesions. We highlight the fact that standard finite elements are not well-adapted as rezolution strategy in realistic geometries, especially when the flow model considered is non linear. We also consider a 3D stenotic bifurcation where we define a 3D flow problem as well as an extension of Windkessel outlet boundary conditions in 3D. The patterns obtained for velocity and pressure are in accordance with the 2D results.

4.1 Introduction

The coronary arteries are a common and important site of the development of sclerotic lesions. Thus, a detailed hemodynamic evaluation of the flow and its spatial and temporal distribution may give important insight to understand the progression of atherosclerosis. In this view, the fractional flow reserve (FFR) plays a central role, see [29]. The fractional flow reserve (FFR) is an invasive measure that consists in introducing a pressure wire to a diseased artery to measure in vivo two values of blood pressure : the aortic pressure P_{aortic}, and the pressure distal to a lesion, P_{distal}. These pressure values are then used to calculate the FFR ratio. According to the value obtained, the clinician decides whether the lesion is hemodynamically significant (FFR lower than 0.80) or non-significant (FFR higher than 0.80). In the case of a significant lesion, a revascularization is necessary. In this case, a realistic simulation of vascular blood flow inside the coronary arteries can be a better alternative to the invasive FFR, see [10] and [32] . On the one hand, a realistic blood flow simulation requires the use of an adequate flow model. For instance, Boujena and al. [10] presented a Non Newtonian flow model adapted to describe blood flow in the presence of atherosclerosis. Simulation in their paper was performed in 2D and 3D simplified geometries. On the other hand, the choice of suitable boundary conditions is crucial. In our paper [29], we presented a first virtual FFR estimation using the generalized fluid model in [10] and led different simulations to study the impact of the lesions parameters on the FFR value. However, we considered a simplified 2D geometry and reduced boundary conditions. In this chapter, the domain of simulation corresponds to a realistic diseased coronary tree with many outlets. Thus, we address a special concern to the boundary conditions model. In fact, the shape and the type of the function at the inlet are determinant of the flow and pressure patterns obtained in the domain. In the case where the study aims at comparing the results to in vivo measurements, the inlet boundary condition should be adequately chosen. Many works explored the effect of the inlet boundary condition, among them Liu and al. [21] and Taylor and al. [20] presented realistic forms of inlet boundary condition in the case of coronary blood flow. Concerning the outlet, the most common boundary condition for blood flow correspond to a constant pressure. However, this choice is not realistic when it comes to complex geometries, with many outlets. The strategy of resolution in this case consists in dividing the domain into two parts : the upstream domain, and the downstream domain that includes the outlets. The outlet boundary conditions are defined in the downstream domain using an appropriate model, usually based on an electrical analogy, known as the Windkessel effect, see [22] and [23]. In the first section, we give the essential elements for simulation : the 2D multi-stenotic domain defined using segmentation techniques, the realistic flow model and finally suitable boundary conditions. In the second section, we present the pressure and the flow distributions obtained for three different outlet boundary conditions. Finally, in the

last section, we give an estimation of the fractional flow reserve (FFR) for two lesions using the pressure pattern in the stenotic coronary tree. The FFR calculation is performed using two different flow models: Navier Stokes and the generalized flow model, and considering diverse outlet boundary conditions.

4.2 Mathematical modelling

4.2.1 Domain definition: 2D image segmentation

In order to create a realistic geometry for numerical simulation, we started from a 2D patient-specific angiography. An enhancement technique was done before this image could be segmented. In this phase, different filters were used to improve the contrast of the original image, see [31]. Then opening/closing Matlab functions were used to extract a black and white image that contains only the coronary tree in which we are interested. It should be noticed that despite the fact that the original angiography corresponds to a stenotic coronary tree, due to the lower quality of the image, and to the small degree of stenosis of the lesion, this last could not appear in the black and white image. Since our aim in this chapter is to investigate the impact of the flow model and the boundary conditions on the FFR, we introduced two different artificial lesions in the coronary tree. The first lesion corresponds to 68% stenosis and was drawn in the same location of the real patient's lesion. The second lesion corresponds to 56% stenosis and was drawn at the entrance of the longest branch in the coronary tree. This choice is justified by the purpose of calculating the fractional flow reserve in the case of free outlet boundary conditions. The resulting 2D multi-stenotic domain, the original extracted tree, and the original angiography are given in figure 4.1.

Starting from the new multi-stenotic coronary tree, the segmentation and the meshing were performed later using a homemade Freefem++ code, see [24].

4.2.2 Coronary blood flow model

The blood was assumed as an incompressible, non-Newtonian viscous fluid obeying the Carreau law with the viscosity shear rate relation given by :

$$\mu = \mu_\infty + (\mu_0 - \mu_\infty)(1 + (\lambda s(u))^2)^{(n-1)/2} \tag{4.1}$$

where $\mu_0 = 0.0456$ $Pa.s$ and $\mu_\infty = 0.0032$ $Pa.s$ are the values of the viscosity for the lowest and highest shear rates. The parameter values $\lambda = 10.03s$ and $n = 0.344$ are typical for the Carreau law. The shear rate $s(u)$ is defined as follows:

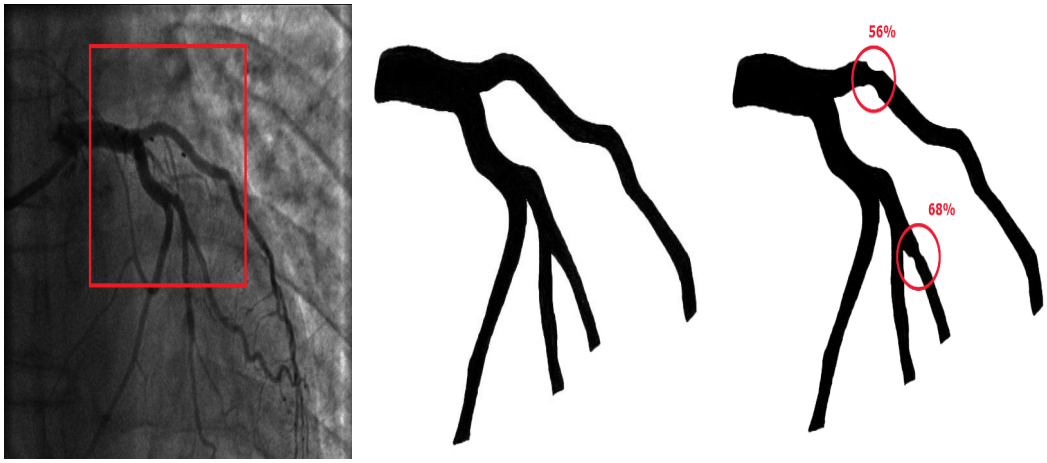

Figure 4.1: From left to right: The original angiography image, the coronary tree of interest is framed with red. The Black and white original image. The resulting multi-stenotic coronary tree.

$$(s(u))^2 = 2Du : Du = 2\sum_{i,j}(Du)_{ij}(Du)_{ji} \tag{4.2}$$

with :

$$Du = \frac{1}{2}(\nabla u + \nabla^T u) \tag{4.3}$$

The geometrical 2D domain Ω_f is given in figure 4.2. The time dependent two dimensional generalized fluid equations presented in [1] were considered as the governing equations in the tree domain Ω_f :

$$\begin{cases} \rho_f \dfrac{\partial u}{\partial t} + \rho_f (u.\nabla)u - \nabla.(2\mu(s(u))Du) + \nabla p = f, \ \ in \ \ \Omega_f \times (0,T_c) \\ \nabla.u = 0, \ \ in \ \ \Omega_f \times (0,T_c) \\ 2\mu(s(u))Du.n - pn = I, \ \ on \ \ \Gamma_{in} \times (0,T_c) \\ u = 0, \ \ on \ \ \Gamma_l \times (0,T_c) \end{cases} \tag{4.4}$$

where u is the incompressible velocity and p is the pressure. f is the external body force applied to the fluid. I is the velovity profile at the inlet, that will be given in the next paragraph. In the computations, the blood density ρ_f was assumed to be constant at 1060 $Kg.m^{-3}$. A no-slip condition was applied to the velocities at the lumen wall, considered to be inelastic and impermeable. A steady Stokes initial condition, with a Poiseuille function at the inlet was imposed. T_c corresponds to the duration of a cardiac cycle under normal conditions, we took $T_c = 0.8s$ (corresponding to a heart rate of 75 beats per minute).

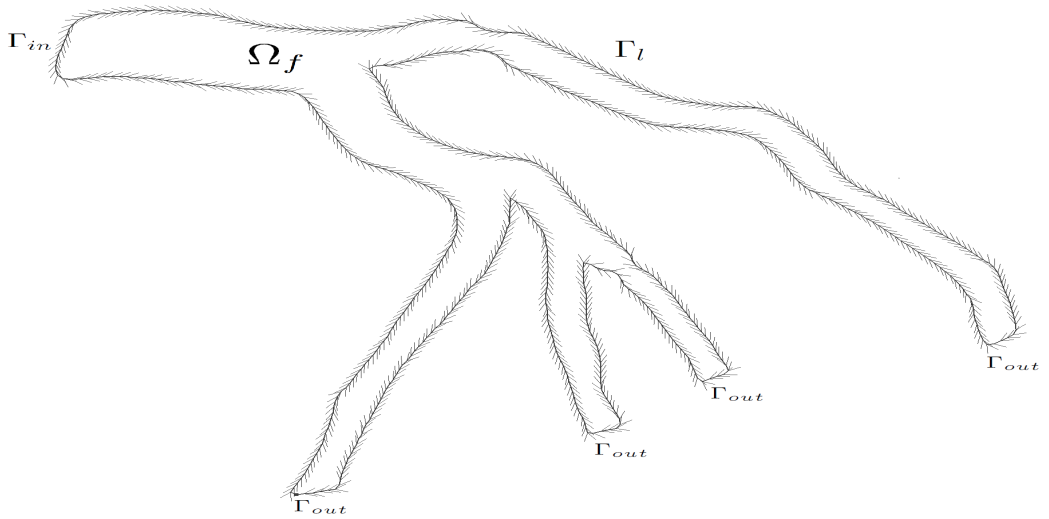

Figure 4.2: The 2D geometry considered. Arrows indicate the isoline orientation.

4.2.3 Boundary conditions : Inlet / Outlets

Since the processed image treated corresponds to a left coronary artery, we used sinusoïdal functions to approach the inlet flow distribution into the left coronary artery. The shape of this function is well known, see [21]. Considering that T_{sys} is the period of systole, t_s the start of the systolic phase of the current cardiac cycle and t_d the start of the diastolic phase, this periodic function $I(t)$ can be written as follows:

$$I(t) = \begin{cases} (I_p + I_0 * sin(\pi * (t - ts)/Tsys), 0), & 0 \leq t \leq T_{sys} \\ (I_p + I_c * sin(\pi * (t - td)/(T_c - Tsys)), 0), & T_{sys} \leq t \leq T_c. \end{cases} \tag{4.5}$$

where $I_p = 10\ \ cm/s$ represents the dominant flow, $I_0 = 10\ \ cm/s$ and $I_c = 10\ \ cm/s$. T_{sys} is taken equal to 0.33s. The remaining duration from the cardiac cycle corresponds to a diastole. The profile of this function is given in figure 4.3.

To assess the influence of outlet boundary conditions on the pressure and flow fields, two different outlet boundary conditions were utilized in this study: traction free and a 2 elements Windkessel model [23] to incorporate the resistant effect of the downstream bed. Indeed, the coupled multidomain method was utilized, as described in [23]. The idea is to couple the solution at the outflow boundaries of the computational domain of simulation with the 2 element Windkessel model (chosen in our case) to represent the downstream coronary vascular network cut from the real domain. It should be noticed that other so

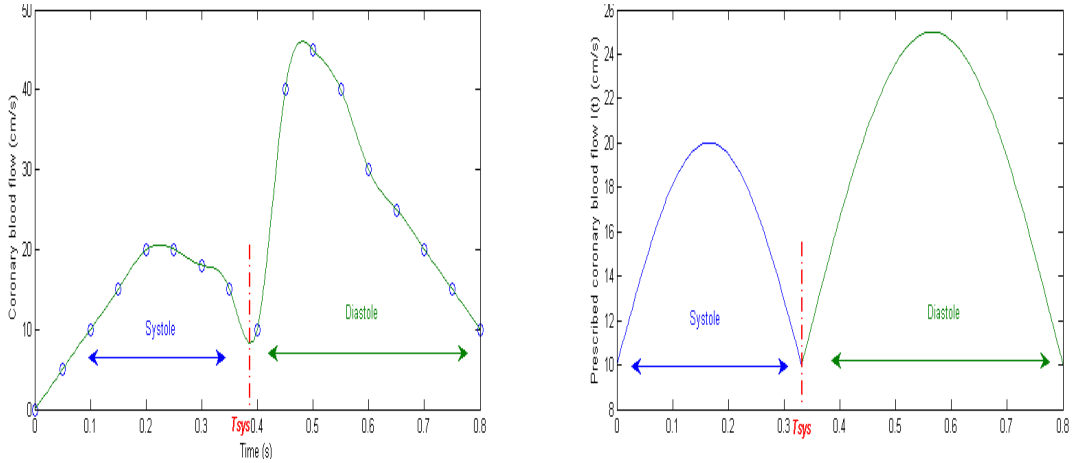

Figure 4.3: Left, spline function approaching left coronary blood flow. Right, the flow function prescribed at the inlet $I(t)$.

called lumped parameter models can be used for the downstream bed like 1D or 2D based impedance boundary conditions..etc, see [23] or [33] for further details.

To represent this type of outflow boundary conditions, we need to introduce the two operators: $M = [M_m, \overrightarrow{M_c}]$ and $H = [H_m, \overrightarrow{H_c}]$. M represents the traction while H represents the flow at each coronary outlet. Each one of M and H is composed of a momentum and a continuity operator respectively.

For each coronary outlet we define the operators M and H by replacing the coronary outlet pressure P(t) with the ordinary differential equation obtained from the 2 element Windkessel model. In our case, the same model is used to represent all the outlets. A weak formulation of the problem in this case can be written as follows, based on the proof introduced in [23]:

$$\begin{cases} \rho_f \int_{\Omega_f} \dfrac{\partial u}{\partial t} v dx + (Au, v) + \rho_f b(u, u, v) - \boxed{\displaystyle\int_{\Gamma_{out}} v.(M_m(u,p) + H_m(u,p)).\overrightarrow{n}\, ds} \\ \quad + \boxed{\displaystyle\int_{\Gamma_{out}} q.(\overrightarrow{M_c}(u,p) + \overrightarrow{H_c}(u,p)).\overrightarrow{n}\, ds} = \displaystyle\int_{\Gamma_{in}} Id\sigma, \quad \forall v \in V, \forall p \in P \\ u(0) = u_0, \quad in \ \ \Omega_f \end{cases} \tag{4.6}$$

where V and P are the Hilbert spaces introduced in [23], defined by:

$$V = \{v \in (H^1(\Omega_f))^2 | \nabla.v = 0 \ \ in \ \ \Omega_f, v = 0 \ \ on \ \ \Gamma_l\}$$

$$P = \{p \in (H^1(\Omega_f)\}$$

with :

$$(Au, v) = \int_{\Omega_f} 2\mu(s(u))Du : Dvdx, \tag{4.7}$$

$$b(u, v, w) = \sum_{i,j=1}^{2} \int_{\Omega_f} u_i \frac{\partial v_j}{\partial x_i} w_j dx \tag{4.8}$$

The expressions of the boxed terms representing the downstream bed physics will be given in the next section.

4.2.4 Windkessel model

Lumped parameter models was originally derived by the physiologist Otto Frank in an article published in 1899 [25] to describe the afterload of the heart related to pumping blood through the arterial system, as described in [23]. Windkessel model is based on an electrical analogy where an arterial tree is assimilated to an electric circuit. The parameters of the components of the circuit (resistances, capacitances, etc) correspond to the properties of each branch. The variables are the voltage at every node and the current in each branch. In the context of blood flowing in an arterial network, pressure plays the role of voltage and flow rate the role of current. During a cardiac cycle, a 2 elements Windkessel model takes into account the effect of arterial compliance and total peripheral resistance. In the electrical analogy, the arterial compliance (C in $cm^3/mmHg$) is represented as a capacitor with electric charge storage properties. Peripheral resistance of the systemic arterial system (R in mmHg s/cm^3) is represented as an energy dissipating resistor. The flow of blood in the heart (Q(t) in cm^3/s) is analogous to that of current flowing in the circuit and the outlet blood pressure ($P(t)$ in mmHg) is modeled as a time-varying electric potential. We also consider the downstream intramyocardial pressure P_d: the pressure in the left atrium. Figure 3.1 gives a schematic view of the representative circuit of the dynamics in each compartment of the coronary tree. The resulting differential equation can be written as follows:

$$Q(t) = \frac{P(t) - P_d(t)}{R} + C\frac{d(P - P_d)(t)}{dt} \tag{4.9}$$

Using the operators M and H, we couple the flow and pressure at each coronary outlet between the upstream finite element model and the downstream Windkessel model. Like demonstrated in [23], their expressions are obtained by resolving the differential equation given above (equation 4.9).

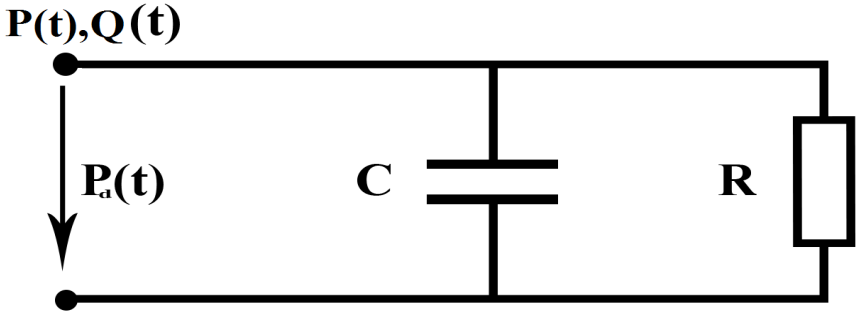

Figure 4.4: Windkessel electrical analogy.

$$\int_{\Gamma_{out}} v.M_m(u,p).\overrightarrow{n}\,ds$$
$$= -\int_{\Gamma_{out}} v.\overrightarrow{n}\ \ (R\int_{\Gamma_{out}} u.\overrightarrow{n}\,ds + \int_0^t \frac{e^{-(t-t_1)}/\delta}{C}\int_{\Gamma_{out}} u(t_1).nds.dt_1 + \overrightarrow{n}.\tau.\overrightarrow{n})\ \ ds$$
$$+\int_{\Gamma_{out}} v.\tau.\overrightarrow{n}\,ds \tag{4.10}$$

$$\int_{\Gamma_{out}} v.H_m(u,p).\overrightarrow{n}\,ds$$
$$= -\int_{\Gamma_{out}} v.\overrightarrow{n}\ \ ((P(0) - R\int_{\Gamma_{out}} u(0).\overrightarrow{n}\,d\Gamma - P_d(0))e^{-t/\delta} + P_d(t))\ \ ds \tag{4.11}$$

$$\overrightarrow{M_c}(u,p) = u \qquad and \qquad \overrightarrow{H_c}(u,p) = \overrightarrow{0} \tag{4.12}$$

where $\delta = RC$, $R = 0.95$ and $C = 1.06$.

We consider the same values of Windkessel parameters for all outlets. The downstream pressure P_d is also varying in time. The expression of P_d can be found by solving analytically the differential equation 4.9 considering a simplified expression for $Q(t)$, based on common learning of the cardiac physiology. During diastole, when the ventricules are relaxed, there is no blood flow in the aorta. However, with ventricular contraction during systole, blood is ejected into the aorta and can be modeled as a sinusoïdal wave. In this work, we use the same approach in [22] to implement $P_d(t)$ in the case of a 2 element Windkessel model. The velocity and pressure fields inside the realistic computational domain were solved semi-implicitly. Mainly due to the viscosity term with Carreau law involving shear rate $s(u)$. The

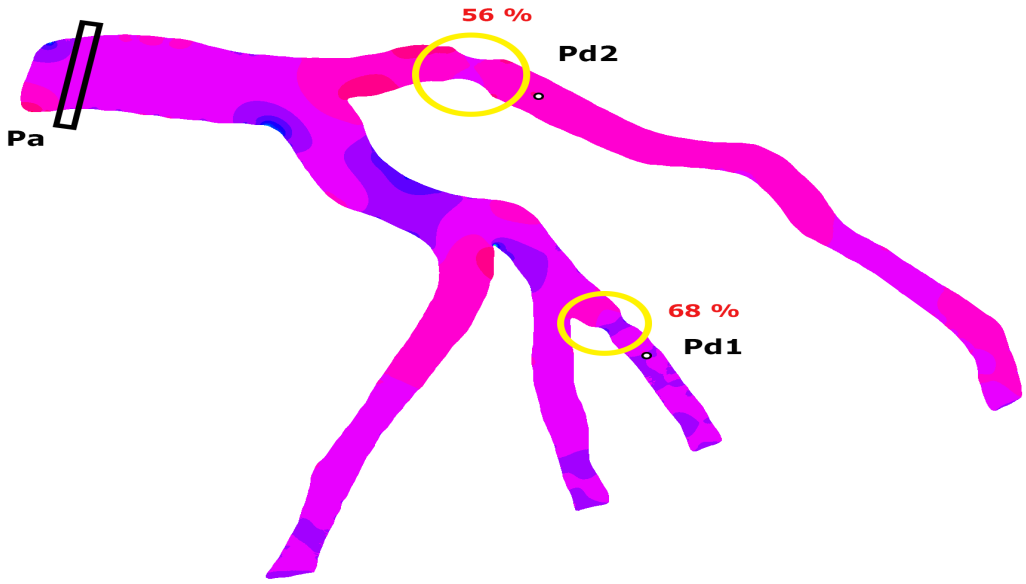

Figure 4.5: FFR calculation. The mutli-stenotic coronary tree contains two lesions: 56% stenosis and 68% stenosis.

finite element method for the resolution was implemented under FreeFem++. The numerical results obtained are presented in the next sections.

4.2.5 Fractional flow reserve (FFR)

Our objective is to give an estimation of the FFR for both lesions in the diseased coronary tree using the pressure distributions obtained in the tree domain. We aim at the study of the effect of the flow model and the outlet boundary conditions on the FFR value. For this reason, we consider two different flow models: Navier Stokes versus the generalized flow model (presented in the previous section), and three options for outlets boundary conditions: Windkessel, free outlets and mixed boundary conditions given in detail in the next section. We assume that the 2D geometry for FFR measurements corresponds to a maximal vasodilation. In fact, a clinically certified FFR value (compared to real FFR measurements) is not our ultimate goal in this stage of the work. We implement an algorithm to comput a virtual FFR following the same calculation strategy as used by the clinical FFR device, like in [29]. At each time step, the aortic pressure P_a is calculated by the mean pressure of the points at 1 cm from the inlet of the coronary tree, in order to avoid all the transient effects at the entrance.

The distal pressure P_d is obtained at a distance of 1 cm beyond each lesion on the sensor contour assimilated to a disk with constant diameter. The ratio between the sensor diameter

and the reference diameter of the branch is: $\frac{D_{sensor}}{D_{ref}} = \frac{1}{10}$, based on the common magnitude of the sensor diameter that is $0.014'' = 0.35\ mm$. It should be noticed that the 2D disk is not virtual and is considered as an obstacle to the flow, in contrast to the virtual box for P_a calculation. The diagram in figure 4.5 describes the approach. At each cardiac cycle - and during five consecutive cardiac cycles - a temporal mean pressure of P_a and P_d is performed. The ratio of these two pressures gives an FFR value at each cardiac cycle.

4.3 Numerical results

Simulations are performed using the finite element solver Freefem++, based on a semi-implicit time discretization scheme. Fluid velocity and pressure are calculated at each time step. The time step used is $\delta t = 5.10^{-3}\ s$ and the duration of a cardiac cycle is $T_c = 0.8\ s$. Five consecutive cardiac cycles were simulated to reach a periodic regime of the flow. As for the spatial discretization, we use a 55353 elements mesh. To study the dependency of the solution on the numerical mesh, we perform a mesh refinement convergence study for FFR estimation. The results from this convergence study are presented in table 4.2 in section **??**. This is mainly due to the curved aspect of the 2D domain and to the fact that the common finite element method is not well-adapted in our case, see [28]. Moreover, it is recognized that the numerical resolution of the Non Newtonian Navier Stokes equation is sensitive to the mesh size and to mesh modification. The results in figure 4.6 give the flow (magnitude of velocity) and pressure patterns into the stenotic coronary tree at the peak diastole of the fifth cardiac cycle. The same flow model - Non Newtonian Navier Stokes - is used for all simulations. However, three different outlet boundary conditions were considered: firstly, we considered that all outlets corresponds to a 2 elements Windkessel model. Secondly, we used a free traction boundary condition for all the outlets. Finally, we introduced mixed outlet boundary conditions where the longest stenotic branch of the tree is considered as a traction free outlet, and the remaining three branches correspond to a 2 elements Windkessel models with the same parameters.

Results in figure 4.6 show that the velocity and pressure fields have approximately the same layout with Windkessel and free outlets boundary conditions even if the isovalues are different. This is due to the fact that in both these cases no one of the outlets is advantageous comparing to the others (resistive effect or free exit in all of them). In contrary, with mixed boundary conditions, the longuest branch is free while the rest corresponds to a 2 element Windkessel model. As a result, we observe lower values of pressure in this branch and eventually higher values of velocity which is completely intuitive.

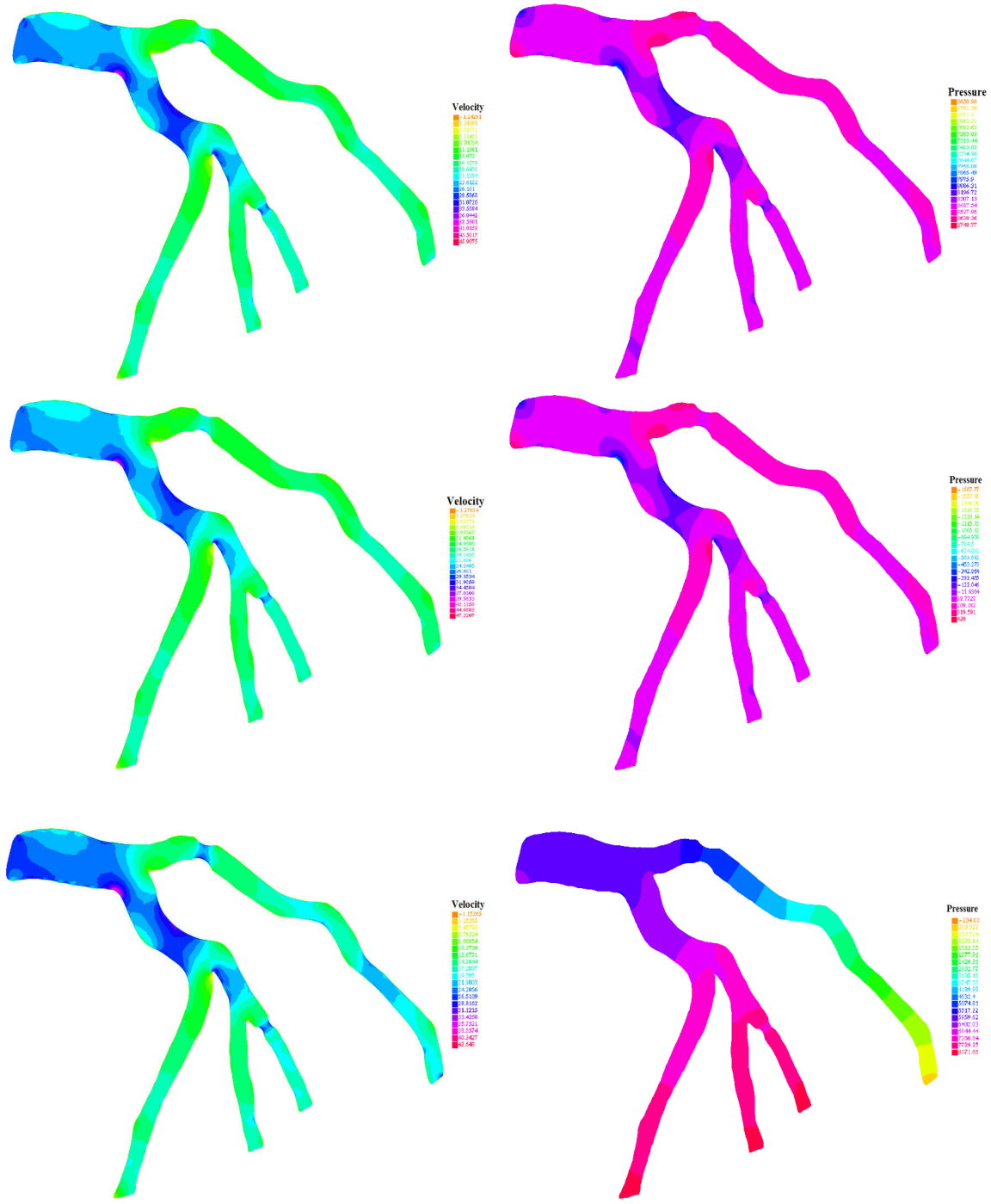

Figure 4.6: From top to bottom: Velocity and pressure fields at $t = 0.59s$ (peak diastole) using Windkessel model, free pressure outlet boundary conditions and mixed outlet boundary conditions (as defined in the paragraph above) respectively.

4.3.1 Fractional Flow Reserve (FFR) computation

The lesions of interest have a degree of stenosis equal to 56% and 68%, which makes them both in the intermediate value range. That justifies the necessity of the fractional flow reserve in taking a clinical decision. Table 4.1 gives the FFR values for these two lesions using Navier Stokes and the generalized flow model and considering three different options for the outlet boundary conditions: Windkessel model, traction free outlets and mixed outlet boundary conditions where only the longest branch is considered free while the other branches outlets are assimilated to a 2 elements Windkessel model. The FFR result in table 4.1 corresponds to the average FFR value over five cardiac cycles in each different case of study.

Mesh size	Coarse mesh					
Flow model	Navier Stokes			Generalized flow		
Outflow BC	Wind-kessel	Free Out-lets	Mixed BC	Wind-kessel	Free Out-lets	Mixed BC
FFR 1	0.917	0.710	0.717	0.908	0.698	0.722
FFR 2	0.760	0.119	0.885	0.7478	0.106	0.8567
Mesh size	Fine mesh					
Flow model	Navier Stokes			Generalized flow		
Outflow BC	Wind-kessel	Free Out-lets	Mixed BC	Wind-kessel	Free Out-lets	Mixed BC
FFR 1	0.9515	0.8704	0.7172	0.9404	0.8096	0.7229
FFR 2	0.8205	0.2459	0.9891	0.8039	0.2082	0.9791

Table 4.1: FFR values for both lesions correponding to the two flow models and the different outlet boundary conditions. The two mesh files presented in figure 3.5 were used for these calculations.

The model used for simulation is non linear, as shown in equation 4.4. Moreover, the domain of simulation is not a plane geometry but a curved boundary configuration, and the finite element method used is standard (triangular elements are not well adapted to curved domain in the opposite of isoparametric elements for example, see [53]). As a result, the solution of our system is dependent on the numerical mesh and the FFR estimation algorithm is sensitive to the mesh discretization (as show in table 4.1). In this case, the accuracy of the FFR estimation might be questioned. In order to study the sensitivity of the FFR value computed, a mesh refinement convergence study is presented in the next paraghraph. Then, a discussion of the results in table 4.1 is provided in paragraph 4.3.2, based on the finer mesh simulations.

Convergence study

In this paragraph, we present a mesh refinement study for FFR computation. We consider 10 different meshes, with a number of elements varying from 1478 to 51528. We use P2 element for velocity components and P1 element for the pressure. For each finite element space considered, the simulation was run during five consecutive cardiac cycles, we compute the FFR value and the average FFR value FFR_a over the previous cycles. We only considered one lesion, that is lesion 1 represented in figure 3.4. The time step $dt = 5 \times 10^{-3}$ considered for all simulations was small enough so that the numerical stability of the semi-implicit scheme is verified. For all simulatons, we use the non Newtonian model for flow and the 2 element Windkessel boundary condition for all outlets. The main results from this study are presented in table 4.2.

N vertices	Cycle N	1	2	3	4	5
1478	FFR	0.9803	0.93115	0.8538	0.9179	0.9203
	FFR_a	0.9803	0.9557	0.9217	**0.9208**	**0.9207**
1746	FFR	0.9792	0.9382	0.9128	0.9278	0.9505
	FFR_a	0.9792	0.9587	0.9434	**0.9420**	**0.9417**
2143	FFR	0.9824	0.9228	0.8644	0.9308	0.9111
	FFR_a	0.9824	0.9526	0.9232	**0.9251**	**0.9223**
2786	FFR	0.9795	0.9214	0.8777	0.9138	0.9221
	FFR_a	0.9795	0.9504	0.9262	**0.9231**	**0.9229**
3731	FFR	0.9819	0.9203	0.8180	0.9210	0.9143
	FFR_a	0.9819	0.9511	0.9067	**0.9103**	**0.9111**
5254	FFR	0.9759	0.9194	0.8037	0.9014	0.9101
	FFR_a	0.9759	0.9476	0.8996	**0.9001**	**0.9021**
7908	FFR	0.9790	0.9267	0.8305	0.9082	0.9106
	FFR_a	0.9790	0.9528	0.9120	**0.9111**	**0.9110**
13916	FFR	0.9724	0.9231	0.8251	0.9222	0.9172
	FFR_a	0.9724	0.9477	0.9068	**0.9107**	**0.9120**
30658	FFR	0.9619	0.9243	0.8278	0.9064	0.9036
	FFR_a	0.9619	0.9431	0.9046	**0.9051**	**0.9048**
51528	FFR	0.9608	0.9220	0.8271	0.8993	0.9013
	FFR_a	0.9608	0.9414	0.9033	**0.9023**	**0.9021**

Table 4.2: FFR values for the second lesion at 5 different cardiac cycles, for different values of the meshsize. The same value of time step was adopted for all simulations $dt = 5 \times 10^{-3}$. FFR is the value for the cardiac cycle while FFR_a is the average FFR value.

We can observe from the results in table 4.2 that from the third cycle the FFR average FFR_a is not subject to a big change (two decimal places constant) for all the space discretizations considered. We can see that for the two final meshes, the FFR_a value is not subject to a big change. The value of 0.90 can be adopted to make a clinical decision. This lack in the

accuracy of the estimation can only affect the lesions for which the FFR value obtained is close to the clinical FFR cut-off. In general, for these special cases, the pratician resorts to the patient clinical history and to some additional tests to decide for the strategy of treatment, see [16].

4.3.2 Discussion

The flow model considered for simulations is only slightly influencing the FFR value. For example, considering the possible options for outlets boundary conditions, the difference in the FFR between the Navier Stokes model and the non-Newtonian flow model does not exceed 2% where the outlets are not all free. In the case of free outlets, the decrease in the FFR value for the first lesion is quite surprising (cells in gray in the table): up to 79% and 75% with the generalized fluid and the Navier Stokes models respectively. In fact, there is a huge pressure drop in the $P(t)$ value since the distal sensor for this lesion is not far enough from the free exit. In the contrary, we do not have this problem with the second lesion as the branch is long enough beyond the sensor. That shows that this type of boundary conditions are not appropriate and not realistic to perform a such calculation in the coronary arteries, though their widespread use, see [30]. Now, comparing between Windkessel and mixed boundary conditions, we can see that the first lesion conserves the same FFR classification - hemodynamically non-significant - while the second lesion moves from the non- significant stenosis class to the significant one. These same classifications are conserverd with both flow models. Considering the fact that the first lesion has an important degree of stenosis (68%) while the second one is a 56% lesion, this result confirms that the FFR value is not only depending on the degree of stenosis, which renders a physical severity of the lesion, but also on the haemodynamical flow inside the connected tree, strongly impacted by the flow model and the nature of boundary conditions (inlets and especially outlets boundary conditions).

4.4 3D modelling

In this section, we aim to run simulations inside a realistic 3D domain. We use the 3D flow model given in the previous chapter 4.13 as well as a 3D extension of outlet boundary conditions introduced in section 4.2.4. The two 3D domains has been acquired thanks to our collaboration with a qualified team in the field of cardiovascular domain reconstruction from medical imaging CARMEN team project at INRIA Bordeaux Sud Ouest. No special concern was accorded to that part but we got two surface meshes from them ready for simulation purposes. The meshes of interest are practically the same, one is a diseased version of the other: an artificial lesion is created in order to visualize the impact on the flow and to compute the corresponding FFR value. The following figure 4.9 gives the 3D mesh of the healthy tree:

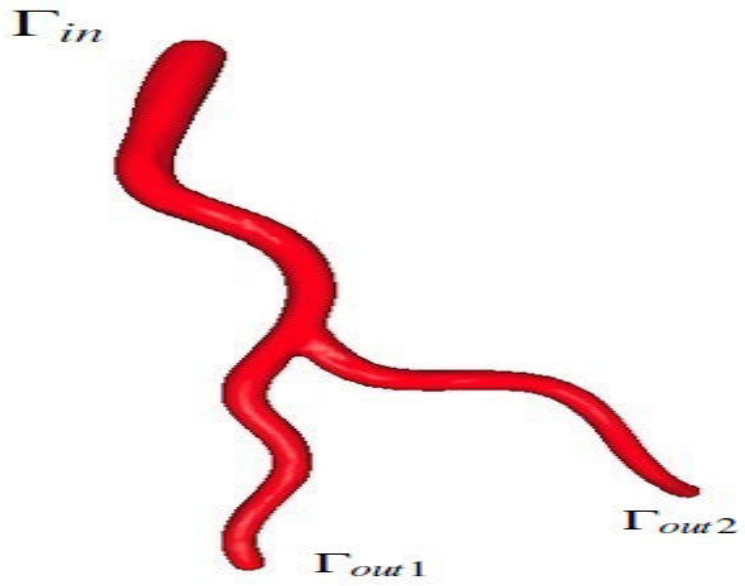

Figure 4.7: 3D domain used for simulations.

4.4.1 Details about the flow model and boundary conditions

The flow model used for all simulations has been introduced for the first time in [2], with a detailed proof of existence of a weak solution in the case of non Newtonian flow.

The PDE equation can be written as follows:

$$\begin{cases} \rho_f \dfrac{\partial u}{\partial t} + \rho_f(\dfrac{1}{2}\nabla|u|^2 + curl\ \ u \times u) - \nabla.(2\mu(s(u))Du) + \nabla p = 0, \ \ in\ \ \Omega_f \times (0,T_c) \\ \nabla.u = 0, \ \ in\ \ \Omega_f \times (0,T_c) \end{cases} \tag{4.13}$$

Using the following identity, as in [2] :

$$u \cdot \nabla u = \frac{1}{2}\nabla|u|^2 + curl\ \ u \times u \tag{4.14}$$

The expression of $s(u)$ is the same as in the 2D case, see 4.2 and 4.3, as well as the expression of the viscosity given by Carreau law, introduced in the second chapter 3, with the same values of parameters.

As for the boundary conditions, the inlet boundary conditions is a 3D function- similar to that given in equation 4.5 since we consider that the 3D tree is issued from a left coronary tree, see [17] - given by:

$$\sigma^{tot}(u,p).n = I(t), \ \ in\ \ \Gamma_{in} \times (0,T_c), \tag{4.15}$$

with σ^{tot} the fluid stress given by:

$$\sigma^{tot} = -(p + \frac{\rho_f}{2}|u|^2)I_3 + 2\mu(s(u))Du. \tag{4.16}$$

and

$$I(t) = \begin{cases} ((I_p + I_0 * sin(\pi * (t - ts)/Tsys)) \times \vec{n}, & 0 \leq t \leq T_{sys} \\ ((I_p + I_c * sin(\pi * (t - td)/(T_c - Tsys))) \times \vec{n}, & T_{sys} \leq t \leq T_c. \end{cases} \tag{4.17}$$

$I_p = 10\ \ cm/s$ represents the dominant flow, $I_0 = 10\ \ cm/s$ and $I_c = 15\ \ cm/s$. T_{sys} is taken equal to 0.35s. The remaining duration from the cardiac cycle corresponds to the diastole. The profile of this function is similar to that given in figure 5.11.

Outlet boundary conditions are those of a 2 element Windkessel model. The momentum and continuity operators are defined exactly the same as in **??** and **??** except that the vector of solution u has three components instead of two. We conserved the same values for Windkessel parameters, that said, the peripheral resistance of the arterial system considered is taken equal to $R = 0.95 mmHgs/cm^3$, while the arterial compliance is $C = 1.06 cm^3/mmHg$.

The initial conditions is a Poiseuille profile at the inlet:

$$f_{ini} = u_0 \times (1 - \frac{x^2 + y^2 + z^2}{R^2}) \times \vec{n}$$

where $u_0 = \frac{R^2}{4\mu}$ is the constant of Poiseuille.R is the approximate radius of the inlet section, calculated by dividing by two the maximum distance between two points of the inlet contour. $\mu = 0.006$ is the value of the constant viscosity.

$\vec{n} = \begin{pmatrix} n_1 \\ n_2 \\ n_3 \end{pmatrix}$ is the normal to Γ_{in}.

The corresponding initial distributions are given in figure 4.8:

4.4.2 Details about the numerical simulation

The semi-implicit scheme was the most appropriate in our case, since it is less constraining than the explicit for stability, and easier to implement than the implicit scheme because of the non linear form of our problem, especially with the additional terms add to incorporate Windkessel boundary conditions. We implement this within FreeFem++ parallel environment under a cluster. The initial 3D surface mesh was manipulated and labelized using GMSH. The 3D volume mesh was in a first place created under GMSH for tests and then using tetgen inside the FreeFem++ script. This last option is more convenient since we can

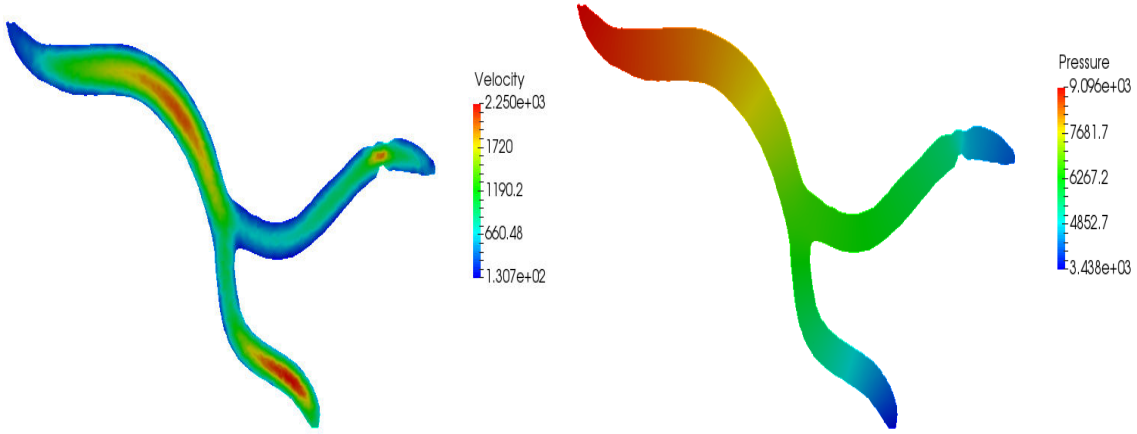

Figure 4.8: Left to right, 2D slices of the initial velocity and pressure fields for simulations.

fix the volume of tetrahedra as well as the minimal size of the mesh to avoid having any instability in the scheme. The time step used in all simulations is $dt = 10^{-2}s$, which mean that there is about 80 iterations for each cardiac cycle of $T_c = 0.8s$. The 3D volume mesh contains about 16043 tetrahedras and one simulation of one cardiac cycle takes about 35 minutes using 16 cores of the cluster. P23d element were chosen for velocity components and P13d for the pressure.

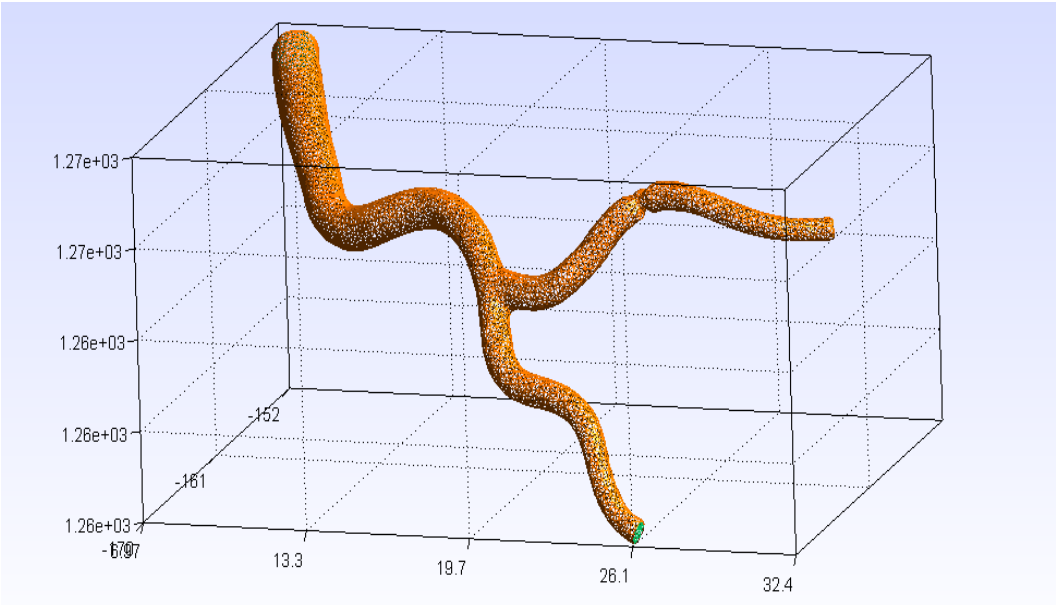

Figure 4.9: 3D mesh of the coronary tree used for simulations.

4.4.3 3D results

In the following figures we have the 3D results: velocity and pressure distributions at two characteristic times of the cycle: peak systole corresponding to the highest amplitude of the first sinusoid of the inlet flow function and peak diastole that is the highest amplitude of the sinusoid during diastolic phase, see figure 4.3 of the third chapter. Values of velocity in all the elements of the 3D tree follow the profile of the inlet. However, the amplitude is not the same but varies while moving through the two branches of the tree. Since the 3D tree is not belonging to the same plane (but is corrugated in space), this accelerates the flow in some areas and curbs it in others. Also the variant caliber (diameter) of the branches, or the presence of lesions privileges or not the flow in some branches in the opposite of the others. Since All these effects are illustrated in figures 4.10 and 4.11.

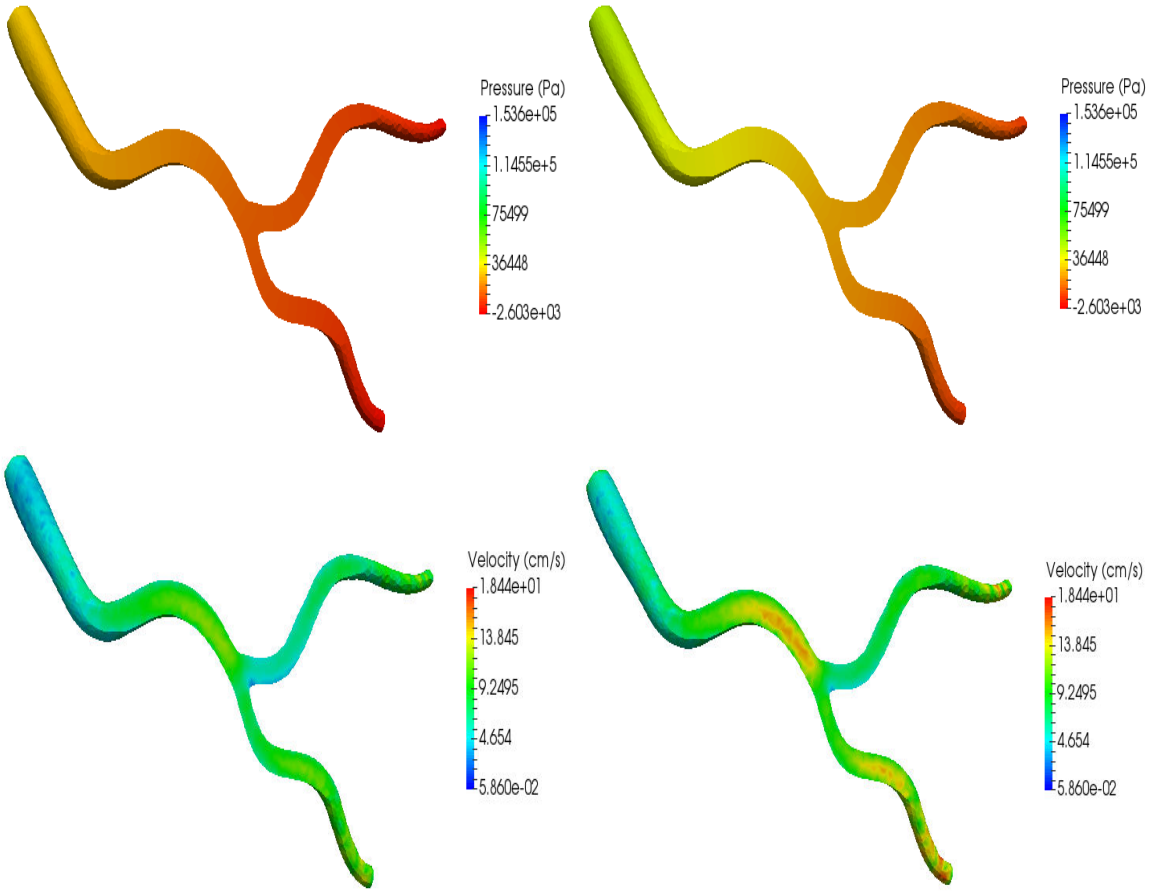

Figure 4.10: Top, pressure fields inside the healthy coronary tree at peak systole (left) and peak diastole (right). Bottom, corresponding velocity fields.

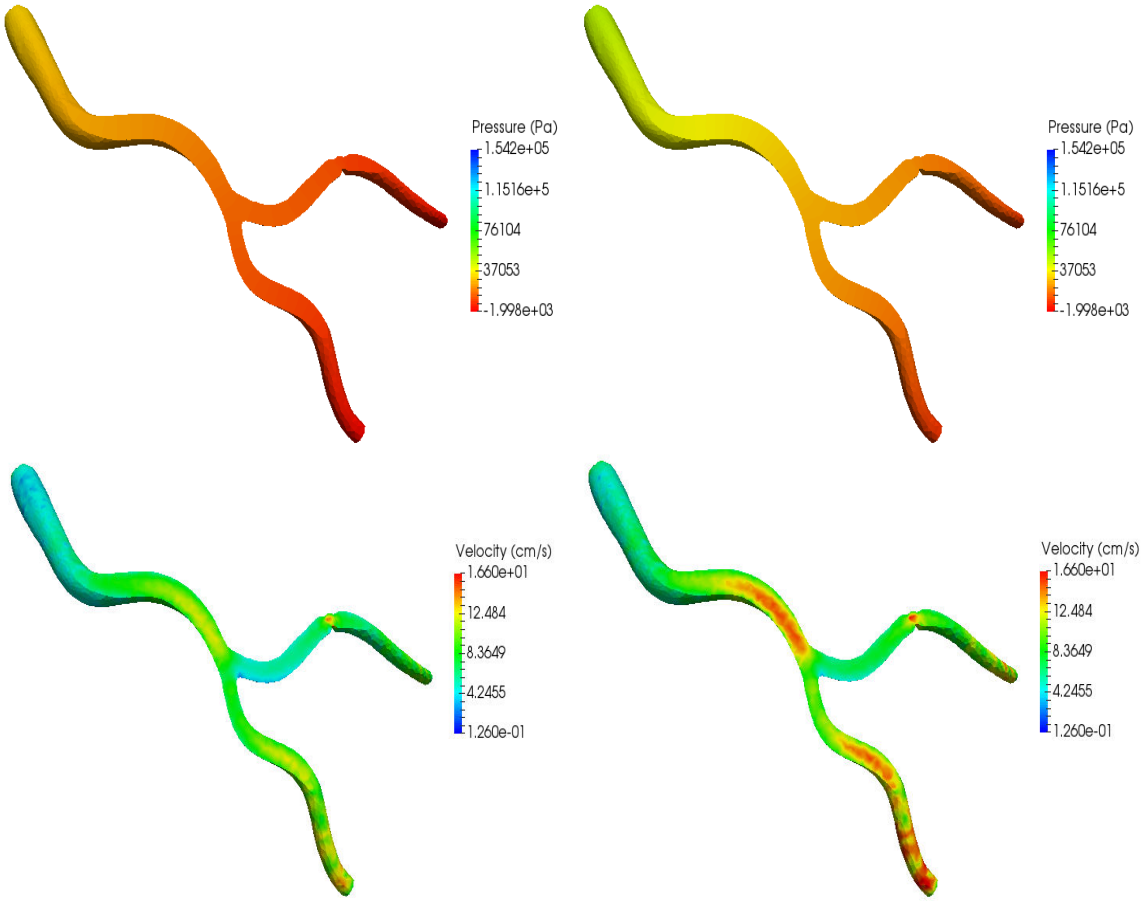

Figure 4.11: Top, pressure fields inside the diseased coronary tree at peak systole (left) and peak diastole (right). Bottom, corresponding velocity fields.

4.5 Drift quantification

We can observe from the results in the figures that for both the healthy and diseased portions the values of pressure decreases going from the inlet to the peripheral branches. For both cases, blood flow is favoured in the left branch due to gravity reasons because this one is more elongate in contrary to the right branch that is twisted. This problem is amplified when the lesion is added since the flow in this branch becomes more constraining. For this reason values of velocity are higher in the left branch.

4.5.1 Conclusion

In this chapter we calculated the fractional flow reserve (FFR) corresponding to a 2D multi-stenotic patient specific coronary tree issued from an angiography. The two lesions of interest were not present in the original image, but were incorporated artificially into the tree. The two intermediate lesions of interest have degrees of stenosis of 68% and 56%. The FFR classification for these two lesions was not sensitive to the flow model adopted for the simulation even if the FFR value were slightly different between the Navier Stokes and the non-Newtonian flow model. However, according to the chosen option for outlets boundary conditions we could have a different lesion classification. Based on the finer mesh simulations, the second lesion moved from the insignificant to the significant value range stenosis. Based on the simulation results, we summarize following conclusions:

- There is a good agreement between Navier Stokes and the generalized flow model in simulating coronary blood flow and thus in classifying coronary lesions provided fluid parameters are appropriate, see [3].
- Free outlet boundary conditions are not realistic to consider for FFR computation, since they are sensitive to the FFR sensor position. Moreover, they do not reproduce the resistant effect of the coronary downstream bed. In contrary to the Windkessel model even if the parameters R and C are taken constant.
- The study confirms the fact that the degree of stenosis is not enough to quantify the severity of a lesion, see [17]. In our case, the two considered lesions had different classifications in each time outlet boundary conditions were modified.

Based on the conclusions we obtained for the 2D coronary tree - since a 2D geometry is not enough realistic to represent important features of the flow in a real diseased coronary tree - we extended the simulation to 3D using the same 3D non Newtonian flow model as in [2] and a 3D version of Windkessel boundary conditions. Results obtained in 3D are in accordance with those in 2D, but no comparative study was established to clinically

validate the features obtained. We could not also compute the 3D FFR for the 3D tree considered at this stage of the thesis. Our aim was to place emphasis on the sensitivity of the FFR calculations and flow features in coronary arteries to the physical model, the boundary conditions and the space discretization as well, keeping out of scope the important purpose of validating virtual FFR against clinical data. Indeed, the FFR value issued from the 2D simulations can not be directly compared to the real invasive FFR, since a 2D angiography based reconstruction of the coronary tree is not the best representation of the physiological domain.

In the next chapter, we aim to study the drift induced on the value of the estimated virtual fractional flow reserve, due to the change in the configuration of the sensor during the measure. We use gaussian processes to generate a set of sensor's designs with varying parameters and a set of diseased arterial portions to create an FFR map.

Chapter 5

Fractional flow reserve prediction using gaussian processes

Abstract

Due to lack of standardization while making the invasive FFR measurement, this index encounters many sources of uncertainties. In this chapter, we investigate - trough simulation- the effect of the FFR device position and configuration on the FFR value computed. In 2D, we consider the same flow model as in the previous chapter 4 combined with different boundary conditions. The FFR device is assimilated to a disk in a first place, its position is subject to change. In 3D, we use the non Newtonian flow model introduced in the previous chapter 4. The 3D domain corresponds to a diseased arterial portion to which we introduce a 3D FFR device (wire+sensor) with a given length and coefficient of bending. These two parameters are used later to generate a GP model for FFR prediction that indicates a good accuracy. We implement an automated R function that generates the necessary meshes and FreeFem++ codes to resolve the elastic and fluid problems to compute a final FFR value corresponding to each GP design. We demonstrate using both the 2D and 3D model that the virtual FFR value is subject to change because of these sources of error which may lead to a misclassification of coronary lesions.

5.1 Introduction

As introduced in the first chapter 2, Fractional flow reserve derived from the initial coronary physical approaches. It gives a hemodynamic significance of coronary lesions by coupling the anatomic severity of stenosis with its physiological impact. Since its initial proof of feasibility in humans, it contributed in improving diagnostic performance, as demonstrated by the clinical study in [11]. The FFR measurements are performed using a 0.014 inches guidewire incorporating a distal pressure sensor, capturing the transtenotic (distal) pressure gradient P_d as illustrated in 5.1. To improve FFR work-flow, pressure measurement is made during maximal vasodilation using adenosine hyperemia, see [35].

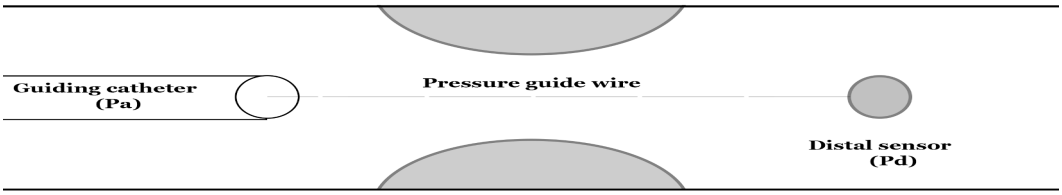

Figure 5.1: Main elements of FFR measurement: guiding catheter, pressure guide and distal sensor.

As a reminder, the FFR value is calculated by the ratio of P_d over the upstream aortic pressure P_a, that is measured proximal to the lesion (usually at the root of the aorta). Both these pressures, P_a and P_d, given by the FFR device are calculated as a temporal mean, over the cardiac cycle T_c, of pressures $p_s(t)$ captured at each frequency drop by the sensor, see [29]. These pressures can be written as follows:

$$P = \frac{1}{T_c}\int_0^{T_c} p_s(t)dt \tag{5.1}$$

Pressure Drift

All FFR measurement are susceptible to drift. Pressure drift is a degradation in the precision of the measurement that can deviate from the original calibrated state, defined by the practitioner. Pressure signal drift may occur in the value of the distal pressure P_d. This mainly comes from changing sensor sensitivity due to temperature changes, moisture around the wire surface or microcatheter, microbubbles on the transducer, or from electrical interference caused by blood or fluid at the wire/signal couple interface. Pressure drift may also

be related to the aortic pressure P_a measurement part of the FFR procedure. Changing the height of the aortic pressure transducer, capillary forces within the catheter, wedging of the guide catheter in the coronary ostium, a loss of pressure through the wire introducer tool, are possible causes of a varying pressure signal [35]. The drift is an evitable phenomenon and it is clear how it can decrease the accuracy of FFR measurement leading potentially to stenosis misclassification. This doubt in the accuracy of the FFR test is at the origin of most of recent criticisms addressed to FFR, like in FUTURE study, see [47].

There is an urgent need to investigate these unresolved issues in a large prospective study including a wide range of vessel and lesion types. The biggest limitation to this kind of studies is the technical aspect of assessing coronary pressure wire-derived FFR and in particular challenges with manipulating stantard pressure wires and hesitancy to pull back the pressure wire sensor to check for pressure drift after having crossed a stenosis, see [34]. In this view, a virtual assessment of the fractional flow reserve FFR can be an interesting alternative. In this chapter, we are interested in the study of the drift introduced during the evaluation of the distal pressure P_d. To do this, we will not go into the technical details of the sensor itself. However, we will give special concern to the effect of the distal wire position and configuration on the calculated FFR. In the first section, we present some 2D results based on a simplified design of the FFR pressure wire, see figure 5.1. We use a Non Newtonian fluid model presented in our paper [29]. The perturbation created by the catheter as well as the pressure guide are not taken into account and the pressure sensor is assimilated to a simple disk. The perturbation on the value of P_d is mainly due to the sensor arbitrary position during the test. No variable parameters were considered for the lesion or the sensor. In the second section, we present a 3D geometrical design of the FFR device (pressure wire + sensor), see figure 5.2. Blood flow inside the 3D domain was simulated using the same fluid model as in the previous chapter 4. We introduce two sources of uncertainty on the P_d measure: Firstly, the sensor bending due to the practitioner's manipulation. Secondly, the small differences in the guide length distal to the lesion during different FFR tests can induce a perturbation in the FFR value even for the same lesion. These two parameters were considered as variables to generate a set of sensor designs based on Gaussian process in order to obtain an FFR map according to these two variables. The same stenotic plaque was considered at a first place. The methodology followed will be presented in detail in section 5.2.

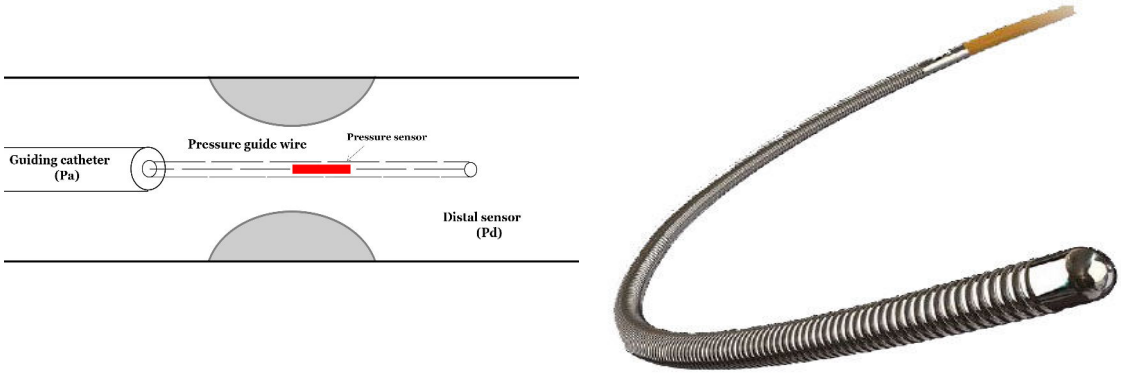

Figure 5.2: Left, a simplified 3D model of the device wire+sensor. Right, image corresponding to an optical FFR device from the market.

5.2 Quantification of the sensor position impact on the FFR value: 2D case

5.2.1 Sensor position: effect on the virtual FFR

FFR measure, as explained previously, uses pressure sensor-tipped intracoronary wires to quantify the transtenotic pressure gradient P_d. In this section, we introduce a simplified 2D sensor to the left coronary tree used in the previous chapter, in order to study the drift caused by the deviation of the sensor from its position of origin that is in general defined at the center of the branch cross- section, see figure 5.3.

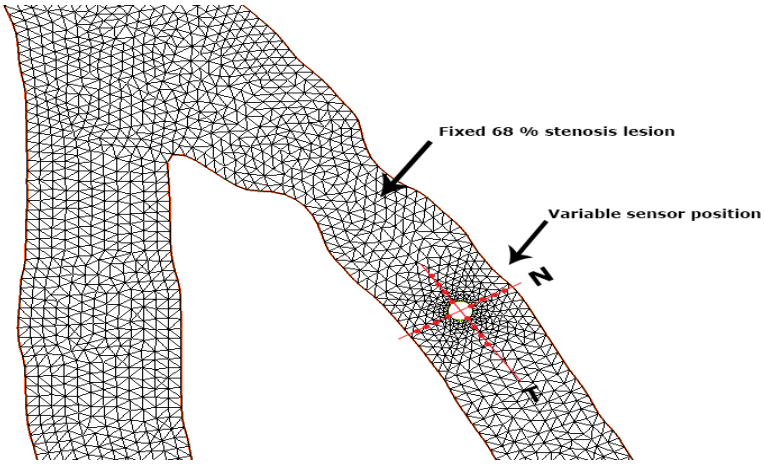

Figure 5.3: Distal sensor displacement according to the normal and tangential positions.

The common value for the sensor diameter is 0.014 inches, which corresponds to 0.35 mm. The mean value of the distal pressure P_d is measured using the sensor surrounding

points with a defined acquisition frequency. In this 2D study, we decide to consider only two sources of error that are: sensor displacement along the flow direction (vector T) and along the normal to flow direction (vector N), see figure 5.3.

In order to model the presence of the distal sensor, we incorporated a 2D disk in a position of reference, given in figure 5.3 We consider that this position is subject to variation due to the randomized aspect of the clinical intervention: the practitioner is not very precise as to the sensor position, two different practitioners can adopt two different positions for the test, which may modify the FFR value. The sensor position can be also changed due to the flow during the measure. Figure 5.3 shows how the sensor position can vary in the normal and tangential directions. The disk diameter is considered to be constant while the ratio between the sensor diameter and the reference diameter of the branch is: $\frac{D_{sensor}}{D_{ref}} = \frac{1}{10}$

We use this same 2D realistic geometry to study the impact of the distal sensor position on the virtual FFR value. In this case, the spatial mean of the distal pressure P_d is calculated over a physical domain: the disk that physically impacts the flow (not virtual like considered in the first chapters). As for the aortic pressure P_a , it is calculated in a virtual rectangle at 1cm from the entrance of the main branch of the arterial tree, since it is not directly linked of the FFR uncertainties.

In order to quantify the effect of the flow model and the outlet boundary conditions on the FFR value in presence of the distal sensor, we led different simulations. On the one hand, a comparison between the Navier Stokes model and the generalized flow model were made. On the other hand, a comparison between free outlet boundary condition and Windkessel model were established. From the two artificial lesions introduced in the previous chapter, only one was kept, that is 68% stenotic.

5.2.2 Numerical results: flow distributions

The following figures give velocity fields at different times of the cardiac cycle, in particular, at peak systole and peak diastole. The simulations were performed with both flow models: Navier stokes (the two figures in the right 5.4) and non Newtonian fluid model (the two figures in the left 5.4). Values of blood velocity vary from $2m/s$ to $19m/s$ and we can clearly observe that the values given by Navier Stokes are higher than those given by the non Newtonian flow model. This is due to the viscosity term that is constant in Navier Stokes in contrary to non Newtonian fluid model where the viscosity varies according to Carreau law introduced in the previous sections. The same type of boundary conditions is considered for all simulations: A 2 element Windkessel model presented in details in the previous chapter. We can also observe from the figures that the values of viscosity are higher at peak diastole than at peak systole for both models. That simply follows the flow profile given at the entrance of the coronary tree, given in the previous chapter 4.3.

The results are well representing of the difference between Newtonian and non Newtonian rheologies. In our case, non Newtonian flow model is more adapted to reproduce the flow. Firstly because the vessels' caliber in coronary arteries is small comparing to the aorta for example, for which Navier Stokes model is widely used. In this case, we cannot neglect the non Newtonian behaviour of blood, that is composed not only of plasma (that can be assimilated to a Newtonian fluid), but also of blood cells, that are the main factor behind blood viscosity. More precisely the frictions between them and against the arterial wall that are more important when the vessel's diameter is small.

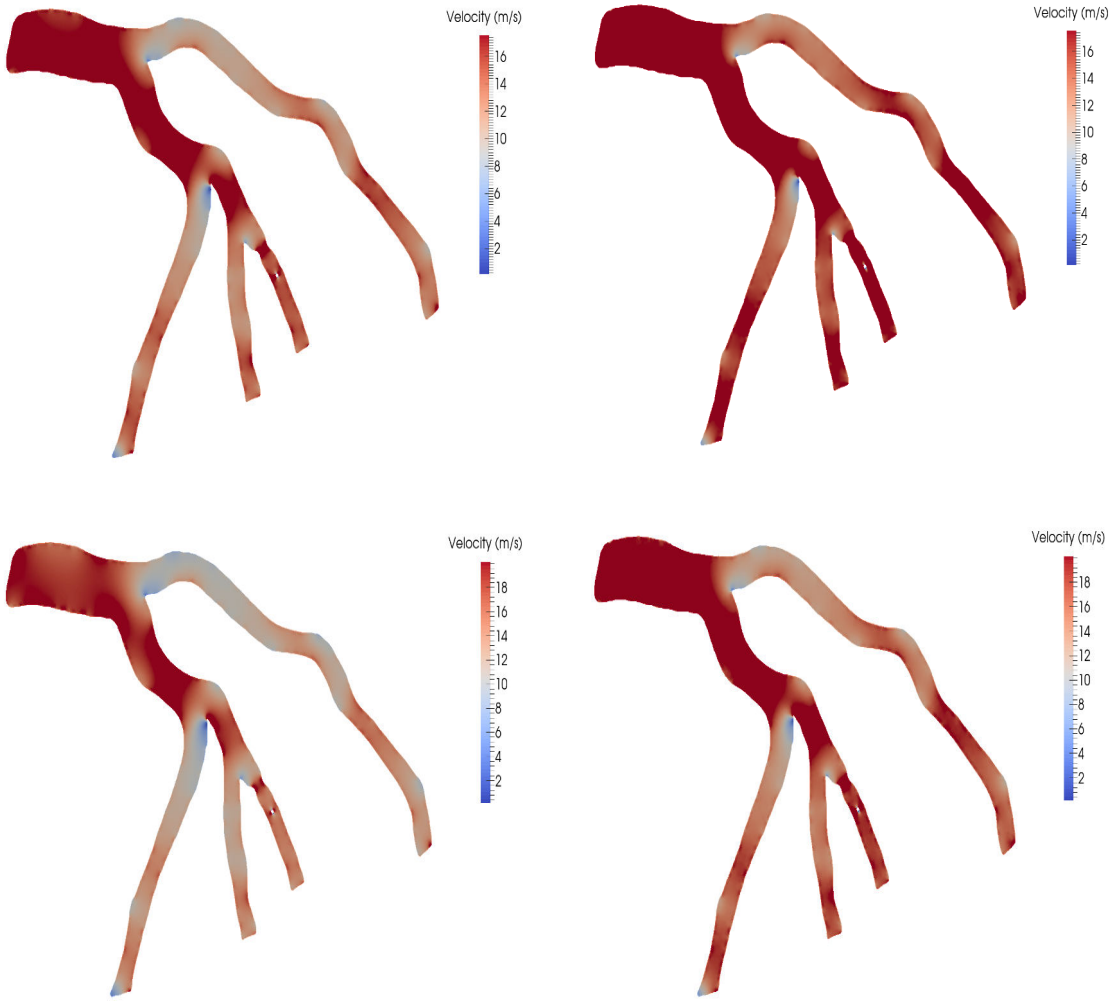

Figure 5.4: Top, velocity field using generalized fluid model at peak systole (left) and peak diastole (right). Bottom, velocity field using Navier Stokes at peak systole (left) and peak diastole (right).

The following figures 5.2.2 correspond to velocity fields near stenosis and around the

obstacle: that is the sensor wire in this case assimilated to a disk in 2D. Shear stresses are observed to be higher with non Newtonian flow model than Navier Stokes. FFR values obtained with both models are: 0.76 with Navier Stokes vs 0.747 with non Newtonian flow model. The difference between the value given by the two models is still minor which means that the lesions is classified in the same value range: hemodynamically important.

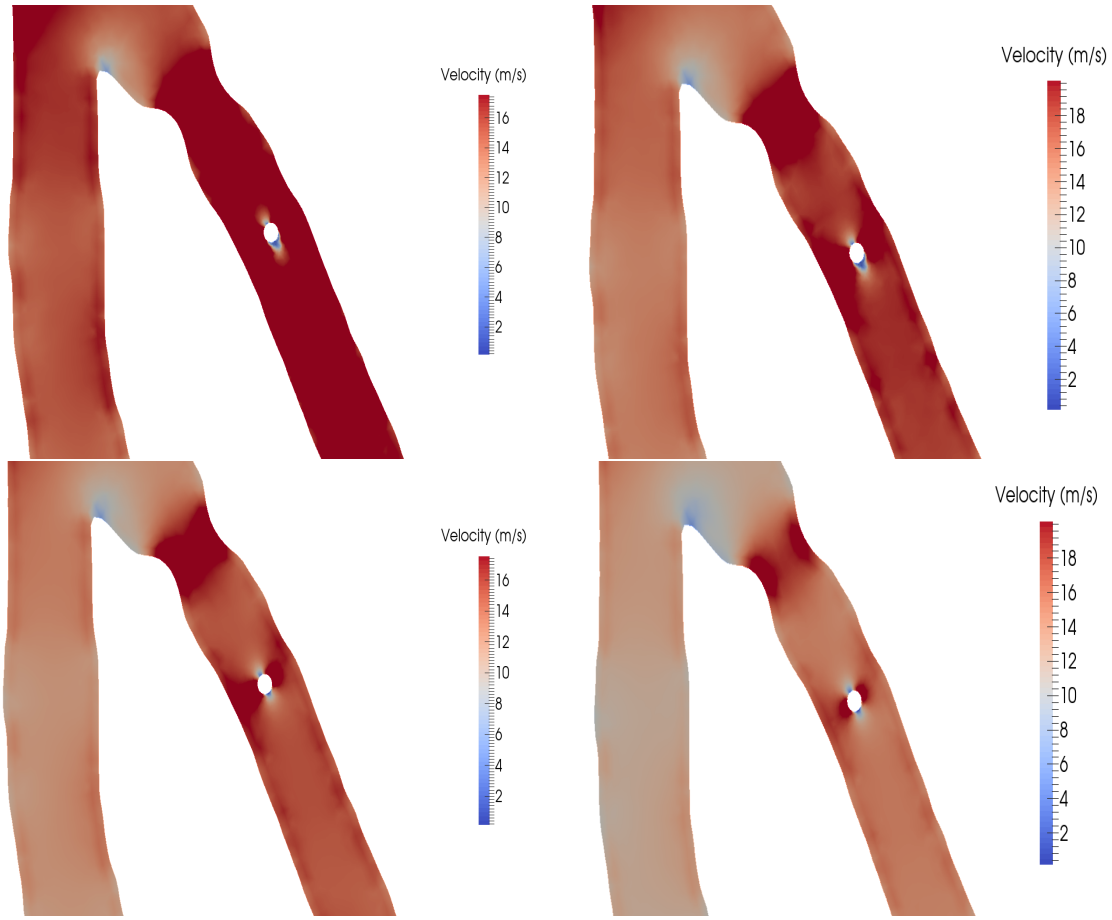

Figure 5.5: Velocity distributions near stenosis with the two flow models at different times of the cardiac cycle. Left, top peak diastole - generalized flow model; bottom peak systole - generalized flow model. Right, top peak diastole - Navier Stokes; bottom peak systole - Navier Stokes.

5.2.3 FFR variation corresponding to both directions

The following figures represents the variation in the FFR value for the fixed lesion. In each simulation, a different position of the sensor is considered. The graphic 5.6 - left represents a variation of the FFR value according to the normal to flow direction N (see figure 5.3), the tangential coordinate is fixed while the normal varies from $-3 \times hsize$ to $3 \times hsize$. hsize

represents size of the mesh is fixed and the diameter of reference of the artery is about $10 \times hsize$. The graphic 5.6 - right represents the variation of the FFR value according to the flow direction T (figure 5.3). The normal coordinate is fixed to the center of the branch while the tangential varies from $-6 \times hsize$ to $6 \times hsize$. For each position of the sensor, two simulations are run: one with Navier Stokes model and the other with non Newtonian flow model, to obtain two values of the virtual FFR, represented respectively in the blue and red curves (figure 5.6). In the two figures, a grey area is drawn to represent the critical zone for FFR values, the cut-off considered in this case is 0.75. We can see that with the two models, for each new positions of the sensor, the virtual FFR illustrates important variations. With Navier Stokes model (blue curve), the lesion was classified in the same value range for all the positions of the distal sensor: not hemodynamically significant. In contrary, with the generalized flow model, $8/26$ positions of the distal sensor classified the lesion to be hemodynamically significant while the remaining positions gave the opposite conclusion. In all simulations, the same model for boundary conditions was considered: a 2 element Windkessel model as introduced in the previous chapter.

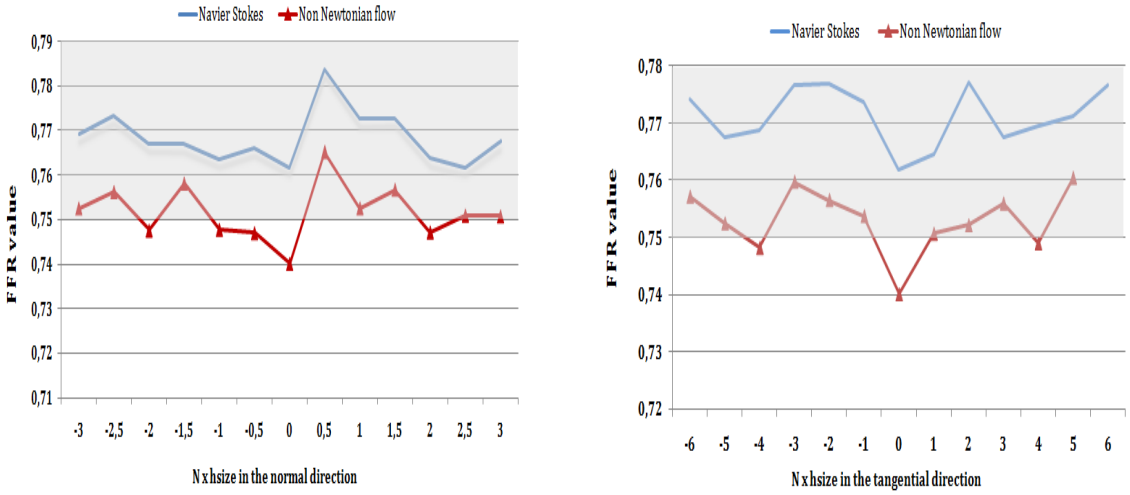

Figure 5.6: Left, comparison between FFR values for Navier Stokes and Non Newtonian flow model obtained by moving the sensor in the normal direction. Right, comparison between FFR values for Navier Stokes and Non Newtonian flow model obtained by moving the sensor in the tangential direction. The grey area represents critical FFR values.

The following graphics (figure 5.7) illustrate the effect of the boundary conditions on the virtual value of the FFR. These simulations combine in each time a different flow model: Navier Stokes vs non Newtonian flow model and different boundary conditions: Windkessel model vs free outlets BC, though this last choice is not very realistic. The FFR values represented in figure 5.7 correspond to a different lesion: the 56% stenotic lesion given in figure 4.5 of the previous chapter.

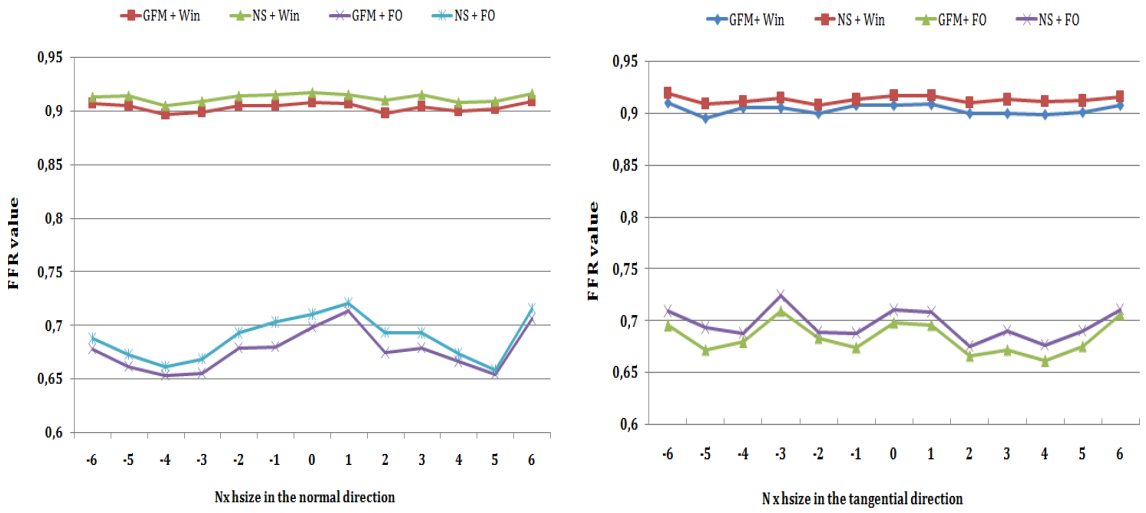

Figure 5.7: Left, comparison between FFR values for Navier Stokes and Non Newtonian flow model combined with free outlets or Windkessel BC obtained by moving the sensor in the normal direction. Right, comparison between FFR values for Navier Stokes and Non Newtonian flow model combined with free outlets or Windkessel BC obtained by moving the sensor in the tangential direction.

The only reason to adopt a different lesion in this case is the fact that this last is positioned at the entrance of the branch and that this branch is long enough to keep the distal sensor far from the outlet. This conditions is not verified in the first lesion since it is very close to the exit. Otherwise, we obtain an important pressure drop when free outlet boundary conditions are considered. We can see from the curves that for both flow models and for sensor's displacement in both directions the lesion is classified non significant if the outlet boundary conditions are Windkessel: virtual FFR beyond 0.85 and significant with free outlet boundary conditions: virtual FFR under 0.75. This first 2D approach was adopted to illustrate the eventual variability on the FFR value calculated due to the perturbation in the distal sensor's position. Which make it possible to obtain two contradictory medical decisions for the same lesions if the circumstances of the FFR intervention are different. This factor is one of the sources of drift. In the next section, we present a 3D approach to illustrate the drift in the value of FFR.

5.3 Quantification of the sensor position impact on the FFR value: 3D cases

5.3.1 Sensor bending problem

In order to model the sensor movement during the FFR test, we consider that the sensor deforms under the action of the practitioner. That implies a displacement from the original position of the sensor, which is the position of reference (considered to be the center of the arterial portion, see figure 5.9). Since the sensor and the arterial portion diameters are small - few millimeters - we can assume that we are in the case of small displacements, which means that we can use Hooke's law to simulate the sensor displacement and to obtain an initial configuration of the sensor inside the diseased arterial portion before to compute the virtual FFR.

Hooke's law is given by the following equation, where σ_{ij} is the stress:

$$\sigma_{ij}(u) = \lambda \delta_{ij} \nabla . u + 2\mu \varepsilon_{ij}(u)$$

where δ_{ij} is the Kronecker symbol, and ε_{ij} the strain tensor given by:

$$\varepsilon_{ij}(u) = \frac{1}{2}(\frac{\partial u_i}{\partial x_j} + \frac{\partial u_j}{\partial x_i})$$

The two constants λ and μ describes the elastic property of the solid, they are given by:

$$\mu = \frac{E}{2(1+\nu)}, \ \lambda = \frac{E\nu}{(1+\nu)(1-2\nu)}$$

The values of parameters are: Young modulus $E = 21.5 \times 10^4$ and Poisson coefficient $\nu = 0.29$. Then we simply use:

$$-div(\sigma) = G$$

G is the gavity force. The variational form can be written as:

$$\int_{\Omega_s} \lambda \nabla . u \nabla . v + 2\mu \varepsilon(u) : \varepsilon(v) dx - \int_{\Omega_s} vG dx = 0; \tag{5.2}$$

The considered 3D geometry for the sensor is given in the following figure 5.8:

As for boundary conditions, we consider that the inlet side of the pressure guide is fixed: $u = 0 \ on \ \Gamma_1$. After solving this Lame system, we obtain a set of initial configurations to the pressure sensor, by varying the gravity coefficient G. The following figure 5.9 shows

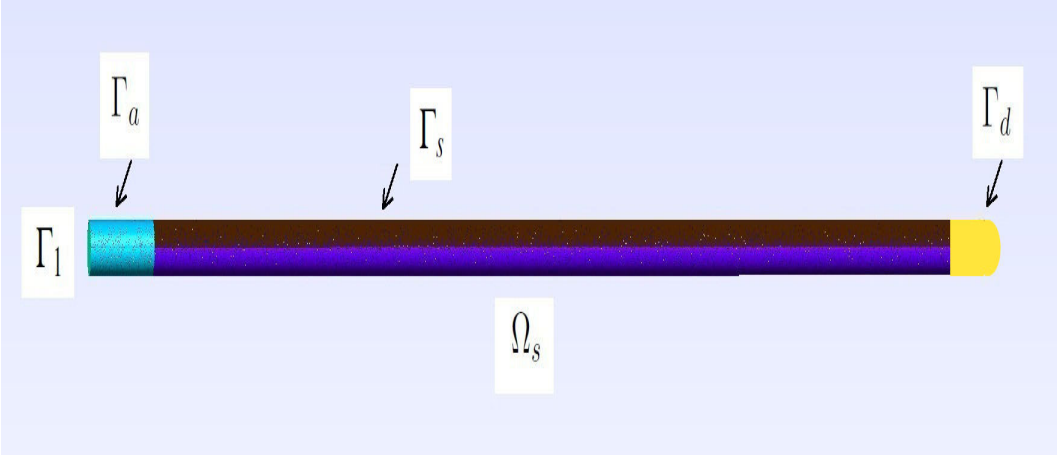

Figure 5.8: 3D configuration of the pressure guide + sensor.

an illustration of the configuration of reference and the two possible cases resulting from bending.

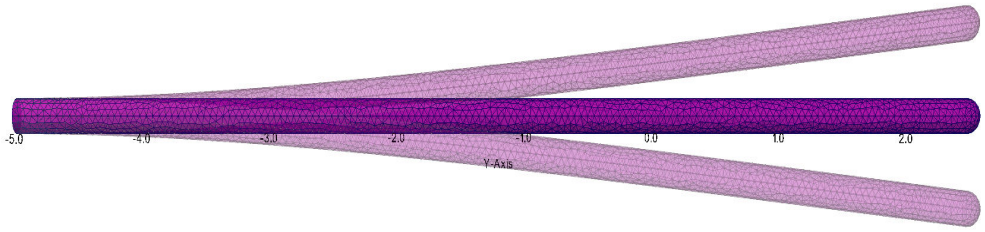

Figure 5.9: Position of reference of the pressure sensor and the two new configurations due to bending.

This new sensor 3D meshed domain is after that introduced inside the diseased arterial portion, where we define a 3D flow problem, given in details in the next subsection.

The diseased arterial portion corresponds to a cylinder of length $L = 10$ and radius $H = 1$. The stenosis is assimilated to an ellipsoid. Given the values of parameters considered the degree of stenosis is 25% and the lesion's radius $1.2cm$. As for the 3D sensor, it has a fixed radius of 0.1 that respects the common ratio of $1/10$ between the arterial diameter and the guide. This radius is kept constant for all the simulations presented in the next section. In the opposite to the sensor length that is taken variable.

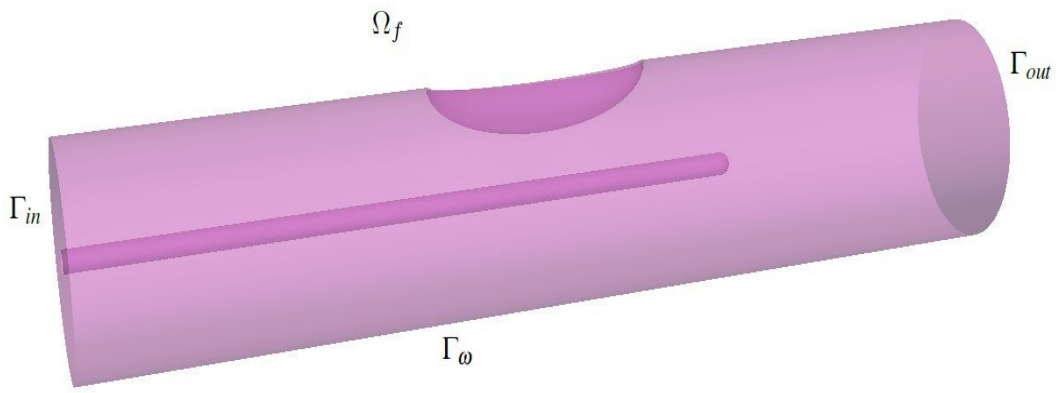

Figure 5.10: The diseased arterial portion + the FFR guide/sensor.

5.3.2 3D Flow model for simulations

The 3D non Newtonian flow equation is the same introduced in the previous chapter 4, given in equation 4.13 This equation is completed with suitable boundary conditions on Ω_f (n is the normal) :

$$\sigma^{tot}(u,p).n = h, \;\; in \;\; \Gamma_{in} \times (0,T_c), \tag{5.3}$$

$$\sigma^{tot}(u,p).n = 0, \;\; in \;\; \Gamma_{out} \times (0,T_c) \tag{5.4}$$

$$u = 0, \;\; in \;\; (\Gamma_\omega \cup \Gamma_a \cup \Gamma_s \cup \Gamma_d) \times (0,T_c), \tag{5.5}$$

with σ^{tot} the fluid stress given by:

$$\sigma^{tot} = -(p + \frac{\rho_f}{2}|u|^2)I_3 + 2\mu(s(u))Du. \tag{5.6}$$

The expression of the velocity profile at the inlet is given by :

$$h = (U_0 + U_m \times sin(\omega \times t)) \times (1 - \frac{x^2+y^2+z^2}{H^2}) \tag{5.7}$$

The initial solution is a steady Stokes with a Poiseuille 3D profile at the inlet.

Parameters:
$\rho_f = 1060\ Kg.m^{-3}$ is the blood density. $U_0 = 10m/s$ the initial value of blood velocity, $U_m = 20m/s$ the maximal value of velocity, $H = 1mm$ the portion's diameter, $\omega = \frac{2\times\pi}{T_c}$ where $T_c = 0.8s$ the conventional duration of a cardiac cycle.

5.3.3 Details about numerical simulation

All 3D simulations were performed using freefem++ parallel. MPI interface was utilized in order to have access to all the libraries and solvers available. New numerical challenges appears once we moved to 3D:

- Big 3D mesh files that implies a huge need in system memory. Reducing the number of elements in the mesh was not a possible option since we aimed to obtain more accurate solutions and FFR values.
- Beyond memory issues, the simulation with a simple solver took about 3 days, to obtain one final FFR value.
- Trying to find a compromise between the accuracy of the solution and the time of simulation led us very often to stability problems in the semi-implicit numerical scheme: stability condition not verified.

For these reasons, a parallel implementation of the resolution algorithm was necessary. All parallel simulations were run under the cluster vSMP of the laboratory Jean Alexandre Dieudonné LJAD - University Côte d'Azur. For more informations about this cluster, see [40]. The cluster has 7 nodes (140 cores) aggregated in one big machine with ScaleMP technology, see [41], with a total memory of 400 GBytes. Under the cluster, two main FreeFEm++ solvers were tested. We started a first computation with GMRES solver, that took about 22 hours using 32 cores for only one cardiac cycle of $0.8s$ and with a time step of $dt = 0.01s$. Considering the challenges we had and the short delays to provide usable results, we had to use a parallel solver that takes less time. The MUMPS solver, also implemented under FreeFem++ environment, was recommended by many FreeFem++ users. MUltifrontal Massively Parallel Solver (MUMPS) is a free library that solves linear system of the form $Ax = b$ where A is a square sparse matrix with a direct method based on a multifrontal approach, see [24] for more details. Thanks to the new matrix implementation and to MUMPS solver, time of resolution was considerably reduced to 7h30min using 16 cores and 2h15min using 32 cores. The simulation this time was run during three cardiac cycles of $T_c = 0.8s$ with a time step of $dt = 0.01s$. The memory space available under the cluster was enough to get over all meshing problems. The main steps of the resolution algorithm are as follows:

Algorithm of resolution

- Calling MPI parallel solver.
- Importing the portion's and the sensor's mesh. The two initial meshes are 3D surface meshes.
- Creating 3D volumic mesh using tetgen. This software is a tetrahedral mesh generator of a three dimensional domain defined by its boundary. The input domain take into account a polyhedral or a piecewise linear complex. This tetrahedralization is a constrained Delaunay tetrahedralization. For further details about this software, see [42]. The tetrahedralization used for all simulations has a maximum volume of 0.001. The corresponding mesh file has a size of 2938260 octets: 76490 tetrahedras (17383 vertices and 20132 triangles).
- Creating FEM spaces: P23d continuous finite elements were chosen for the three components of the velocity field and P13d for the pressure.
- Giving the necessary physical and numerical parameters for simulation.
- Solving steady Stokes problem to provide the initial solution with a Poiseuille profile at the inlet.
- Defining the generalized non Newtonian numerical problem with a semi-implicit scheme based on the 3D problem defined in 4.13. The integration order for the 3D gradient term is three.
- Starting the time loop where, at the current cardiac cycle, at the current time step:
  1. Solving $Ax = b$.
  2. Calculating P_a and P_d as two integration factors: $P_a = \int_{\Gamma_a} pds$ and $P_d = \int_{\Gamma_d} pds$
  3. Adding the P_a and P_d value to the P_a^{cumul} and P_d^{cumul} (in order to calculate the mean P_a and P_d at the end of the cardiac cycle).
  4. Saving solution and moving to the next iteration.
- Computing mean P_a and P_d from the previous cardiac cycle as well as FFR (ratio of the two values) and moving to the next cardiac cycle.
- After the final cardiac cycle, FFR is calculated as mean of all FFR values: in our simulations we considered three cardiac cycles.

5.3.4 Some 3D results

The following figures corresponds to 2D cuts of the velocity and pressure fields at three different moments of the cardiac cycle. We can observe the recirculation area created after the sensor. This phenomenon, mainly due to the non Newtonian aspect of the blood (as considered in Carreau law), affects the P_d value (and thus the virtual FFR) and makes it correlate considerably with the length of the sensor: distance between the distal end of the sensor and the lesion. The simulation results presented here corresponds to the position of reference of the pressure sensor, and no elastic property is taken into account. This effect also affects this re-circulation area and the FFR value. These effects will be quantified thanks to different parameters and explored in the next section using a Gaussian processes method.

5.3.5 Gaussian process modelling

In this section, we run a set of simulations in order to quantify and study the effect of the arbitrary configuration of the sensor inside the diseased coronary tree, or the randomized geometry of the stenosis on the FFR value computed. For this purpose, different parameters were introduced to quantify this effect. For each set of parameters, an initial configuration is given to the sensor (a 3D surface mesh is created) and to the diseased portion (for each vector of parameters, a different 3D lesion is created, shaped in this study, through two main geometrical quantities, one for the degree of stenosis and the other for the lesion's radius). As demonstrated in the previous 2D study given in chapter 3, and compared to a clinical study given in [17], these two quantities are enough to represent the functional significance of intermediate coronary lesions. One precise simulation of the FFR via the above methodology - given in section 5.3.3 - requires several hours of computing, on a cluster (minimum of 2h15min using 32 cores). Hence, quantifying the effect of the parameters of the model (e.g., properties the stenosis or position of the sensor) would become infeasible in terms of computational resources. The usual solution in this context is replace the computationally expensive simulator by a fast to evaluate surrogate model. Based on the idea that configurations closed to each other should have similar responses, Gaussian Processes (GP) are particularly popular for this task with their ability to give accurate predictions. This GP study was performed thanks to our collaboration with Mickael Binois from ACUMES, INRIA Sophia Antipolis.

Here we model the FFR depending on variables $\mathbf{x} \in \mathbb{R}^d$ as a zero mean Gaussian process Y with covariance kernel $k : \mathbb{R}^d \times \mathbb{R}^d \mapsto \mathbb{R}$, a positive definite function. Given n observations $\mathbf{f} = \{f_1, \ldots, f_n\}$ of the FFR at designs $\mathbf{x}_1, \ldots, \mathbf{x}_n$, multivariate normal conditional identities

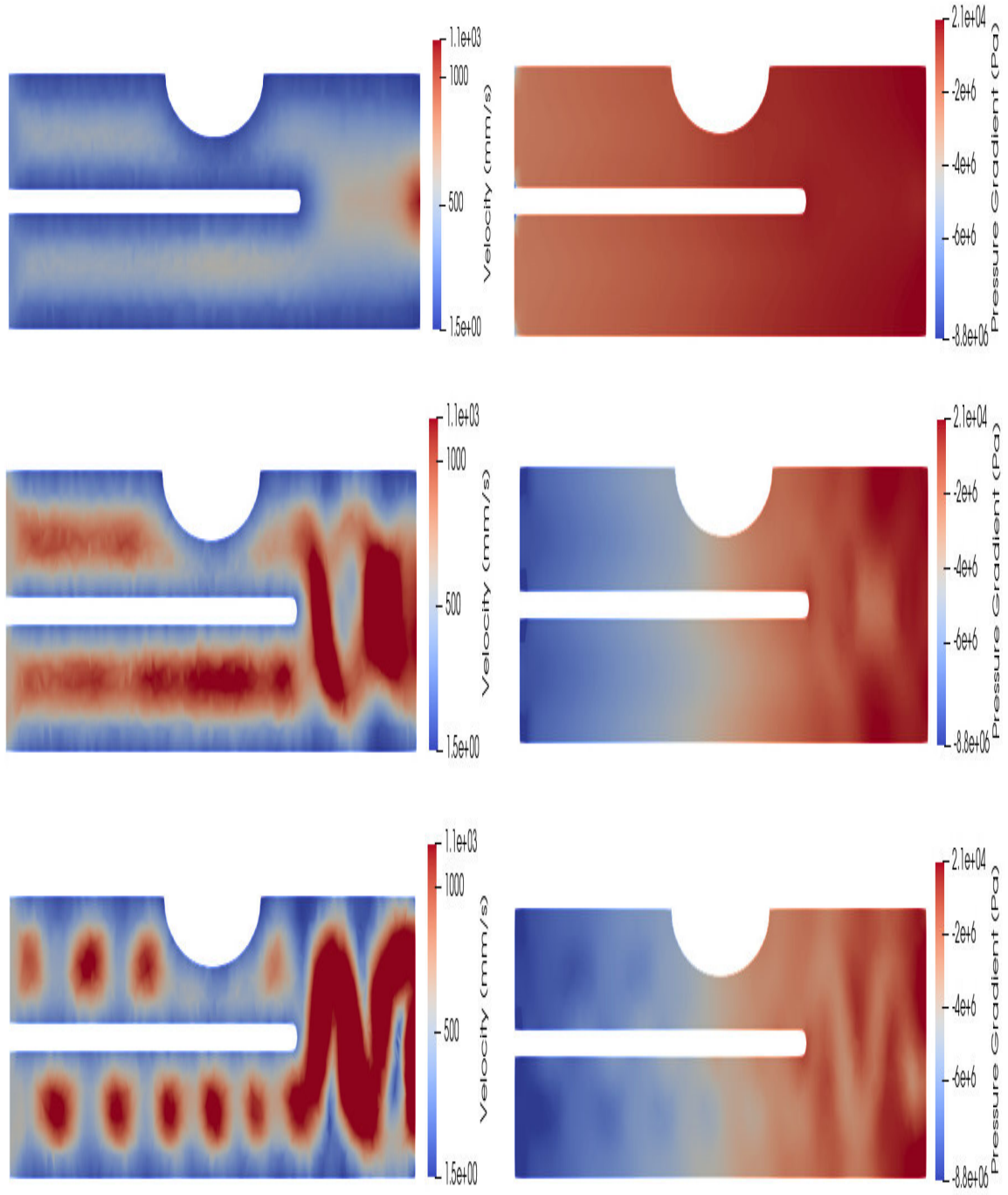

Figure 5.11: Left, blood velocity at three different times of the cardiac cycle. Right, corresponding blood pressure fields.

gives the prediction of the FFR at $\mathbf{x}$, $Y|\mathbf{f} \sim \mathcal{N}(m_n(\mathbf{x}), s_n^2(\mathbf{x}))$ with:

$$m_n(\mathbf{x}) = \mathbf{k}(\mathbf{x})\mathbf{K}_n^{-1}\mathbf{f}$$
$$s_n^2(\mathbf{x}) = k(\mathbf{x},\mathbf{x}) - \mathbf{k}(\mathbf{x})\mathbf{K}_n^{-1}\mathbf{k}(\mathbf{x})^\top$$

where $\mathbf{k}(\mathbf{x}) = (k(\mathbf{x},\mathbf{x}_i))_{1\leq i\leq n}$, $\mathbf{K}_n = \big(k(\mathbf{x}_i,\mathbf{x}_j)\big)_{1\leq i,j\leq n}$. In practice, k usually takes a parametric form such as the Gaussian or Matérn family, whose parameters are estimated via maximum-likelihood. We refer to [43] for more details on GP regression.
At a first place, we decided to run a 2D Gaussian process study, where the vector of parameters is in $\mathbb{R}^2$. For the same lesion of 25% and with a radius of $1cm$, we vary the parameters of the sensor's configurations. We used two main quantities:

- The length L of the sensor, see figure 5.9.
- The bending $coef$ of the sensor: deviation from the position of reference that is the center of the portion. The illustration of the deformation is given in figure 5.9 and the corresponding elastic problem is defined in details in section 5.3.1.

For each vector of parameters $x_i = (L_i, coef_i)$, a cascade of events is triggered. The main steps are described as follows:

1. Giving the initial sensor mesh with the length L_i in the configuration of reference to the elastic problem with $G = coef$ (problem 5.2) to obtain the new deformed configuration.
2. Adding the new 3D sensor's mesh to the fixed diseased portion's mesh to create the initial volumic mesh to run the resolution algorithm given in 5.3.3 and obtain the corresponding fractional flow reserve FFR_i

An initial set of twenty experience was run (20 vectors of parameters) to build the GP model. In each group of experience, a maximum of three outlayers was observed: we proceeded by deleting them. The corresponding results of the samples (initial + add through sequential training) are given in table 5.1. After fitting a GP model, it needs to be validated for further use. A common procedure is to train it on a part of the data and verify that the prediction is relevant on the hold-out set. For instance, we can check the root mean squared prediction error or the prediction intervals. The quality of the prediction depend on the choice of the initial n observation location, which are commonly selected as a max-min Latin hypercube for their space filling properties. If necessary, sequential strategies can be used to further refine design of experiments with new observations that are the most informative about the task at hand.

Once the GP is sufficiently precise, the surrogate can be used to estimate quantities of interest, say, for instance:

- the variance of the FFR due to uncertainty in the position. Separating variables about the position of the sensor from the rest: $\mathbf{x} = (\mathbf{x}_p, \mathbf{x}_q)$, this quantity can be written as $\mathbb{V}ar(Y(X_p, \mathbf{x}_q))$ with X_p a random position.
- the mean FFR marginalizing over the position $\int_{D_p} Y(\mathbf{x}_p, \mathbf{x}_q) d\mu(\mathbf{x}_p)$.
- the maximum/minimum of the FFR given characteristics of the stenosis: $\max_{\mathbf{x}_p} Y(\mathbf{x}_p, \mathbf{x}_q)$.

Results from 2D data

Sample i	L_i	$coef_i$	FFR_i
1	2.18	21	0.673188
2	2.6	26.4	0.623142
3	2.36	39	0.65419
4	2.66	50.4	0.608595
5	2.94	34.2	0.554545
6	2.74	11.4	0.613949
7	2.21	45	0.133888
8	2.45	18	0.643645
9	2.76	42	0.59215
10	2.31	4.08	0.684436
11	2.5	56.4	0.649058
12	2.075	32.4	0.888446
13	2.81	29.4	0.570834
14	2.62	13.2	0.75374
15	2.53	43.2	0.637968
16	2.016	0.9	0.709227
17	2.12	58.8	0.692804
18	2.96	8.4	0.542237
19	2.88	52.2	0.582604
20	2.26	22.8	0.663284
21	2.482	33.48	0.637789
23	2.45	18	0.643645
24	2.455	7.56	0.653798
26	2.382	50.88	0.649064
27	2.818	19.98	0.574916
28	2.6	26.4	0.623142
29	2.382	50.88	0.649064
30	2.818	19.98	0.574916
32	3.586	-42	0.357732

33	3.834	4.92	0.406385
35	3.82	43.56	0.34358
36	3.032	-47.64	0.54053
37	3.972	-31.44	0.235393
38	3.552	37.8	0.363824
39	2.1434	-48.828	0.6851
40	3.396	-33.24	0.454975
41	3.982	12.12	0.163693
42	3.318	39.36	0.45481
43	3.456	-5.04	0.450934
44	2.746	-48.132	0.97368
45	3.774	-48.228	0.37447
46	2.264	-51.804	0.67171
47	3.39	58.44	0.472278
48	3.958	48.84	0.303138
49	3.86	-59.0136	0.38006
50	3.342	-60	0.501422
51	3.256	0.4800	0.520874
52	2.48	-22.68	0.636965
53	2.948	-28.56	0.553173
54	3.712	55.08	0.404327
55	2.1564	-24.12	0.68164
56	2.0274	34.2	0.704215
57	3.694	-29.52	0.316196
58	3.954	-14.04	0.190627
59	3.216	-13.08	0.46632
60	3.576	15.12	0.371547
61	2.00918	-49.884	0.708
62	3.158	59.88	0.520237
63	3.546	-58.416	0.44344

Table 5.1: Two parameters design experiments: parameters and corresponding FFR values

We start by considering two parameters to illustrate the interest of GP modelling in this context. These parameters are the distance $L \in [2,4]$ of the sensor to the stenose center and the angle $coef \in [-60°, 60°]$ of the sensor toward the stenose. We started by generating 20 initial designs, completed by 37 new designs. We removed 6 results whose computation was problematic. The designs parameters and the corresponding FFR values are given in table 5.1. After fitting the GP model, we obtain the resulting prediction is given in figure 5.12.

To validate the GP predictions, we randomly selected 11 designs as testing locations and used the remaining 40 for training. As shown in Figure 5.13, all the prediction interval intersect the diagonal line, indicating good accuracy. We can now estimate quantities that cannot be computed directly with expensive FFR computations. We start with the effect of the uncertainty on the sensor's position. The position is considered as uniformly sampled on

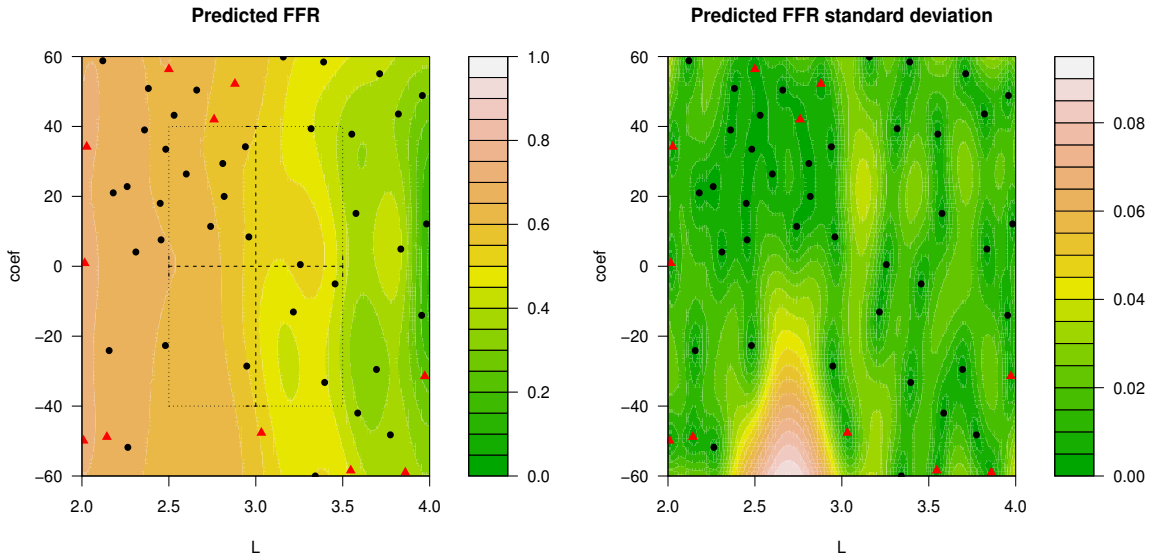

Figure 5.12: Predicted FFR given by GP regression. Designs are marked by points (resp. triangles) for the training (resp. testing) set used later. The dashed lines and dotted box are used later for uncertainty quantification. Left:predictive mean of the FFR values given by the GP. Right: corresponding predictive standard deviation.

given interval, like $L \in [2.5, 3.5]$, $coef \in [-40, 40]$ or in the corresponding box, as illustrated Figure 5.12. As L is much more influential than $coef$, the effect of uncertainty on the former is much more important, the measure FFR can vary by more than 0.1 in this case.

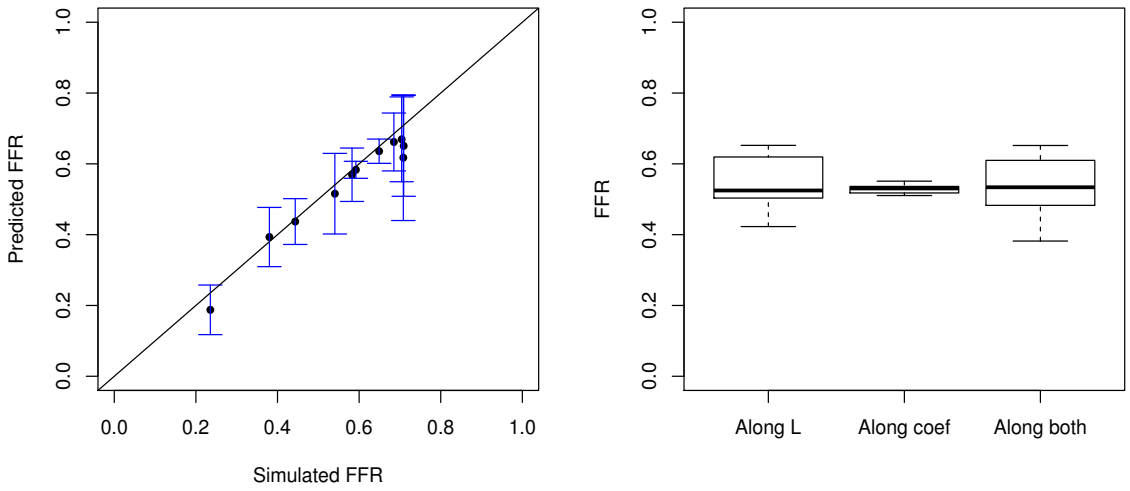

Figure 5.13: Left: predicted FFR versus simulation, the black points depict the mean prediction while the segments denote the 95% prediction intervals. Right: boxplot of FFR values for random position along the segments and box represented in Figure 5.12. The median is represented by the thick line while the box is defined by the lower and upper quartiles.

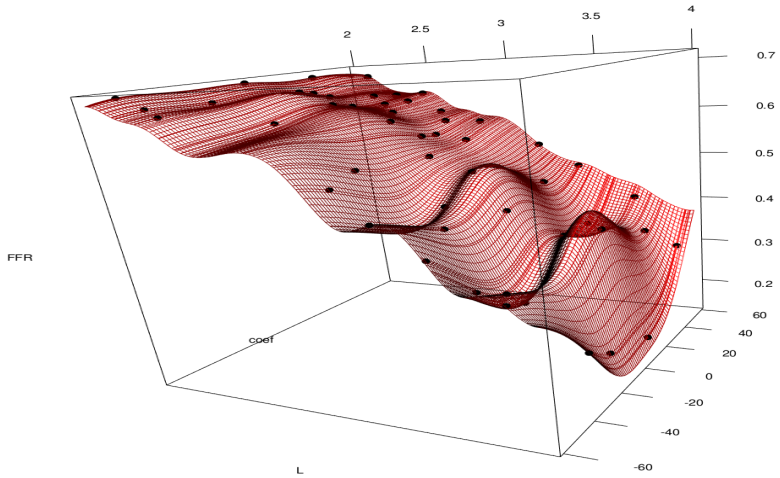

Figure 5.14: 3D view of the statistical predictor.

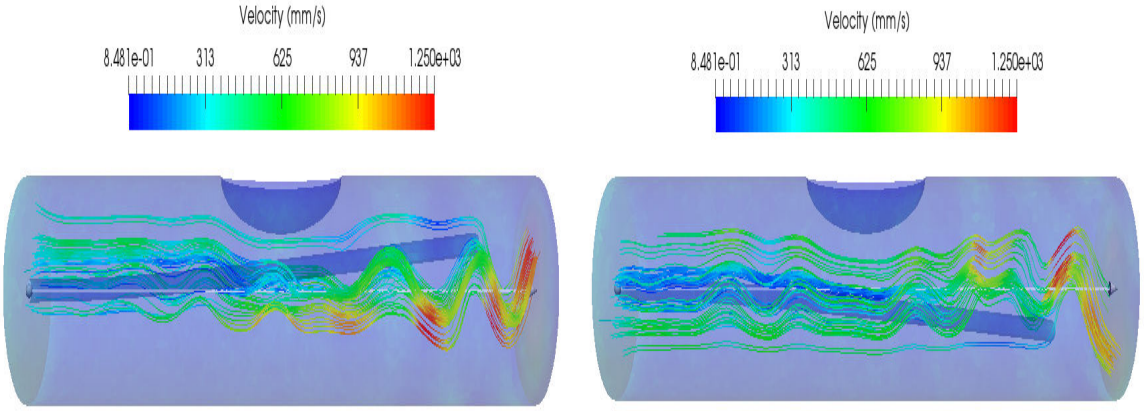

Figure 5.15: Left: velocity streamlines corresponding to sample 49: $L = 3.712$, $coef = 55.08$ and $FFR = 0.4043$. Right: velocity streamlines of sample 54: $L = 3.86$, $coef = -59.0136$ and $FFR = 0.38$.

Results with 4D data

In this section, we consider four parameters to build a map of FFR variations with respect to the two previous parameters considered for the FFR device configuration, and to two additional parameters, introduced to quantify stenosis: the degree of stenosis $a \in [20\%, 60\%]$ and $b \in [0.6, 1.2]$ the radius of the 3D lesion. With analogy to the previous 2D approach, we started by generating 20 initial designs. We observed from the first group of twenty experiment that all FFR values are widely below the cut of 0.8: highest value 0.7196 and lowest value of 0.320. We were surprised by the results, the GP model in this case was insensitive to the two parameters of the lesion. Even if the shape of this last varied in each sample, as shown in table 5.2, all the lesions were classified as significant. After refining the experiment space, and adding 50 new design through a sequential process, the results are still the same: all the samples give an FFR value below the cut off (≤ 0.8), see table 5.2.

Sample i	L_i	$coef_i$	a_i	b_i	FFR_i
1	2.2358	39.042	0.27288	0.99438	0.67103
2	2.484	9.198	0.15726	0.71226	0.659641
3	2.7187	36.234	0.11454	1.1145	0.621718
4	2.8488	14.208	0.18306	0.95298	0.58358
6	2.2957	20.76	0.26508	0.73188	0.673774
7	2.4507	29.814	0.4923	0.96084	0.65136
8	2.3987	37.518	0.5004	0.74046	0.655696
9	2.3245	15.06	0.4743	0.77838	0.672089
10	2.3703	46.818	0.42522	1.0728	0.660043
11	2.6417	17.592	0.07134	0.98052	0.63727

12	2.5074	49.194	0.23346	0.80124	0.64945
13	2.8963	56.448	0.51942	0.75036	0.595705
14	2.6212	54.222	0.53088	1.17888	0.631782
15	2.9094	44.226	0.4599	1.01238	0.580472
16	2.1217	19.122	0.13026	0.81156	0.699746
17	2.1884	45.396	0.37164	0.87606	0.693522
18	2.4394	35.64	0.17652	1.03578	0.660002
19	2.6754	30.294	0.37518	0.78054	0.615614
20	2.02278	0.56616	0.07848	0.648468	0.719645
21	2.216	24.84	0.040464	1.0947	0.690969
22	2.1389	6.678	0.31356	0.88572	0.696781
23	2.867	34.332	0.21132	0.91698	0.585039
24	2.5985	11.382	0.56496	0.91392	0.620903
25	2.5296	31.602	0.5946	1.12632	0.643535
26	2.1611	27.198	0.58398	0.86916	0.681604
27	2.3325	42.222	0.32856	0.64011	0.676706
28	2.8113	5.7906	0.09042	1.18506	0.620811
29	2.7728	23.922	0.13992	0.68772	0.593596
30	2.6694	53.844	0.057996	0.83274	0.631134
31	2.942	12.168	0.40812	1.05636	0.556775
32	2.09074	58.188	0.24732	1.0329	0.707345
33	2.56	58.506	0.54696	0.93882	0.643344
34	2.7264	50.55	0.20298	1.15596	0.615655
35	2.4161	2.2602	0.029154	0.84204	0.689288
36	2.9805	3.4044	0.39804	0.66618	0.565073
37	2.02723	41.454	0.008106	0.70248	0.71150
38	2.05327	8.994	0.4446	0.6058068	0.708303
39	2.972	51.756	0.2934	0.624342	0.565772
40	2.2663	22.398	0.3309	1.14906	0.674914
41	3.65	-39.72	0.4096	0.9198	0.343739
42	3.656	-6.36	0.696	0.8898	0.435539
43	2.764	-38.4	0.6776	0.9126	0.590094
44	3.692	-26.04	0.1176	0.8562	0.328526
45	3.35	-31.68	0.7032	0.7284	0.44868
46	2.964	-57.828	0.2616	0.957	0.582574
47	3.566	-20.28	0.6856	0.9258	0.36852
48	3.804	27	0.2776	1.0908	0.34698
49	3.814	28.92	0.2528	0.7464	0.344258
50	3.844	-37.08	0.5072	0.8904	0.321237
51	3.7	-41.76	0.268	1.0506	0.383927
52	3.812	32.64	0.676	1.0548	0.337689
53	2.1978	-49.26	0.5224	1.0134	0.417448

54	2.45	-50.736	0.468	0.6984	0.655147
55	3.778	34.2	0.2504	1.0866	0.348962
56	2.29	-49.62	0.2832	1.0236	0.666935
57	3.634	24.48	0.28	1.0926	0.336593
58	3.674	36.6	0.6408	0.7314	0.333449
59	3.13	-49.116	0.164	0.7212	0.52262
60	3.634	-35.76	0.3952	0.927	0.331021
61	3.344	28.68	0.1976	0.8946	0.457081
62	3.478	-45.24	0.604	1.0704	0.437839
64	3.758	55.2	0.2552	0.7998	0.415483
65	2.502	-39.6	0.456	1.0788	0.649004
66	2.1636	-28.8	0.6136	1.011	0.682034
67	3.16	-21.24	0.1848	1.0086	0.501702
68	3.314	28.2	0.7456	0.9048	0.440582
69	3.724	21.96	0.06816	0.9768	0.38054
70	2.438	-49.644	0.1616	0.732	0.662238
71	2.442	-29.28	0.336	0.732	0.655274
72	3.732	-15.96	0.3032	1.0686	0.407782

Table 5.2: Four parameters design experiments: parameters and corresponding FFR values

Performing these 4D samples took us many days of simulation. No effect of the lesion's parameters was observed in the model, that is why making prediction based on this GP model is not a good idea. Since we used the same resolution strategy as for the 2D GP: the fluid part, FFR computation strategy, we could not question the approach itself. Since the 2D GP model gave accurate results as shown in the previous result section 5.3.5. One possible reason that we could give is that the 3D design considered for the FFR device is similar to a microcatheter, as shown in figure 5.2 (right). The main criticism addressed to this FFR device (microcatheter) particularly in practice is that it induces a minimal contribution to lesion's severity which may overestimate stenosis (see [54]), and that is what happened in the simulation, since all stenosis were considered to be significant ($FFR \leq 0.8$). The considered ratio of $1/10$ between the portion and the sensor diameters might be not sufficient in our case to generate the 4D GP model.

5.3.6 Comparing FFR issued from virtual sensor to that from a physical sensor

In the previous section, the 3D problem modelling the flow inside a diseased in presence of the FFR sensor, this last was considered as a physical obstacle to the flow, in the contrary to the initial 2D approach presented in the first chapter. In this section, we present a counter-example to demonstrate that taking into account the physical presence of the sensor or not can impact considerably the value of the virtual FFR. The simulation presented in figure

5.16 and 5.17 corresponds to two different 3D mesh, while the flow model and boundary conditions are exactly the same. The methodology of computing the virtual fractional flow reserve is also the same: in fact, the 3D domain in figure 5.16 is created by adding the sensor's configuration to that of the diseased portion. The sensor in this case is considered to be a part of the flow domain and the virtual FFR is computed using the two integrals on Γ_a and Γ_d. In contrary, and like in all previous simulation, in the configuration of figure 5.17, the sensor is considered as a hole inside the diseased coronary portion and blood flows around it. We can observe from the two figure the difference of isolines between the two considered configurations especially in the recirculation zone before/after the lesion. One main difference is that the recirculation is observed before the lesion when the sensor is virtual and after the lesion and sensor where this last is physically existing.

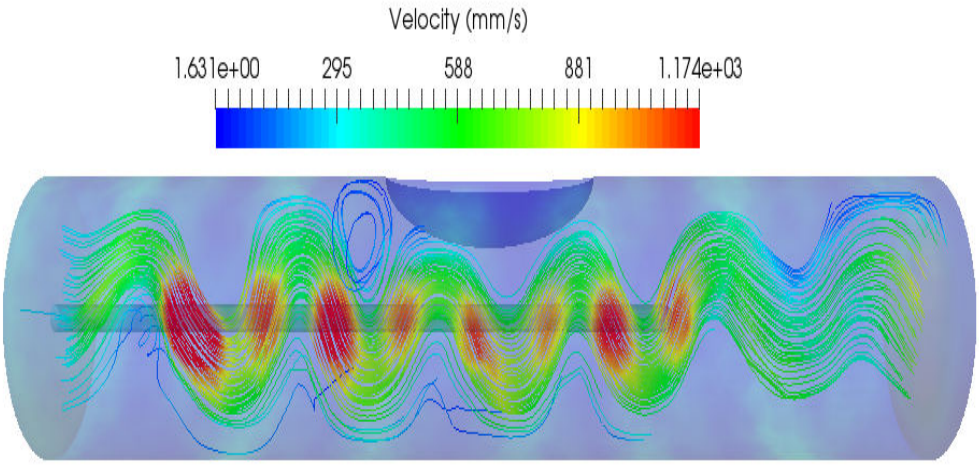

Figure 5.16: Velocity isolines at peak systole. The shadowed tube illustrates the virtual device sensor/guide.

For the fixed lesion of 25% stenosis, and due to the change in the flow between the two proposed configurations, we obtained two different FFR values. In the case where the sensor is considered virtual (merged with the flow domain), we obtain an FFR value of 0.905, which classifies the lesion as hemodynamically non significant. In the opposite case where the sensor is a physical obstacle to the flow, we obtain an FFR value of 0.709 and the lesion is said to be hemodynamically significant. That said, for the same lesion, considering or not the physical presence of the guide+sensor in computing the virtual FFR can change the clinical decision concluded from the non-invasive test suggested in this chapter. The physiological perturbation due to the device (guide+sensor) is inevitable during the invasive FFR procedure. Even if the practitioner makes sure that the recording device is set to zero pressure (all pressures are measured against atmospheric pressure), there is an inevitable drift caused by the change in the vessel caliber in the same coronary tree and by the arbitrary

presence of the guide+sensor (exact location, diameter, torsion during the test...etc).

Many undesirable effects during the FFR procedure can be avoided thanks to simulation, among which lies the presence of the sensor itself. Virtual assessment of the fractional flow reserve gives the possibility to evaluate the hemodynamic signification of a lesion without the need of a physical sensor like demonstrated in this section. However, to validate this type of approaches, we need to validate it by comparing the FFR values issued from simulation to those measured during an invasive test (which is not a simple task, since at least we should use a 3D domain issued from the same coronary tree), and in this case, modelling the device guide+sensor as an obstacle to the flow might be beneficial since the comparison will be in the same basis if the order of magnitude of the different elements are respected.

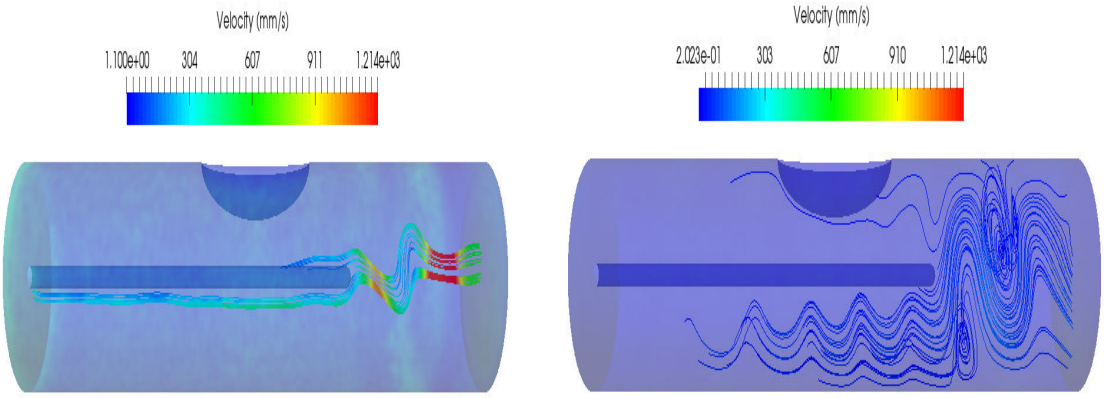

Figure 5.17: Left, velocity isolines at peak systole. Right, velocity isolines at peak diastole. We can see the flow around the physical device.

5.4 Conclusions

During FFR invasive measurement, many undesirable effects can occur during the procedure, leading to a drift in the value of the index. In this chapter, we aimed to illustrate on of these effects through the uncertainty in the pressure distal sensor's position. Using a 2D and 3D modelling of the FFR measurement scenario with a similar computation strategy to the clinical device, we could demonstrate only by simulation that for the same lesion we can have different medical conclusions. In 2D, we led different simulations using two fluid models for blood, Navier Stokes and a non Newtonian model and different outlet boundary conditions: Windkessel vs free outlets. All cases of figures in 2D showed that the FFR values is subject to small changes, that can amplify in function of the degree of stenosis, leading to a decrease in the accuracy of the measure. In 3D, we created different configurations of FFR device (guide+sensor) inside the same diseased arterial portion. Based on Hooke's law, we

could produce a bending effect of the device and we could also vary the length of the distal part of the sensor. With two parameters to modify the configuration of the FFR device, we obtained a set of samples with an FFR value corresponding to each case. The strategy of resolution is based on an automated function written in R language, that calls the different contributors:

1. GEO file with the given value for the sensor's length.
2. GMSH to create the sensor's initial mesh.
3. FreeFem++ algorithm to new sensor's mesh with the given coefficient of bending.
4. FreeFem++ algorithm for fluid resolution inside the global domain (sensor's mesh + diseased portion mesh) and FFR computation.

The set of samples created are used later to create a gaussian model that predicts the FFR value in function of these parameters. This first two parameters GP model indicated a good accuracy. Based on the same methodology, we created a 4D GP model, by varying two additional parameters of the lesion: the degree of stenosis and the lesion's radius. This second set of samples gave the same classification of all lesions: hemodynamically significant, which is intriguing. After refining the space of designs experiments we still obtained the same results. On possible reason of this problem is the relatively elevated diameter of the FFR device considered (1/10 compared to the arterial portion diameter), which is intended to produce an additional contribution to lesion severity. The study presented in this chapter is an evident proof that simulation is an essential key to explore all the eventual sources of error that might occur during FFR test and that impact the accuracy of the measure.

Chapter 6

Conclusions and perspectives

The different studies presented in this thesis aimed to provide a realistic modelling of blood flow inside stenotic coronary arteries. Combining skills and methods of applied mathematics: computational fluid dynamics, segmentation and domain reconstruction from medical images; and from the clinical context: Fractional Flow Reserve (FFR) procedure, atherosclerosis and coronary blood flow.. etc, we tried to investigate -only through simulation- the possibility of stenosis assessment without the need of surgery or expensive devices. The computation of a virtual version of the FFR was a first possibility to do that. Using the different numerical tools and algorithms implemented during this thesis, we could explore the problematic from different sides. We started by a simplified 2D representation of the stenotic arterial portion, the lesion was parameterized by two main quantities: the degree of stenosis and the lesion's radius. Inside the diseased domain, a non Newtonian flow model was defined with common boundary conditions at the inlet and outlet. This flow model was coupled to Koiter model to take into account the elastic property of the arterial wall. Pressure distributions obtained were used to compute the virtual fractional flow reserve. We performed different trials to see how the virtual FFR varies with respect to the two parameters considered for the plaque and to emphasize the need to go beyond the degree of stenosis while evaluating the severity of a coronary lesion. Adding this parameter, like in [17] is one simple way to put the stress on the fact that a 2D projection of the lesion - that is a randomized deposit of grassy cells over the arterial surface - is not enough for the assessment of stenosis, which is usually the case when the clinician resorts only to angiography during diagnosis.

In a second place, we introduced realistic stenotic domains in 2D and 3D and new appropriate boundary conditions based on an electrical analogy: Windkessel boundary conditions. The aim was to test the flow models proposed - that was already introduced in [1] and [2] - combined to the new resistance outlet boundary conditions. In 2D, we compared between Navier Stokes and the generalized flow model and demonstrated that there is a good agreement between them when flow parameters are appropriate. However, free outlet boundary

conditions are not realistic to consider compared to Windkessel boundary conditions, especially while trying to estimate fractional flow reserve. Actually, the value of the fractional flow reserve does not only depend on the lesion itself (even when it is well represented), but also on the peripheral properties of branches (capillary resistance...etc), especially the stenotic one. This effect is taken into account only when the model of outlets boundary condition is based on resistance or impedance models. In our case, the 2 element Windkessel model considered was enough to clarify that. The same type of simulation was performed inside a 3D bifurcation with an extension to 3D of the boundary conditions model.

While advancing on this thesis, we could have some fruitful discussions with clinicians and mathematical researchers. We tried also to keep in touch with most recent papers published in this context. Thanks to that, we could detect several source of errors and question the initial motivation of our project. Years ago, FAME trial showed that FFR guided interventions are associated with better clinical outcomes and lower mortality rate compared to angiography. Since then, investigations are still involving in this view, which yielded to some new alternatives - and probably more sophisticated - to this ratio. iFR (instantaneous wave-free ratio), introduced for the first time in 2012, has been recently demonstrated non inferior to FFR to drive coronary revascularization, see [44]. And might be better in characterizing the potential of stenosis in the presence of discordance between the two indexes, see [45]. The main difference between the two ratios is that iFR represents a diastolic resting index. It allows the assessment of the lesion only during the phase in the cardiac cycle where microvascular resistance is the lowest, allowing increased flow. Moreover, recent clinical trials (FUTURE 2018, see [47]), continue to question FFR utility in guiding treatment strategy. On the other hand, one of the main criticisms addressed to clinical studies involving FFR - including FAME that is the main booster of FFR in clinical use - is that the datas are collected from different laboratories. This small detail implies minor - but non negligible - differences in practice which may cause heterogeneity in acquisition and interpretation, see [46]. Lack of standardization during FFR measurement may lead to some deviations. Standardization includes required verification before and during the test (zero pressure...etc) as well as the use of similar models of devices - especially where we aim to build a data - in particular those in contact with blood flow like catheters and pressure guidewires.

All this considered, many undesirable effects during procedure still can occur, simply because the practitioner is human. During this thesis, we aimed to illustrate on of these elements through the uncertainty in the pressure distal sensor's position. Using a 2D and 3D modelling of the FFR measurement scenario with a similar computation strategy to the clinical device, we could demonstrate only by simulation that for the same lesion we can have different medical conclusions. Based on the 3D model of the FFR device, we could using gaussian processes generate a set of designs by varying the sensor's parameters: length

and coefficient of bending. All cases of figures showed that the FFR value is subject to small changes, that can amplify in function of the degree of stenosis, leading to a decrease in the accuracy of the measure. The goal of this prospective study is to obtain a mathematical model integrating measurable clinical parameters with simulation performances and prediction tools (Gaussian processes for example) which gives a very close estimation to the realistic FFR value. Our aim for futur works is to compare the results from modelling with in vivo measurements recorded during an interventional procedure based on 2D and 3D patient-specific geometries issued from image reconstruction techniques on the one hand. On the other hand, and as demonstrated during this thesis, the choice of an adequate flow model with appropriate boundary conditions - ideally patient-specific - is crucial as to the accuracy of the estimation. The methods and algorithms developed during this thesis is a basis upon which we can build a set of non-invasive and reliable tools to accompany the diagnostic phase. The numerical simulation of blood flow is rivaling and even surpassing experimental fluid mechanics methods to investigate the mechanisms of disease and to design medical devices and therapeutic interventions. In this view the interaction between clinicians and mathematicians is compulsory in terms of assessment and definition of new problematics.

Bibliography

[1] S. Boujena, O. Kafi, N. El Khatib. A 2D Mathematical Model of Blood Flow and its Interactions in an Atherosclerotic Artery. Math. Model. Nat. Phenom. 2014; Vol. 9, pp: 32–54.

[2] S. Boujena, N. El Khatib, O. Kafi. Generalized Navier-Stokes Equations with Non-standard Conditions for Blood Flow in Atherosclerotic Artery. April 9, 2015; Available from http: //www.tandfonline.com/doi/full/10.1080/00036811.2015.1068297

[3] O.Pironneau. Simplified fluide-structure interactions for hemodynamics. Numerical Simulations of Coupled Problems in Engineering 2014; pp : 57-70, . https://doi.org/10.1007/978-3-319-06136-8_3

[4] P. Gostaf, O. Pironneau. Pressure boundary conditions for blood flows. Chinese Annals of Mathematics. September 2015; Series B, Volume 36, Issue 5, pp : 829–842.

[5] V. Chabannes, G. Pena, C. Prud'Homme. High-order fluid-structure interaction in 2D and 3D. Application to blood flow in arteries. Journal of Computational and Applied Mathematics, Elsevier, 2013; vol 246, pp: 1-9.

[6] Irene E. Vignon-Clementel, C. Alberto Figueroa, Kenneth E. Jansen, Charles A. Taylor. Outflow boundary conditions for three-dimensional finite element modelling of blood flow and pressure in arteries. Computer methods in applied mechanics and engineering, 2006; vol 195, pp: 3776–3796.

[7] T. Lassila, A. Manzoni, A. Quarteroni, G. Rozza, A reduced computational and geometrical framework for inverse problems in haemodynamics, International Journal for numerical methods in biomedical engineering, 2013; pp: 1–35.

[8] M. Fernandez, M. Landajuela, M. Vidrascu. Fully decoupled time-marching schemes for incompressible fluid/thin-walled structure interaction. Physics Elsevier,2015; vol 297, pp: 156-181.

[9] Shengxian Tu, Emanuele Barbato, Zsolt Köszegi, Junqing Yang, Zhonghua Sun, Niels R. Holm, Balázs Tar, Yingguang Li, Dan Rusinaru, William Wijns, Johan H.C. Reiber. Fractional Flow Reserve Calculation From 3-Dimensional Quantitative Coronary Angiography and TIMI Frame Count. Elsevier Jacc Cardiovascular interventions, 2014; vol 7.

[10] Morris D, Van de Vosse N, Lawford V, Rodney Hose D, Gunn P (2015) Virtual (Computed) Fractional Flow Reserve : Current Challenges and Limitations. *Elsevier JACC Cardiovasc Interv 8(8): 1009–1017.* https://doi.org/10.1016/j.jcin.2015.04.006

[11] Van Nunen, Richard Lycett, Patricia V. Lawford, Rodney Hose, Julian P. Gunn. Fractional flow reserve versus angiography for guidance of PCI in patients with multivessel coronary artery disease (FAME): 5-year follow-up of a randomised controlled trial. Lancet doi: 10.1016/S0140-6736(15)00057-4, 2015.

[12] C. Bertoglio. Forward and Inverse Problems in Fluid-Structure Interaction. Application to Hemodynamics. Numerical Analysis [math.NA]. Université Pierre et Marie Curie - Paris VI, <tel-00768188>,2012.

[13] Jian Yang, Yongtian Wang, Yue Liu, Songyuan Tang, and Wufan Chen. Novel Approach for 3-D Reconstruction of Coronary Arteries From Two Uncalibrated Angiographic Images. Ieee transactions on image processing; vol 18. NO. 7, July 2009.

[14] Zhi-Yong Li, Simon P.S. Howarth, Tjun Tang, Jonathan H. Gillard. How Critical Is Fibrous Cap Thickness to Carotid Plaque Stability?: A Flow–Plaque Interaction Model. https: //doi.org/10.1161/01.STR.0000217331.61083.3b.Stroke. 2006;37: 1195-1199.

[15] G. Toth, P. Johnson, A. Jeremias, M. Pellicano, P. Vranckx, F. Fearon, E. Barbato, J. Kern, N. Pijls, B. Bruyne. Standardization of Fractional Flow Reserve Measurements. DOI: 10.1016/j.jacc.2016.05.067. August 2016; Vol 68, Issue 7.

[16] T. Cuisset, J. QuiliCi, G. Cayla. Qu'est-ce que la FFR ? Comment l'utiliser ? Réalités Cardiologiques, Janvier/ Février 2013.

[17] Lopez-Palop R, Carrillo P, Agudo P, Frutos A, Cordero A, Lopez-Aranda M, Ramosc D (2013) Correlation Between Intracoronary Ultrasound and Fractional Flow Reserve in Long Coronary Lesions. A Three-dimensional Intracoronary Ultrasound Study. *Rev Esp Cardiol (Engl Ed) 66(9):707-14.* https://doi.org/10.1016/j.rec.2013.04.023

[18] M.Catanho, M.Sinha, V.Vijayan. Model of Aortic Blood Flow using the Windkessel effect. Report BENG 221 - Mathematical Methods in Bioengineering, October 2012.

[19] Available online from
https: stanfordhealthcare.org/content/dam/SHC/conditions/blood-heart-circulation/images/anomalouscoronaryartery-diagram-heart.gif

[20] Taylor CA, Steinman DA (2010) Image-based modelling of blood flow and vessel wall dynamics: Applications, Methods and Future Directions. *Ann Biomed Eng 38(3):1188-203.* https://doi.org/10.1007/s10439-010-9901-0

[21] Liu B, Zheng J, Bach R, Tang D (2015) Influence of model boundary conditions on blood flow patterns in a patient-specific stenotic right coronary artery. *BioMed Eng OnLine 14(Suppl 1): S1.* https://doi.org/10.1186/1475-925X-14-S1-S6

[22] Catanho M, Sinha M, Vijayan V (2012) Model of Aortic Blood Flow using the Windkessel Effect. Report : BENG 221 - Mathematical Methods in Bioengineering. http://isn.ucsd.edu/classes/beng221/problems/2012/BENG221_Project - Catanho Sinha Vijayan.pdf

[23] Vignon-Clementel IE (2006) A coupled multidomain method for computational modelling of blood flow. Phd thesis, Department of mechanical engineering, Stanford university. https://team.inria.fr/reo/files/2012/07/Vie-thesis-asInStanford.pdf

[24] Hecht F (2006) Freefem++ Documentation. https://freefem.org/#documentation

[25] Frank O (1899) Die Grundform des arteriellen pulses: Mathematische Analyse. Erste Abhandlung. *Zeitung für Biologie.*

[26] Toth G, Johnson P, Jeremias A, Pellicano M, Vranckx P, Fearon F, Barbato E, Kern J, Pijls N, Bruyne (2016) Standardization of Fractional Flow Reserve Measurements. *J Am Coll Cardiol 68(7):742-53.* https://doi.org/10.1016/j.jacc.2016.05.067

[27] Javadzadegan, Yong AS, Chang M, Ng AC, Yiannikas J, Ng MK, Behnia M, Kritharides L (2013) Flow recirculation zone length and shear rate are differentially affected by stenosis severity in human coronary arteries. *Am J Physiol Heart Circ Physiol 304(4):H559-66.* https://doi.org/10.1152/ajpheart.00428.2012

[28] Shepharda MS, Flaherty J, Jansena K, Li X, Luo X, Chevaugeon N, Remacle JF, Beall M, O'Barac RM (2005) Adaptive mesh generation for curved domains. Applied Numerical Mathematics *52:251–27.* https://doi.org/10.1016/j.apnum.2004.08.040

[29] K.Chahour, R. Aboulaich, A. Habbal, C. Abdelkhirane and N. Zemzemi. Numerical simulation of the fractional flow reserve (FFR) Mathematical Modelling

of Physiological Flows, *Math. Model. Nat. Phenom.* **Vol. 13**, No. 6 (2018). https://doi.org/10.1051/mmnp/2018069

[30] Guerra T, Catarino C, Mestre T, Santos S, Tiago J, Sequeira A (2018) A data assimilation approach for non-Newtonian blood flow simulations in 3D geometries. *Applied Mathematics and Computation 321:176–194.* https://doi.org/10.1016/j.amc.2017.10.029

[31] Gimel'farb G (2013) Image processing: Image filtering and segmentation. OMPSCI 373 Computer Graphics and Image Processing. https://www.cs.auckland.ac.nz/courses/compsci373s1c/PatricesLectures/2013/CS373-IP-03.pdf

[32] Boileau E, Pant S, Roobottom C, Sazonov I, Deng J, Xie X, Nithiarasu P(2017) Estimating the accuracy of a reduced-order model for the calculation of fractional flow reserve (FFR). *Int J Numer Method Biomed Eng 34:1.* https://doi.org/10.1002/cnm.2908

[33] Kim HJ, Vignon-Clementel IE, Coogan JS, Figueroa CA, Jansen KE, Taylor CA(2010) Patient-specific modeling of blood flow and pressure in human coronary arteries. Ann Biomed Eng. 2010 Oct;38(10):3195-209. doi: 10.1007/s10439-010-0083-6. Epub 2010 Jun 18. Review. PubMed PMID: 20559732.

[34] Fearon WF, Chambers JW, Seto AH, and al. ACIST-FFR Study (Assessment of Catheter-Based Interrogation and Standard Techniques for Fractional Flow Reserve Measurement). Circ Cardiovasc Interv. 2017;10(12):e005905. doi:10.1161/CIRCINTERVENTIONS.117.005905

[35] Morton Kern, MD. Comparing FFR Tools: New Wires and a Pressure Microcatheter, CLINICAL EDITOR'S CORNER: KERN, Volume 24 - Issue 5 - May 2016 available online: https://www.cathlabdigest.com/article/Comparing-FFR-Tools-New-Wires-Pressure-Microcatheter

[36] Christopher M. Cook, Yousif Ahmad, Matthew J. Shun-Shin, Sukhjinder Nijjer, Ricardo Petraco, Rasha Al-Lamee, Jamil Mayet, Darrel P. Francis, Sayan Sen, and Justin E. Davies. Quantification of the Effect of Pressure Wire Drift on the Diagnostic Performance of Fractional Flow Reserve, Instantaneous Wave-Free Ratio, and Whole-Cycle Pd/Pa. Circulation: Cardiovascular Interventions. 2016;9:e002988. (April 2016). https://doi.org/10.1161/CIRCINTERVENTIONS.115.002988

[37] Available online from: http://tpe2016nddcoeur.e-monsite.com/pages/i-la-miniaturisation-au-service-du-cardiologue/le-stent-bon/

[38] Pim A.L. Tonino and al. Fractional Flow Reserve versus Angiography for Guiding Percutaneous Coronary Intervention. N Engl J Med 2009; 360:213-224. January 15, 2009 DOI: 10.1056/NEJMoa0807611

[39] Monos E. Biomechanics of the blood vessels Medicina Kiadó, 1986. Budapest.

[40] https://math.unice.fr/wiki/utilisation-du-cluster-vsmp-math5unicefr

[41] http://www.scalemp.com

[42] Tetgen manual, available online: http://wias-berlin.de/software/tetgen/1.5/doc/manual/manual.pdf

[43] Rasmussen, C. E. and Williams, C. (2006). *Gaussian Processes for Machine Learning*. MIT Press.

[44] Verardi R, Fioravanti F, Barbero U, Conrotto F, Omedè P, Montefusco A, Moretti C, D'Amico M, Rinaldi M, Escaned J, D'Ascenzo F. Network meta-analysis comparing iFR versus FFR versus coronary angiography to drive coronary revascularization. J Interv Cardiol. 2018 Dec;31(6):725-730. doi: 10.1111/joic.12551. Epub 2018 Aug 23.

[45] Jeremias A. Instant Wave-Free Ratio or Fractional Flow Reserve for Hemodynamic Coronary Lesion Assessment? Yes, Just Do It! Circ Cardiovasc Interv. 2018 Jan;11(1):e006284. doi: 10.1161/CIRCINTERVENTIONS.117.006284.

[46] Gabor G. Toth, Nils P. Johnson, Allen Jeremias, Mariano Pellicano, Pascal Vranckx, William F. Fearon, Emanuele Barbato, Morton J. Kern, Nico H.J. Pijls, Bernard De Bruyne, Standardization of Fractional Flow Reserve Measurements, Journal of the American College of Cardiology,Volume 68, Issue 7,2016,Pages 742-753,ISSN 0735-1097. https://doi.org/10.1016/j.jacc.2016.05.067.

[47] FUTURE trial. Available online: http://www.crtonline.org/Assets/64d1e459-07e3-414c-8d58-a2c54d3afec2/636708919813530000/future-pdf

[48] Sabina Salles and al. 2011 J. Phys.: Conf. Ser. 332 012048 doi:10.1088/1742-6596/332/1/012048

[49] Sara Moccia, Elena De Momi, Sara El Hadji, Leonardo S. Mattos, Blood vessel segmentation algorithms — Review of methods, datasets and evaluation metrics. Computer Methods and Programs in Biomedicine, Volume 158, 2018, Pages 71-91, ISSN 0169-2607. https://doi.org/10.1016/j.cmpb.2018.02.001.

[50] N. El Khatib, S. Génieys, V. Volpert Atherosclerosis Initiation Modeled as an Inflammatory Process. Math. Model. Nat. Phenom. 2 (2) 126-141 (2007) DOI: 10.1051/mmnp:2008022

[51] Bessonov, N., Sequeira, A., Simakov, S., Vassilevskii, Y., Volpert, V. (2015). Methods of Blood Flow Modelling. Mathematical Modelling of Natural Phenomena, 11(1), 1–25. doi:10.1051/mmnp/201611101

[52] A. Tosenberger, F. Ataullakhanov, N. Bessonov, M. Panteleev, A. Tokarev, V. Volpert, Modelling of thrombus growth in flow with a DPD-PDE method, Journal of Theoretical Biology, Volume 337, 2013, Pages 30-41, ISSN 0022-5193, https://doi.org/10.1016/j.jtbi.2013.07.023.

[53] Miloš Zlámal(2006) Curved Elements in the Finite Element Method *SIAM J. Numer. Anal 10(1), 229–240* https://doi.org/10.1137/0710022

[54] Pouillot C, Fournier S, Glasenapp J, Rambaud G, Bougrini K, Vi Fane R, Geyer C, Adjedj J. (2018) Pressure wire versus microcatheter for FFR measurement: a head-to-head comparison. EuroIntervention. 2018 Feb 2;13(15):e1850-e1856. doi: 10.4244/EIJ-D-17-00238. PubMed PMID: 28804057.